Title
InSAR Inversion Using Point Sources: A Case Study of the Ridgecrest Earthquake Sequence

Author
Saylor, Cameron

Publication Date
2022

Peer reviewed|Thesis/dissertation

InSAR Inversion Using Point Sources: A Case Study of the Ridgecrest Earthquake Sequence

By

Cameron Cole Saylor

Dissertation

Submitted in partial satisfaction of the requirements for the degree of

Doctor of Philosophy

in

Physics

in the

Office of Graduate Studies

of the

University of California

Davis

Approved:

John Rundle, Chair

Robin Erbacher

Eric Prebys

Committee in Charge

2022

To all of my family and friends who have supported me.

Contents

List of Figures

List of Tables

Abstract

InSAR Inversion Using Point Sources:
A Case Study of the Ridgecrest Earthquake Sequence

Interferometric synthetic-aperture radar (InSAR) interferograms provide maps of the surface deformation of the earth. Hidden in these deformation maps is valuable information about the fault systems hidden beneath the surface of the earth. InSAR interferograms are commonly used in inverse problems to determine the characteristics of earthquake sources from the deformation that they caused, which tell us about the faults upon which the earthquake occurred. These inversions typically use models composed of rectangular fault planes, but many studies suggest that faults are much more complicated. In this thesis, we present a new method for the inversion of InSAR interferograms using a model composed of a distribution of seismic point sources. We argue that point sources provide a much greater degree of flexibility to the model at less computational cost compared to rectangular sources.

We start our analysis with an interferogram containing the ground deformation caused by the 2015 M_w 7.8 Gorkha earthquake [9]. After defining a point source model, we explore several different methods of performing the inversion for the source parameters: a genetic algorithm, a multiple linear regression and a nonlinear least-squares solver. During our analysis, we describe the positive and negative aspects of each inversion method, as well as possible interpretations of the results. We conclude our analysis with a case study of the 2019 M_w 7.1 Ridgecrest earthquake mainshock, which serves to expand the preceding analysis to fully explore the capabilities of each method using ground deformation in multiple directions. To extend our analysis of the point source distributions from our inversions, we calculate their fractal dimensions and compare them to the dimensions of the aftershock distribution and fault traces.

Acknowledgments

Thanks to my committee and my family for providing useful guidance throughout the research presented in this thesis.

Chapter 1

Introduction

The characterization of earthquake faults remains a problem that is difficult to solve. In some cases the earthquakes help us out by creating extensive networks of surface cracks that we can measure either in the field or by using remote sensing techniques. In other cases, however, they make our efforts more difficult. So-called blind thrust earthquakes do not produce surface cracks, precluding direct mapping of the faults upon which they occur. Yet, the lack of surface traces does not make remote sensing useless—maps of the ground deformation caused by blind thrust earthquakes can still be produced using methods such as interferometric synthetic aperture radar (InSAR). Ground deformation maps are frequently used for inversion problems that allow us to infer the parameters of the earthquakes that caused the deformation [10, 11, 12]. However, our current models frequently use simple rectangular fault models to represent even the most complex earthquakes.

Significant errors can occur in fault geometry and slip dislocation models as a result of fault surfaces not being well represented by simple planar or rectangular fault models. For this reason, it is necessary to utilize all tools available to improve estimates of fault geometry and location. As mentioned above, one such tool is InSAR, which provides maps of surface deformation that contain valuable information about the complexity of the fault system giving rise to the deformation [13]. InSAR is a radar technique that uses a synthetic aperture radar (SAR) mounted on a satellite to image the same area at two different times, and uses those images to determine the differences in phase of the

waves that return to the SAR. Since the wavelength of the electromagnetic waves emitted by the SAR is known, the phase difference between the images can be used to calculate their difference in line-of-sight distance to the satellite. The result is a map of the line-of-sight ground deformation of the imaged area that occurred between the times that the original SAR images were taken [14]. Despite being susceptible to different sources of error—such as orbital error [15] and atmospheric uncertainty [16, 17]—InSAR is able to measure ground deformation to sub-millimeter accuracy if such effects are appropriately accounted for [18].

Previous work has been done which aimed to invert the ground deformation contained in InSAR interferograms to find the geometry of faults that could cause the observed ground deformation. Such methods rely on having a model that depends on various parameters that can recreate the desired dataset. In seismology, a commonly used model is Okada's analytical solutions for surface deformation due to faults in an elastic half space, which can model ground deformation due to either point or finite rectangular seismic sources [5].

The inversion detailed in Bagnardi and Hooper (2018), for example, utilizes an Okada rectangular fault model described by 9 parameters: length, width, depth, strike angle, dip angle, X and Y-coordinates, uniform slip in the strike direction, and uniform slip in the dip direction [19]. Their approach uses a Bayesian inversion to determine a posterior probability density function (PDF), which describes how well a set of parameters can explain a given dataset based on their uncertainties and taking into account prior information in the form of a joint prior PDF. A Monte-Carlo Markov Chain utilizing the Metropolis-Hastings algorithm is then used to efficiently search the parameter space by taking steps in the prior PDF to get new sets of parameter values and comparing the likelihood of the new model to the previous step [20]. After an appropriate number of iterations, the sampling done by the algorithm approximates the desired posterior PDFs of each of the parameters, which can be used to estimate their most likely values. Jo et al. (2017) performed a different type of inversion for the $M_W = 6.0$ 2014 South Napa earthquake for a similar set of parameters for a rectangular fault model [21]. They used two separate

inversions in their analysis, the first being a Monte Carlo simulation of 10000 iterations to find the fault parameters. The second was a least squares inversion performed to find the slip distribution over the rectangular fault plane.

Aside from Monte Carlo methods, there are other analysis techniques that have been used to invert InSAR interferograms. Feng et al. (2017) utilized a method of inversion called multipeak particle swarm optimization (M-PSO) to study the 2011 $M_W = 6.8$ Burma earthquake [22]. A PSO works by first defining a population (or swarm) of candidate solutions to a problem and then moving them throughout the parameter space to find the optimal solution. The particles move according to a "velocity" that is based on each particle's own best known position in the parameter space as well as the best known position of the other particles [23]. Wen et al. (2016) and Li et al. (2020) also used a M-PSO inversion in their analyses of the 2015 $M_W = 6.5$ Pishan earthquake and the 2013 $M_W = 6.6$ Lushan earthquake, respectively, while additionally adding a second inversion for the slip distribution on the fault plane [24, 25].

There have also been advances in specific aspects of the inversion, such as the slip distribution. Liu and Xu (2019) developed another method for the joint inversion of coseismic and postseismic fault slip from InSAR data called LogSIM, which uses a logarithmic model solved by a nonlinear least squares curve fitting function [26]. Zhang et al. (2008) solved the slip distribution inverse problem with a model using triangular dislocation elements to more accurately model the 3D fault surface [27]. They solved the resulting inverse problem using a weighted damped least squares approach. G. Jiang et al. (2013) also performed an inversion utilizing a model made up of triangular dislocation elements, finding a solution using bounded variable least squares [28]. Fukahata and Wright (2008) aimed to improve the inversion of the slip distribution by treating the dip angle as a hyperparameter and estimating it using the Bayesian information criterion [29]. This is followed by determining the slip distribution using maximum-likelihood methods. Their work is continued in another paper by Fukahata and Hashimoto (2016) who apply the same method to the 2016 Kumamoto earthquake [30]. Frietsch et al. (2019) extended the problem slightly, adding two new parameters for time-shift to the centroid time and

the compensated-linear-vector-dipole (CLVD) component while also allowing for the parameters of multiple fault segments to be found at one time [31]. This makes it possible to model a single event as multiple fault segments or model multiple separate events at the same time.

Finally, it should be noted that InSAR is not limited in usefulness to earthquake mechanism inversion, as shown by Peng et al. (2018) who used InSAR-derived deformation data to invert the mechanism of subsidence of Line 3 of the Xi'an metro near Yuhuazhai [32]. They found from their inversion of a flat-lying sill model with distributed contractions—with a depth based on the average depth of local pumping wells—that the rapid subsidence could be explained by excessive groundwater extraction in the area.

Also note that the inversion of the focal mechanism of earthquakes can be done from a variety of sources other than InSAR data. A common method of inversion uses P-wave first motion polarities, such as the analyses performed by Langet et al. (2020) and Hicks et al. (2000) [33, 34]. If the number of seismic stations is too low to use first motion polarities, a full waveform analysis can be performed to provide constraints on the focal mechanism. Examples of full waveform analysis are reported in Hicks et al. (2000) as well as Villegas A. et al. (2016) [34, 35]. Efforts made to improve these analyses include work by Sokos and Zahradnik (2008) on the ISOLA software package, which can perform multi-source inversions in addition to the typical single source inversions [36].

Though many previous inversions of InSAR data utilize a number of rectangular fault planes, it has been shown that fault surfaces are much more complex. Researchers have taken steps to fight this problem. Sahimi et al. (1993) performed an analysis of the fracture patterns in heterogeneous rocks and found that "at large length scales, they are percolation fractals with a fractal dimension D≈1.9 and 2.5, in 2D and 3D, respectively" [37]. This implies that fault surfaces cannot be completely represented by simple planar surfaces. Candela et al. (2012) studied fault surface roughness over nine decades of length scales from 50 μm to 50 km and found that they could be characterized by an anisotropic self-affine description [38]. Bruhat et al. (2019) investigated the effect of surface roughness on surface displacement, finding that "slip distributions become increasingly more

self-affine, that is, containing more short wavelength fluctuations as compared to the self-similar fault profiles, as roughness increases," suggesting that fault roughness has a considerable effect on the behavior of faults and, therefore, our models must be improved to take such effects into account [39].

The complexity of earthquake modeling is not limited to the fault surfaces, as shown by the 2016 Kaikoura earthquake in New Zealand. This magnitude 7.8 earthquake was one of the largest recorded in New Zealand, and was found to have caused the rupture of at least 12 different faults, with some separated by up to 15 km [40]. Hamling et al. (2017) also state that "The earthquake should motivate rethinking of certain seismic hazard models, which do not presently allow for this unusual complex rupture pattern." Another complex earthquake sequence was that of the magnitude 7.3 Landers earthquake in 1992, around which occurred the magnitude 6.5 Big Bear earthquake and the magnitude 5.7 Little Skull Mountain earthquake, which were later determined to be separate events rather than mainshocks and aftershocks [41].

Due to the complex nature of faults, it is important to improve our models so that they can appropriately represent a wider range of behavior. In this thesis, we introduce a new approach that utilizes a model composed of a collection of seismic point sources. We choose point sources because their superposition can represent any possible physical surface as long as enough sources are included, providing much more freedom than simple rectangular models. The first iteration of our inversion method uses a genetic algorithm to simultaneously find the parameters of the entire collection of point sources. It is followed by a version that uses multiple linear regression to rapidly solve for the model parameters. The final iteration of our method uses a nonlinear solver called LMFit to perform the inversions which improves upon the weaknesses of the preceding models. Finally, we include additional analysis that explores the fractal properties of the point source distributions obtained from the inversions.

Chapter 2

The Characterization of Earthquake Sources

2.1 Earthquake Faulting

A fault is a fracture in a volume of rock. Faults are usually represented by a fault plane that passes through the fracture. The blocks of rock on either side of the fault can slide past each other due to this fracture. Depending on the direction of slip, the fault is categorized as either strike-slip or dip-slip. For a dip-slip fault, each of these blocks are commonly referred to as the hanging wall and footwall. The hanging wall is the block that lies physically above the fault plane, while the footwall is the block that lies below the fault plane. The hanging wall and footwall are labeled in the top left part of Figure 2.1. There are several ways in which the slip on a fault can occur—four basic fault types are shown in Figure 2.1.

The top half of Figure 2.1 shows two different types of dip-slip faults. The top left shows an example of a normal fault. Normal faults occur when the hanging wall of the fault moves downward relative to the footwall. When the movement direction of both blocks is reversed, it is a reverse fault. An example of a reverse fault is shown in the top right part of Figure 2.1. In this case, the hanging wall moves upward relative to the footwall.

The bottom half of Figure 2.1 shows two different types of strike-slip faults. The left side is a left-lateral strike-slip fault while the right is a right-lateral strike-slip fault.

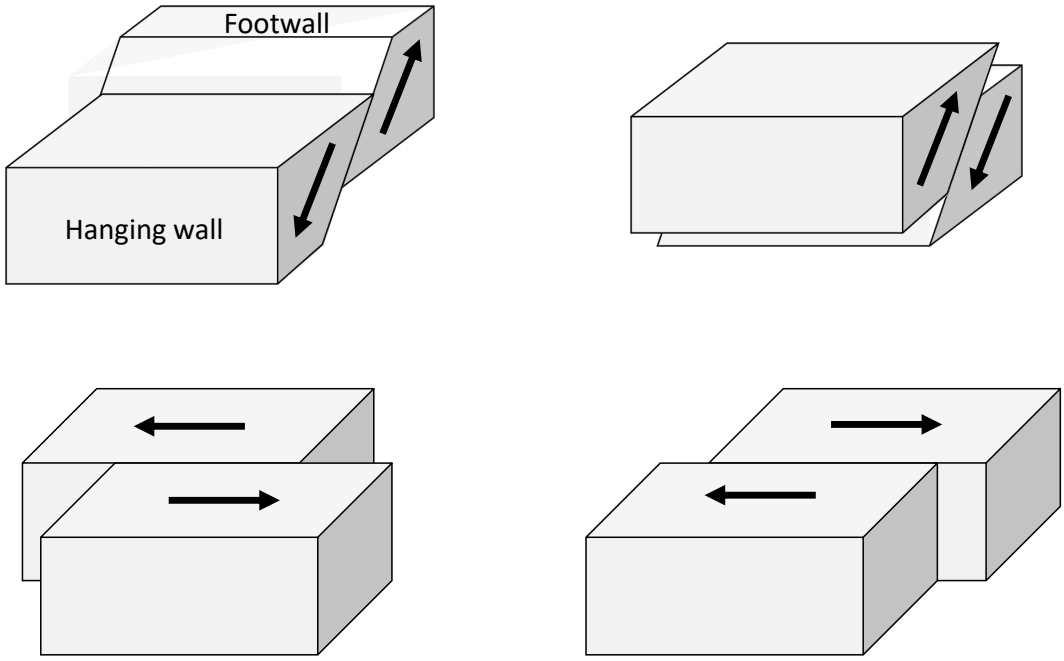

Figure 2.1. The different types of earthquake faults. The top row shows two types of dip-slip faults while the bottom row shows two types of strike-slip faults. Top left: normal fault. Top right: reverse fault. Bottom left: left-lateral strike-slip fault. Bottom right: right-lateral strike-slip fault.

Strike-slip faults do not have a hanging wall or footwall because the fault plane is vertical. Instead, the type of strike-slip fault is determined by imagining standing on one block while facing the fault and seeing which direction the other block moves. For example, when standing on one side of a left-lateral strike-slip fault, the block on the opposite side will be moving to the left.

When it comes to actual faults, it is rare to find a fault that is solely strike-slip or solely dip-slip. Most faults are oblique-slip, which means they have both strike-slip and dip-slip components.

2.2 Earthquake Detection and Measurement

The term earthquake refers to any event that generates seismic waves which shake the surface of the earth. Typically, this is due to a sudden release of energy in the earth's lithosphere when the rocks on either side of a fault slide past each other. The sudden

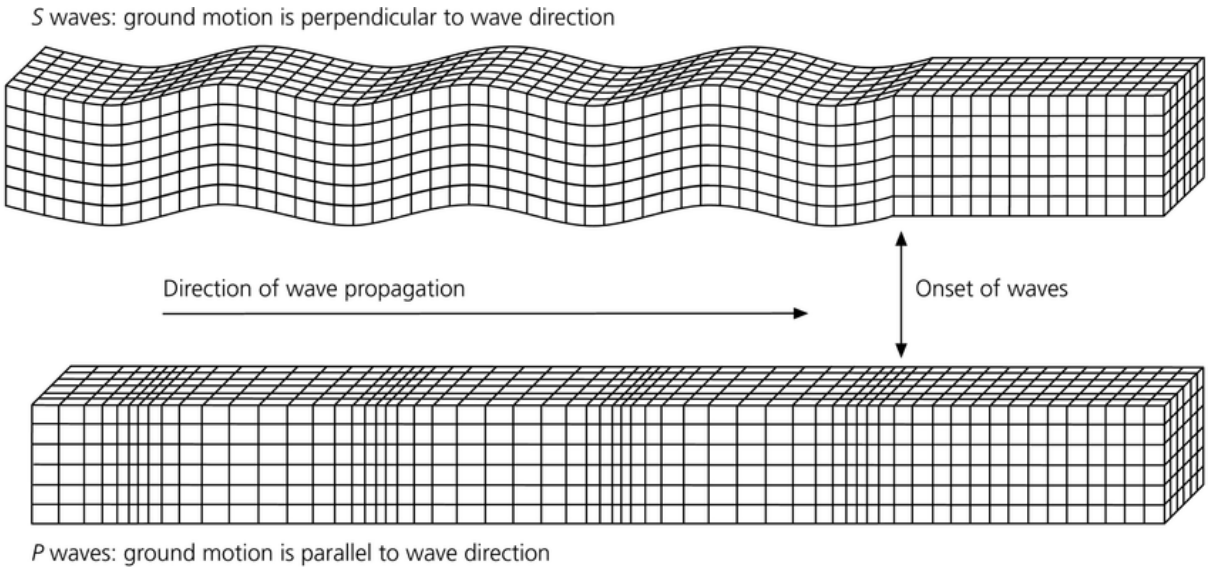

Figure 2.2. The ground motions caused by S and P waves propagating to the right through an elastic medium [1]. S waves cause transverse ground motion, while P waves cause longitudinal ground motion.

release of energy manifests itself in the form of two types of seismic waves: P waves and S waves. P waves (pressure or primary waves) are longitudinal waves while S-waves (shear or secondary waves) are transverse waves. Longitudinal waves oscillate the medium in the direction of their propagation and transverse waves oscillate the medium perpendicular to their direction of propagation. Figure 2.2 shows examples of both P and S waves traveling through a medium. Primary waves are so-named because they travel the fastest, and are therefore the first to arrive at a seismometer. They are shortly followed by the S waves, which themselves are followed by surface waves.

Surface waves are the result of interference between P and S waves on the earth's surface, and they produce the largest ground motion of all of the waves. There are two types of surface waves: Love waves and Rayleigh waves, which are shown in Figure 2.3. Love waves are the result of the interference of multiple S waves and cause horizontal transverse ground motion. Rayleigh waves arise from interference of both P and S waves on the surface and cause both transverse and longitudinal ground motion. Figure 2.4 is a representative example of a seismogram that shows the relative magnitudes and arrival times of each wave type.

To record a seismogram we use a seismometer (also frequently called a seismograph,

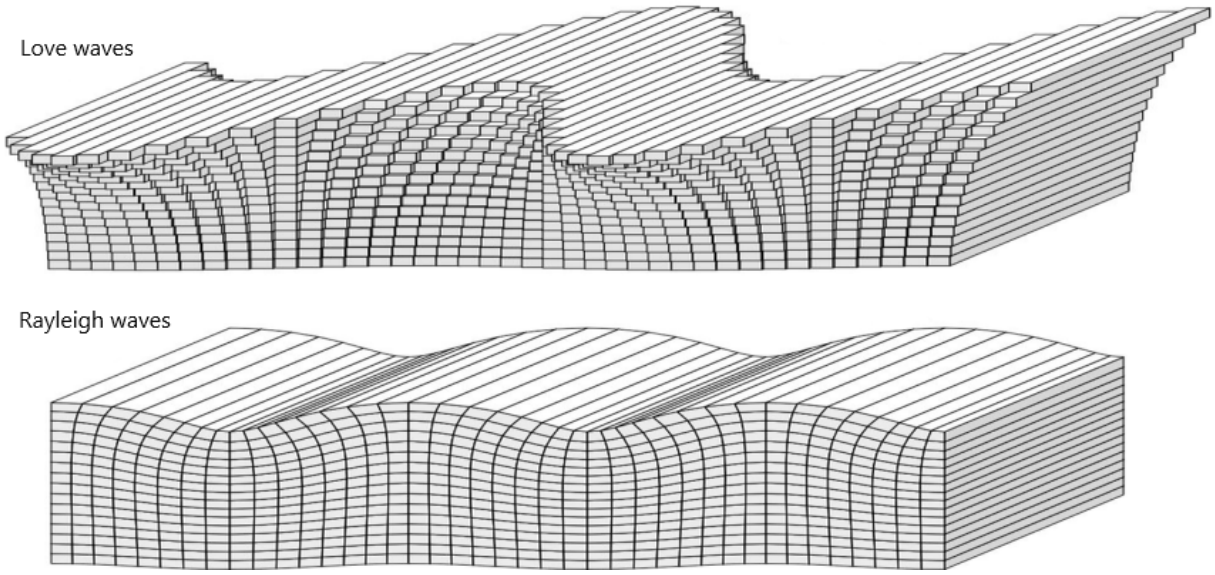

Figure 2.3. The ground motions caused by Love and Rayleigh waves propagating to the right through a medium [1]. Love waves are the result of the interference of multiple S waves and cause transverse ground motion. Rayleigh waves result from the interference of both P and S waves and cause a combination of transverse and longitudinal ground motion.

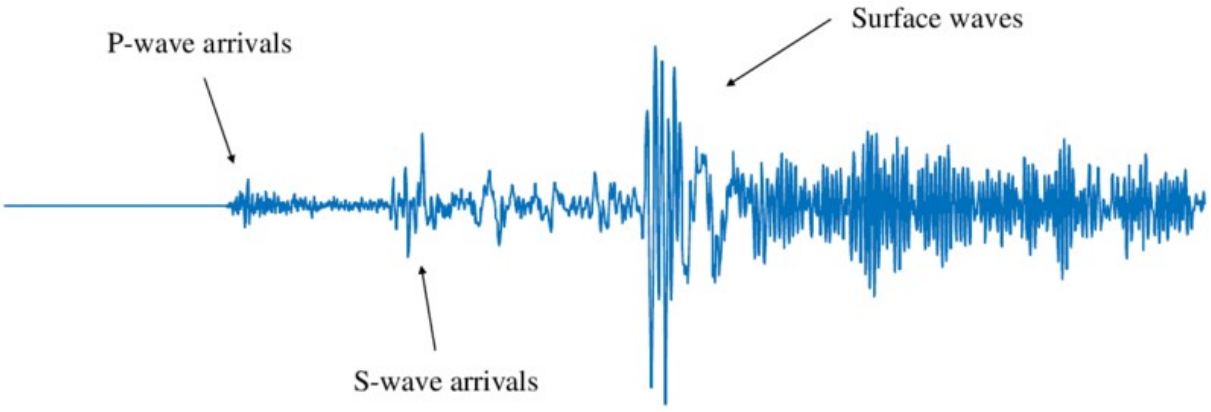

Figure 2.4. An example seismogram. The arrivals of each wave type are indicated by arrows. Adapted from [2]. P waves have the highest speed and arrive first, followed by the S waves and then the surface waves. The surface waves have the highest amplitude because they cause the most significant ground motion.

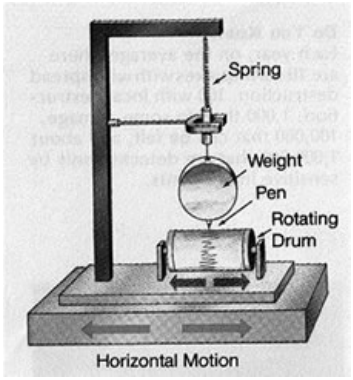

Figure 2.5. An early seismometer. This one would only measure ground motion in the direction indicated by the arrows. Getting full 3-dimensional seismograms would require two additional seismometers constructed to measure ground motion in the other two directions [3].

which is the combination of a seismometer, a timer, and data recorder). A basic seismometer consists of a mass on a spring that is attached to a fixed base. When seismic waves pass by the seismometer, the base follows the ground motion while the mass remains motionless due to inertia. The seismometer then records the relative motion between the mass and base. Historically this was done by attaching a pen to the mass which hangs onto a circular drum attached to the base and records the shaking as the base moves relative to the pen. Figure 2.5 shows the construction of a single-direction seismometer. Modern seismometers record their measurements electronically but remain based on the same basic principles.

2.3 Source Parameters

Figure 2.6 contains a schematic of a simple rectangular fault and its associated parameters. The hanging wall block is removed, leaving only the footwall block. The horizontal (x-y) plane represents the earth's surface and the angled plane that contains the vector u represents the fault plane. Each of the labeled parameters are required to fully describe the behavior of the fault when it slips. First is the position of the fault in the earth's crust. A common convention is to report the latitude, longitude, and depth d of the upper left corner of the footwall, which is shown centered at the origin in Figure 2.6. The length L and width W determine the extent of the fault plane and are also measured from the

Fault type	Rake angle
Normal	-90°
Reverse	90°
Left-lateral strike-slip	0°
Right-lateral strike-slip	180°

Table 2.1. The rake angles for the four different types of fault slip in Figure 2.1. The definition of the rake angle λ is shown in Figure 2.6.

Parameter	Limits
Strike angle (ϕ)	$0° < \phi < 360°$
Dip angle (δ)	$0° < \delta < 90°$
Rake angle (λ)	$-180° < \lambda < 180°$

Table 2.2. Summary of the angles required to define a fault's orientation and their associated limits.

upper left corner of the fault plane.

To determine the orientation of the fault plane, we require two angles: the strike ϕ and dip δ. The strike angle is defined as the angle between north and the strike of the fault. The fault strike is the line tracing the intersection of the fault plane and the horizontal plane. In Figure 2.6 the fault strike is parallel to the x axis. The dip angle of a fault is defined as the angle between the fault plane and the horizontal plane. A dip angle of 0° would yield a horizontal fault plane and a dip angle of 90° would be a vertical fault plane.

The final parameter is the slip vector u which determines how much the fault slips and in what direction the slip occurs. The direction is defined by the rake angle λ, which is the angle between the strike of the fault and the slip vector. The rake angle defines the direction the hanging wall block moves during fault rupture and therefore what type of fault it is. The slip vector can be split into strike-slip (u_s) and dip-slip (u_d) components as indicated in Figure 2.6—this slip vector in particular shows oblique-slip faulting as a combination of left-lateral strike-slip and reverse dip-slip faulting. The rake angles for each fault type in Figure 2.1 can be found in Table 2.1. A summary of the parameters required to fully describe an earthquake source are shown in Table 2.2.

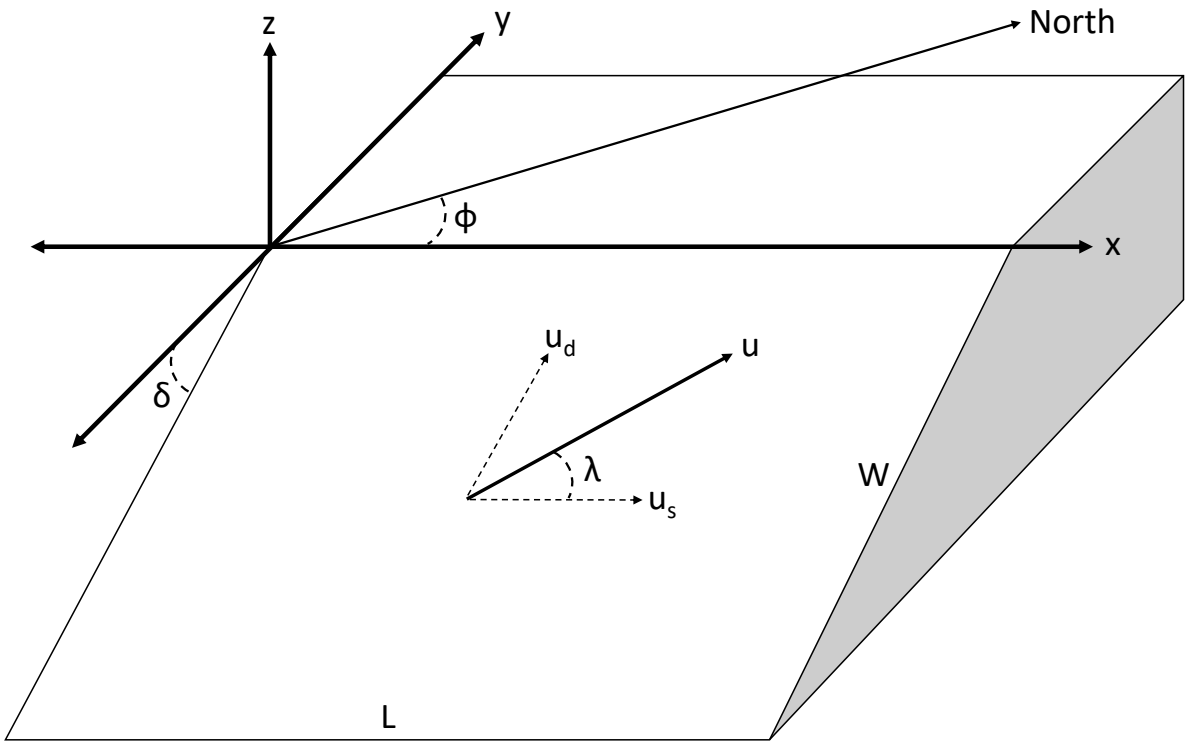

Figure 2.6. The geometric definitions of the various fault parameters. The strike angle ϕ is the angle between the fault surface trace and north. The dip angle δ is the angle between the fault plane and the horizontal plane. Rake angle λ is the angle between the fault slip vector u and the fault strike and determines what type of faulting occurs when the fault slips. L and W indicate the length and width of the fault plane, respectively. The fault slip vector u determines how much the fault slips, and can be broken into strike-slip (u_s) and dip-slip (u_d) components.

A commonly used descriptor of earthquake size is the moment magnitude scale (M_w) developed by Hanks and Kanamori (1979), which they report as $M_w = (logM_0 - 9.05)/1.5$ [42]. It is based on seismic moment (M_0) which is defined by the equation $M_0 = \mu AD$, where μ is the shear modulus of the rock, A is the area of the fault that ruptures during the earthquake and D is the average displacement between the two sides of the fault. The seismic moment represents the torque of each force couple in the double couple model of seismic sources which is described in Section 2.4.

2.4 Double Couple and Shear Dislocation Models

There are two models that are commonly used to model the waves radiated from earthquake sources. First is the double couple point force model which represents an earthquake

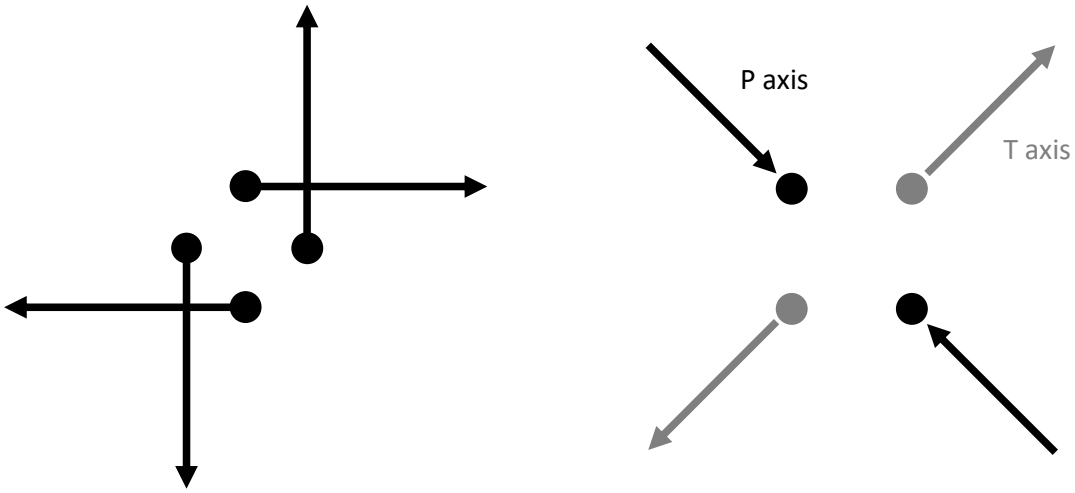

Figure 2.7. Two double couple source models that produce the same seismic wave radiation pattern. The left model consists of moments defined by force couples and the right consists of linear vector dipoles. The P axis is the direction of maximum compressive stress, while the T axis is the direction of minimum compressive stress.

using forces that act on a single point in an elastic medium. The simplest force model that reproduces the elastic wave pattern generated by an earthquake is a double couple, which represents a pure shear dislocation. A double couple consists of two orthogonal pairs of forces, each of which contains anti-parallel forces separated by a moment arm. An example double couple model is shown in the left half of Figure 2.7. The right half of Figure 2.7 shows another double couple that is mechanically equivalent to the one on the left. The locations of the two planes of maximum shear (also called nodal planes) can be inferred from the model on the left. One plane results from each couple of forces and lies both between and parallel to the forces in that couple. The model on the right more clearly shows the P and T axes which are the directions of maximum compression and tension, respectively. Both of these double couple models produce the same seismic wave radiation patterns and simply display different information about the seismic source they represent.

The second model that produces seismic wave radiation similar to actual earthquakes is the shear dislocation model. In this model, the fault is represented by a discontinuity in

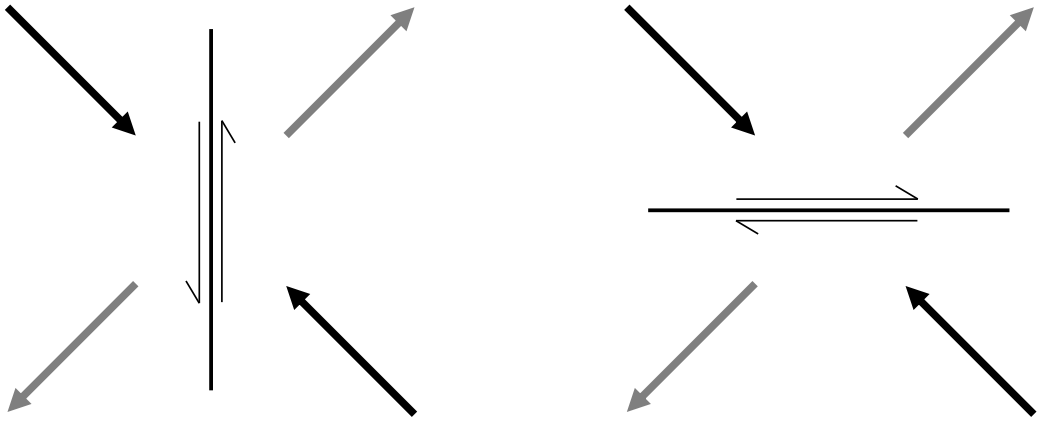

Figure 2.8. Two shear dislocation fault models that produce the same seismic wave radiation pattern. The left model is a left-lateral north-south striking fault and the right model is a right-lateral east-west striking fault. The black and gray arrows show the P and T axes of the corresponding double couple source model, respectively.

a medium which separates the two volumes that slide past one another. If the wavelength of the radiated waves is reasonably greater than the size of the fault, the shear dislocation model produces the same seismic wave radiation pattern as the double couple model. Two shear dislocations that produce identical wave radiation patterns to one another, as well as to the double couple models in Figure 2.7, are shown in Figure 2.8. The black and gray arrows indicate the P and T axes for the double couple model (as shown in the right side of Figure 2.7), respectively. Looking at both shear dislocation models illuminates one problem to keep in mind: there are two different models that produce identical seismic wave patterns. The left model is a left-lateral north-south striking fault, while the right model is a right-lateral east-west striking fault.

2.5 Focal Mechanism

A focal mechanism describes the type of slip that occurs during an earthquake. Sometimes referred to as a fault-plane solution, it contains information about the orientation of the slipping fault as well as the slip vector itself. The most common graphical representation

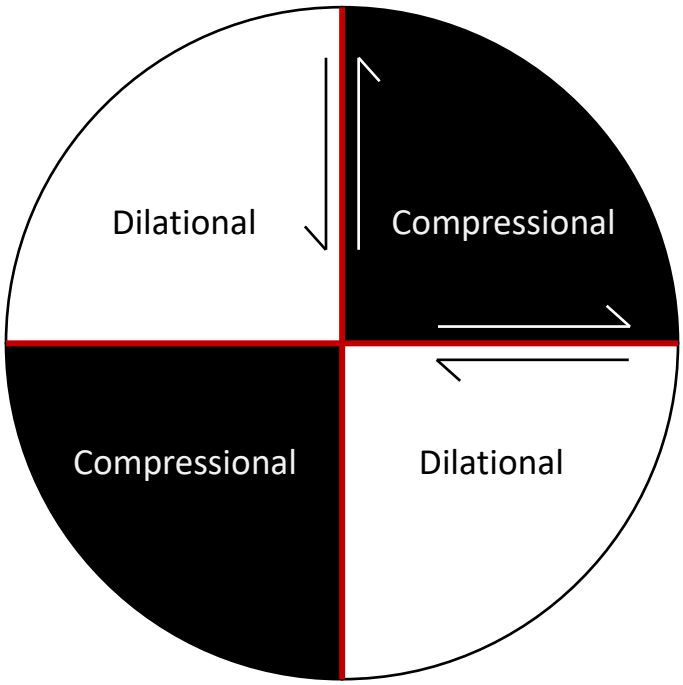

Figure 2.9. A sample focal mechanism of the models in Figures 2.7 and 2.8. This focal mechanism could be the result of either a left-lateral north-south striking fault or a right-lateral east-west striking fault. The red lines indicate the strike of each possible fault. Both faults have a dip angle of 90°.

of a focal mechanism is the so-called "beachball" diagram. Figure 2.9 shows what the beachball diagram looks like for the models in Figures 2.7 and 2.8. The red lines indicate the two possible fault planes and the arrows indicate their direction of slip.

Focal mechanisms are typically calculated using P-wave first motions. First motions are the direction of ground motion when the P-wave generated by an earthquake first arrives at a seismometer. To calculate the focal mechanism you need a sufficient number of seismograms containing first motion data.

To begin, the first motion measurements are projected onto the lower hemisphere of a sphere centered at the hypocenter of the earthquake as shown in the left portion of

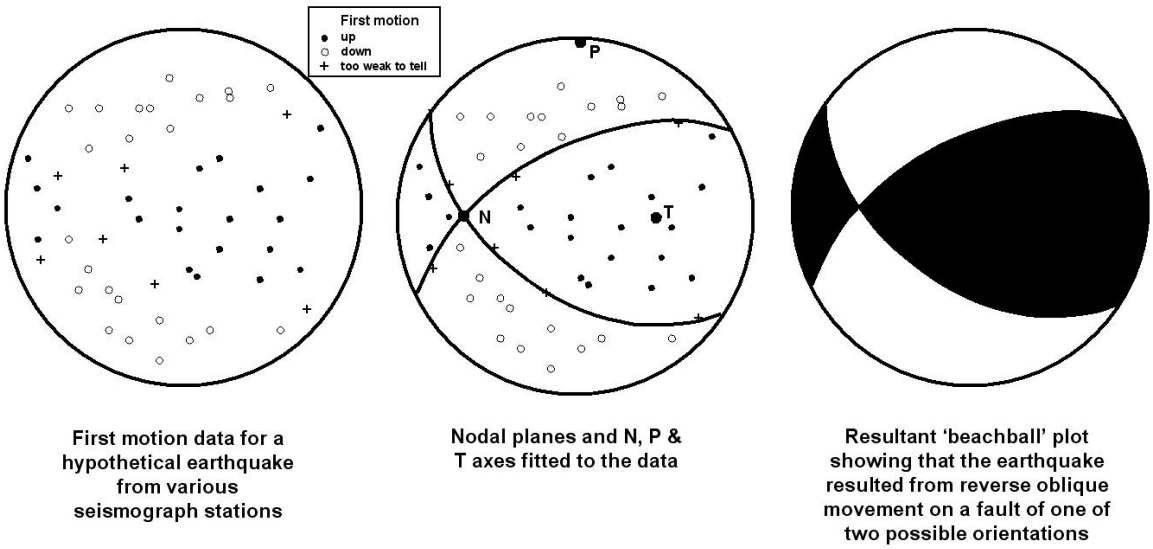

Figure 2.10. The typical process used to calculate the focal mechanism and resulting beachball diagram of an earthquake [4].

Figure 2.10. The next step is to determine the nodal planes by drawing two orthogonal great circles that separate the compressive observations (upward motion) from the tensional observations (downward motion) and therefore show the locations at which no displacement was measured. The middle portion of Figure 2.10 displays the nodal planes, as well as the N (null), P (pressure) and T (tension) axes. The P axis indicates the direction of maximum compressive stress, while the T axis indicates the direction of minimum compressive stress. Finally, the quadrant containing the T axis is colored black and the quadrant containing the P axis is colored white as shown on the right side of Figure 2.10. With this shading convention, black indicates motion toward that quadrant and white indicates motion away from that quadrant. However, the solution is still ambiguous—there are two valid solutions that yield the same focal mechanism as pointed out in the previous section. The focal mechanism alone is not sufficient to determine which of the nodal planes is parallel to the actual fault plane. Therefore, additional information is necessary to remove the ambiguity—usually other geologic information such as models of tectonic slip.

2.6 Moment Tensor

The moment tensor is the mathematical representation of an earthquake's focal mechanism that is based on the double couple source model. It contains all of the information necessary to define the earthquake's fault plane and both the type and amount of slip that occurs. That information is contained in the 9 elements of the 3x3 matrix in Equation 2.1. Each element of M_{kj} represents a single force couple, each of which are shown in Figure 2.11. The couples are arranged in the same order as their corresponding matrix elements. M_{kj} is a symmetric matrix, meaning that only 6 elements are necessary to fully define it. The diagonal elements of M_{kj} are linear vector dipoles, and so represent the normal forces in each direction. The off-diagonal elements make up three double couples (explained in Section 2.4) representing shear forces about each axis. For example, M_{12} and M_{21} form a double couple of forces that cause shear about the 3 axis.

$$M_{kj} = \begin{bmatrix} M_{11} & M_{12} & M_{13} \\ M_{21} & M_{22} & M_{23} \\ M_{31} & M_{32} & M_{33} \end{bmatrix} \tag{2.1}$$

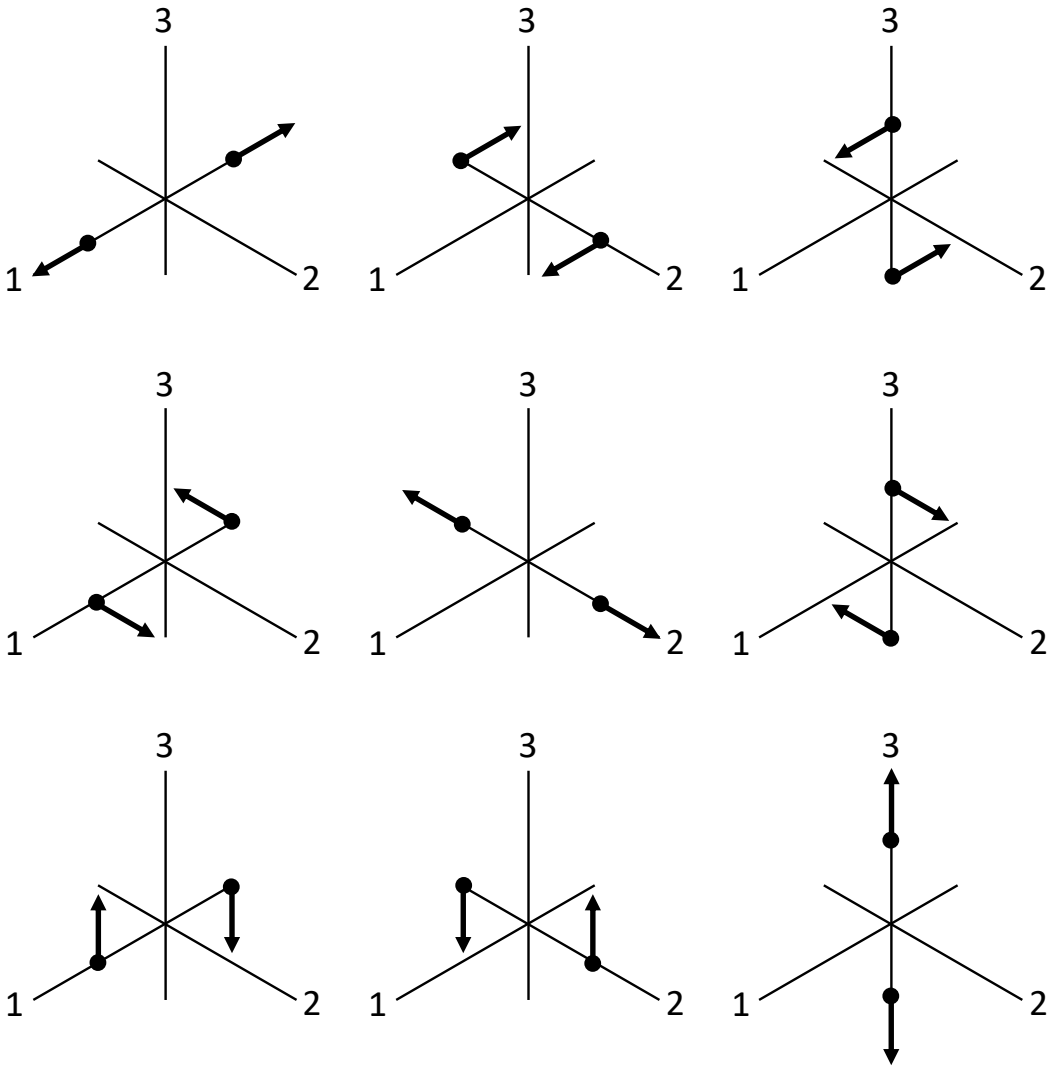

Figure 2.11. The force couples associated with each element in the moment tensor. Each couple in the 3x3 grid corresponds to the element of the moment tensor in the same location (i.e. the top left double couple represents the moment tensor component M_{11}). The diagonal elements are those representing the normal forces on the fault, while the off-diagonal elements combine to form double couples that define the shear forces on the fault.

Chapter 3

Okada's equations

Okada's equations for ground deformation are commonly used in the modeling and characterization of earthquake sources. They are a set of closed analytical expressions for the surface deformation, strains, and tilts caused by inclined shear and tensile faults in a semi-infinite elastic half-space. The geometry of Okada's rectangular source model can be seen in Figure 3.1. The point source model has a similar set of parameters but rather than having a length and width as portrayed in Figure 3.1 it is represented as a point located at the coordinates (0, 0, -d). The homogeneous, isotropic, elastic medium exists in the volume below the $z = 0$ plane. The parameters required to calculate the ground deformation field of a point source are then as follows: the depth d, the dip angle δ and the elementary dislocation U_i. The elementary dislocations U_1, U_2 and U_3 are the strike-slip, dip-slip and tensile components of the fault slip, respectively. We only use the surface deformation of shear faults in our models so we will limit our discussion to those equations in particular. The surface deformation equations and their dependence on the above-mentioned parameters are shown in Equations 3.1-3.6.

$$u_x^0 = -\frac{U_1}{2\pi}\left[\frac{3x^2q}{R^5} + I_1^0 sin(\delta)\right]\Delta\Sigma \tag{3.1}$$

$$u_y^0 = -\frac{U_1}{2\pi}\left[\frac{3xyq}{R^5} + I_2^0 sin(\delta)\right]\Delta\Sigma \tag{3.2}$$

$$u_z^0 = -\frac{U_1}{2\pi}\left[\frac{3xdq}{R^5} + I_4^0 sin(\delta)\right]\Delta\Sigma \tag{3.3}$$

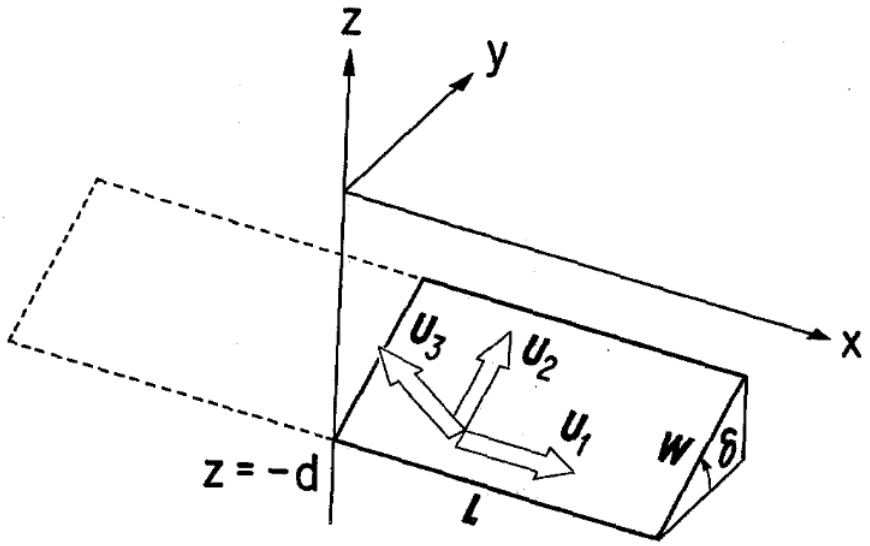

Figure 3.1. Geometry of the source model as defined in [5]. The fault of length L and width W is located at a depth d. The fault slips according to the elementary dislocations U_1, U_2 and U_3.

$$u_x^0 = -\frac{U_2}{2\pi}\left[\frac{3xpq}{R^5} - I_3^0 sin(\delta)cos(\delta)\right]\Delta\Sigma \tag{3.4}$$

$$u_y^0 = -\frac{U_2}{2\pi}\left[\frac{3ypq}{R^5} - I_1^0 sin(\delta)cos(\delta)\right]\Delta\Sigma \tag{3.5}$$

$$u_z^0 = -\frac{U_2}{2\pi}\left[\frac{3dpq}{R^5} - I_5^0 sin(\delta)cos(\delta)\right]\Delta\Sigma \tag{3.6}$$

Equations 3.1-3.6 represent the x, y and z components of the displacement at the point (x, y, 0) caused by a point source located at (0, 0, -d). U_1 and U_2 indicate the strike-slip and dip-slip components of an arbitrary dislocation, respectively. Therefore, Equations 3.1-3.3 are the displacement components of a pure strike-slip source while Equations 3.4-3.6 are the displacement components of a pure dip-slip source. The variables in Equations 3.1-3.6 are defined by:

$$p = ycos(\delta) + dsin(\delta)$$

$$q = ysin(\delta) - dcos(\delta)$$

$$R^2 = x^2 + y^2 + d^2$$

$$I_1^0 = \frac{\mu}{\lambda+\mu} y \left[\frac{1}{R(R+d)^2} - x^2 \frac{3R+d}{R^3(R+d)^3} \right]$$

$$I_2^0 = \frac{\mu}{\lambda+\mu} x \left[\frac{1}{R(R+d)^2} - y^2 \frac{3R+d}{R^3(R+d)^3} \right]$$

$$I_3^0 = \frac{\mu}{\lambda+\mu} x \left[\frac{x}{R^3} \right] - I_2^0$$

$$I_4^0 = \frac{\mu}{\lambda+\mu} \left[-xy \frac{2R+d}{R^3(R+d)^2} \right]$$

$$I_5^0 = \frac{\mu}{\lambda+\mu} \left[\frac{1}{R(R+d)} - x^2 \frac{2R+d}{R^3(R+d)^2} \right]$$

where μ and λ are the Lamé parameters. The Lamé parameters define the elastic behavior of homogeneous, isotropic media—more specifically, the relationship between the components of the elastic stress and the components of the deformation. For our purposes, we slightly alter the equations to be written in terms of seismic moment, defined in [5] to be $M_1 = \mu U_1 \Delta\Sigma$ and $M_2 = \mu U_2 \Delta\Sigma$ for strike-slip and dip-slip sources, respectively. So in Equations 3.1-3.6, $U_i \Delta\Sigma$ is replaced with $\frac{M_i}{\mu}$ of the appropriate i value for each equation.

In order to represent a wider variety of earthquake sources our model needs a few additional parameters—horizontal position, strike angle, and rake angle. These don't show up in the simplest forms of Okada's equations because each one can be added through a coordinate transformation or by finding the components of the slip in terms of the elementary dislocations. The horizontal position of a source can be changed through a translation of the x and y coordinates. Strike angle can be added as a rotation about the z axis. Since rake angle tells us the direction of slip along the fault itself, it is included through a combination of the elementary dislocations U_1 and U_2 for a shear fault. Figure 3.2 shows the geometry of the point source model with the addition of these new parameters. δ still refers to the dip angle as before, while ϕ and λ were added to show the strike angle and rake angle, respectively. The point source is located at the center of the dark grey rectangle, which we added to allow easier visualization of the parameters. The strike angle ϕ is measured relative to the x axis and the rake angle λ is measured relative to the strike direction. A strike angle of 0° would therefore be parallel to the x axis. A rake angle of 0° or 180° yields a fully strike-slip fault (entirely in the direction of

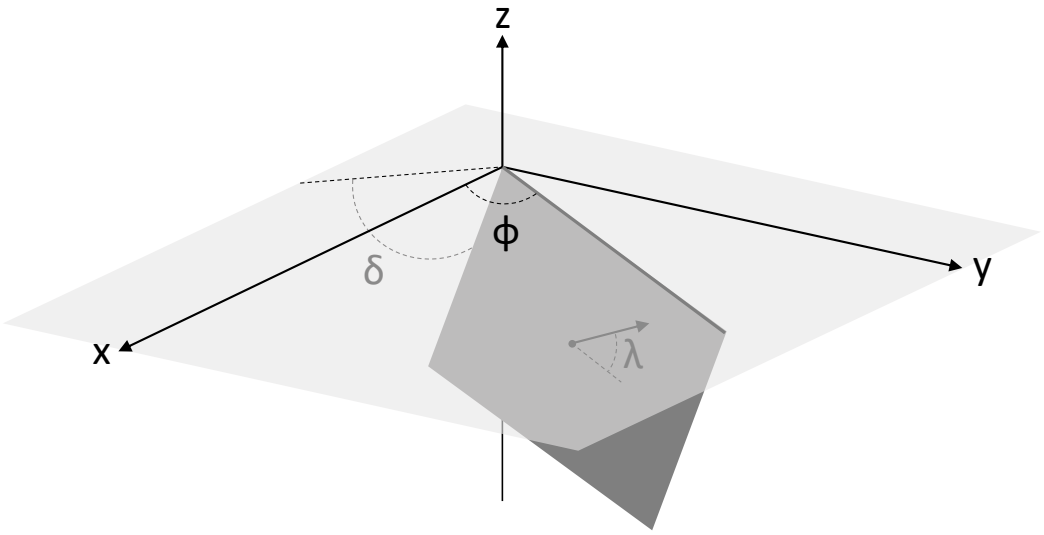

Figure 3.2. Geometry of the point source model after extending it to include strike angle (ϕ) and rake angle (λ).

elementary dislocation U_1) while a rake angle of 90° or 270° yields a fully dip-slip fault (entirely in the direction of elementary dislocation U_2). If the rake angle is any other value, the fault is oblique: a combination of strike-slip and dip-slip components.

There are a few caveats to keep in mind when using the parameters as defined in Figure 3.2. While the strike angle ϕ is measured from the x axis in Okada's convention (i.e., a strike angle of zero means the fault strike is parallel to the x axis), it is typically measured from north for actual faults. Since Okada's original equations do not include rake angle, they allow negative dip angles to reverse the direction of slip on the fault. The most common convention of dip angle restricts it to the range $0 < \delta < 90°$ measured from the horizontal and the rake angle is what determines both the type and direction of fault slip.

Figure 3.3 shows the three components of the ground displacement caused by a purely strike-slip point source. Each component is viewed from a position on the positive z axis such that the area of the plot represents an area of the earth's surface in the Cartesian coordinate system where x is horizontal, y is vertical and z is into/out of the page. The colors of each plot represent the magnitude of the displacement of each point on the ground in the direction indicated by the title of each plot. In other words, the colors of the dx plot indicate the displacement along the x axis, the dy plot the displacement

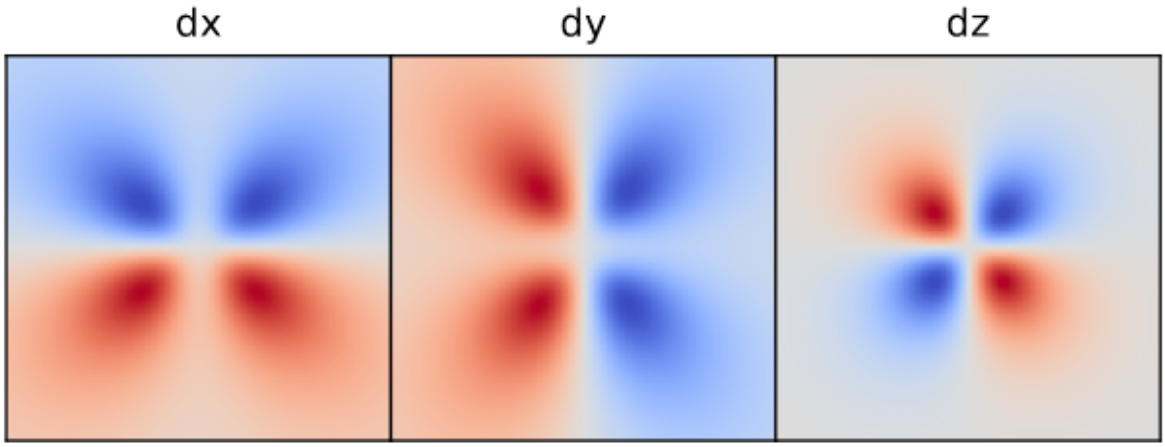

Figure 3.3. The components of the ground displacement caused by a strike-slip point source. Each component is designated by the title above each plot. Positive displacement is indicated in red, while negative displacement is indicated in blue.

along the y axis and the dz plot the displacement along the z axis. Positive displacements are blue, zero displacements are white and negative displacements are red. Darker colors indicate greater magnitude of displacement. The source used to generate the displacement in Figure 3.3 was placed at a depth of 10 km with a strike angle of 0°, dip angle of 90°, and rake angle of 0°. This means that the source is similar to an east-west striking left-lateral strike-slip fault. However, recall that since the displacement patterns are not unique, the same displacements could result from a north-south striking right-lateral strike-slip fault. Each part of the figure covers a 60 km x 60 km area and the point source is located directly in the center of each plot.

Figure 3.4 shows the three components of the ground displacement caused by a purely dip-slip point source. The only parameter that differs from the strike-slip example is the rake angle, which is set to a value of 90°. To get the ground deformation of a shear fault that is not purely strike-slip or dip-slip you combine the deformation in Figures 3.3 and 3.4, scaled by the appropriate components of the slip vector.

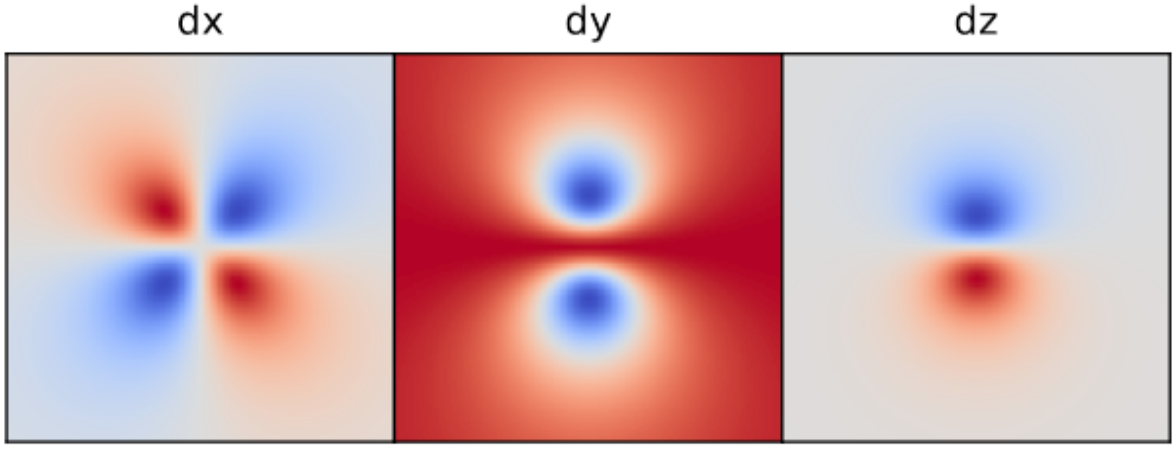

Figure 3.4. The components of the ground displacement caused by a dip-slip point source. Each component is designated by the title above each plot. Positive displacement is indicated in red, while negative displacement is indicated in blue.

Chapter 4

Interferometric Synthetic Aperture Radar (InSAR)

Interferometric synthetic aperture radar (InSAR) is a remote sensing method that utilizes multiple synthetic aperture radar (SAR) images to produce maps of the surface deformation of the earth. SAR is an active sensing technique which means that it produces the radiation used to illuminate its target. The SAR emits radiation which is scattered back to the radar by the earth's surface and then the SAR records both the amplitude and phase of the returning signal. All data recorded by the SAR is reported in the form of images. Each image is separated into pixels, and each pixel represents a small area of the earth's surface. The amplitude and phase of a given pixel's signal is determined by the scatterers that are present within the area of that pixel. A scatterer is anything that can reflect the SAR's radiation, including but not limited to: buildings, vegetation, and rocks. To allow a SAR to image any area of interest, it is generally attached to an aerial platform. The SAR looks to one side of the platform and scans an area of the ground as the platform flies by. An example of a SAR attached to an earth orbiting satellite is shown in Figure 4.1. The satellite flies along its flight path (also known as the azimuth or along-track direction) with the SAR looking to the right. The swath—the area the SAR is recording—extends in the range direction which is perpendicular to the azimuth direction. The width of the swath (as indicated in Figure 4.1) is determined by the size of the SAR antenna and the geometry of the flight path relative to the ground. The

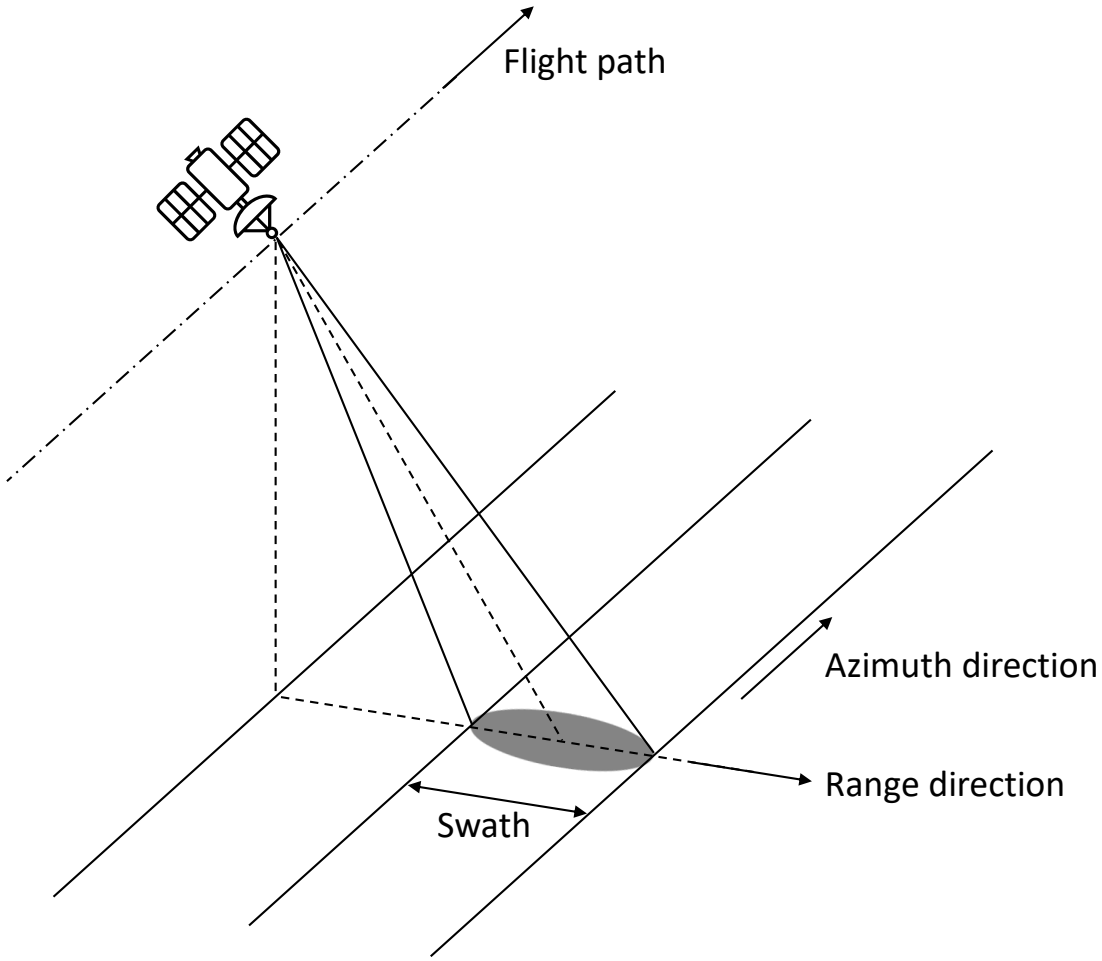

Figure 4.1. A right-looking SAR mounted on a satellite. As the satellite flies along its flight path, the SAR scans the area of the ground indicated by the gray oval. The direction of the flight path is also known as the azimuth direction and the range direction is perpendicular to it. The resulting SAR image would have the same width as the swath and its length in the azimuth direction would be determined by how long the SAR illuminated the ground as it flew by. Figure adapted from an image courtesy of NASA/JPL-Caltech.

length of the swath is determined by how long the SAR sends and receives pulses as it flies by its target area. The "synthetic" aperture of a SAR results from the motion of the platform as it illuminates its target. Because the SAR continuously sends radar pulses to the target as it moves, each pulse views the target from a different position, improving the resolution of the SAR image in the azimuth direction [43].

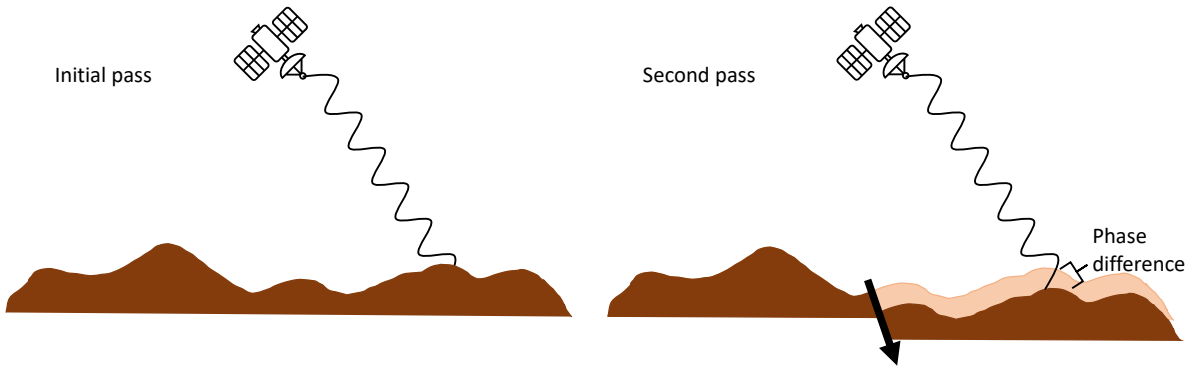

Figure 4.2. Two different SAR passes of the same area. In the initial pass, the SAR records the phase of each point on the ground. In between the passes the right half of the "ground" has subsided away from the satellite. During the second pass, the SAR again records the phase of each point on the ground, but measures a different phase for all points that shifted away from the satellite. When the phases of each image are subtracted, the result is the phase difference in the time between the two images, which can be converted to the distance that each point moved away from the satellite. Image adapted from a figure courtesy of NASA/JPL-Caltech [6].

If two SAR images of the same area are properly co-located (i.e. their pixels cover the same areas), a map of the phase difference between the two images can be produced. Since the wavelength of the radiation produced by the SAR is known, the phase differences can be converted to distances. These distances are the deformation of the ground in the line-of-sight direction of the SAR that occurred in the time between when the images were taken. Figure 4.2 shows an example in which the ground moves away from the SAR in between two different satellite passes and the phase difference that is measured as a result. Figure 4.3 shows two typical SAR images and the InSAR image that shows the phase differences between them. The leftmost SAR image was taken on November 13th, 2009 and the middle image taken on November 18th, 2010. Therefore, the interferogram on the right shows the deformation of the ground in the line-of-sight of the satellite that occurred in the year between the SAR image acquisition dates. Negative pixel values indicate motion toward the satellite and positive pixel values indicate motion away from the satellite.

Multiple InSAR images of the same area from different viewing angles are required

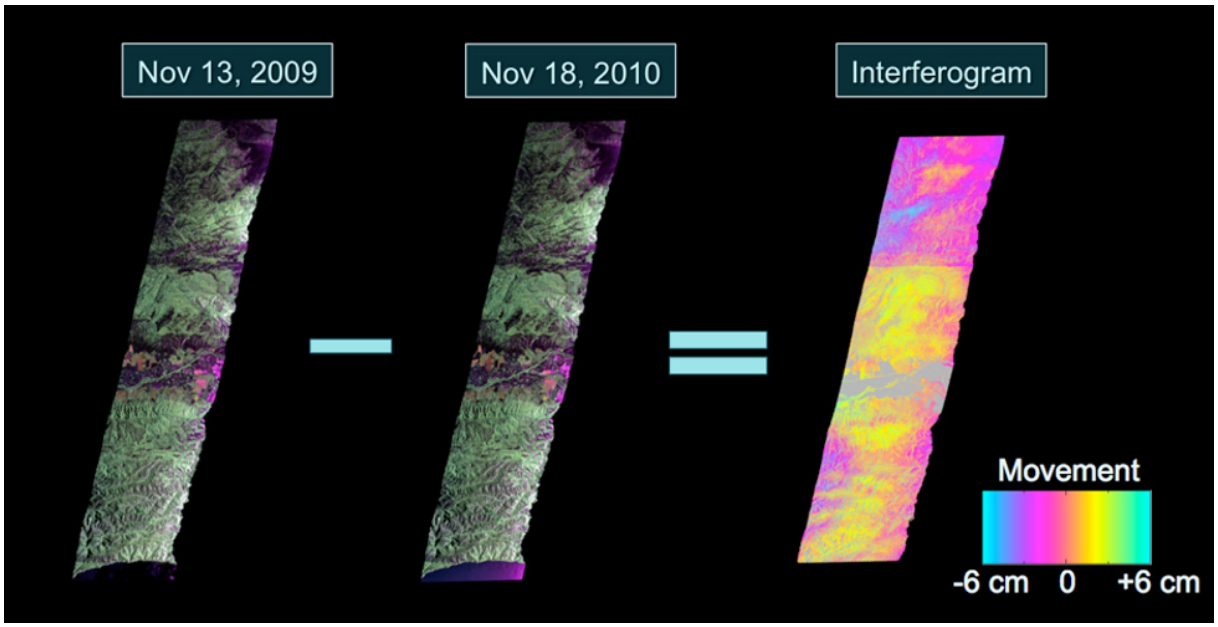

Figure 4.3. Two SAR images and their resulting interferogram. Since the images were taken at the listed dates, the interferogram shows the ground motion that occurred between those dates. The horizontal line at the sudden shift from pink to yellow indicates the San Andreas fault which slipped during this time period. Image courtesy of NASA/JPL-Caltech [6].

to determine the 3D (up-down, north-south, and east-west) components of the ground deformation. Since SARs are commonly mounted on polar-orbiting satellites, they are able to measure the same ground area with their ascending and descending tracks. The ascending track refers to the portion of the satellite's orbit when it is traveling from the south pole to the north pole while descending refers to the north pole to south pole portion of the orbit. The rotation of the earth allows the SAR to image the same area of the ground during both tracks. Figure 4.4 shows a SAR imaging the same area of the earth's surface during separate ascending and descending passes. To get estimates of the 3D ground deformation components, it would require a total of four passes: two in the ascending orbit and two in the descending orbit. Both ascending orbit SAR images are used to generate an InSAR image where each pixel represents the ground deformation in the line-of-sight of the satellite during the time period that elapsed between when the SAR images were taken. A descending orbit InSAR image is generated in the same way. This results in two overlapping InSAR images that were taken from different viewing

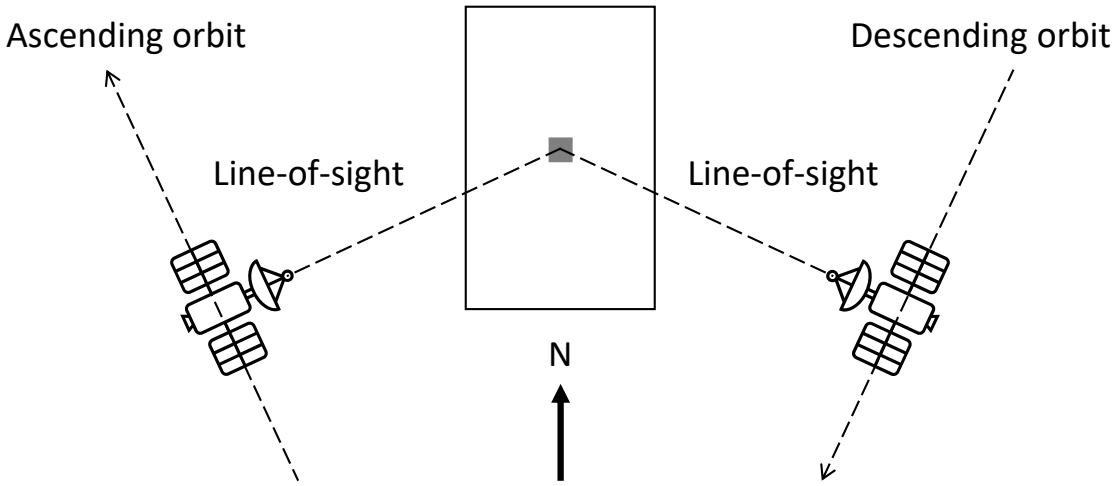

Figure 4.4. An ascending and descending pass of the same ground area by a single satellite mounted SAR. Since the SAR is always right-looking relative to the flight path, it views the area from different sides during each pass.

geometries, giving each pixel two vectors that describe the ground deformation of that pixel. The 3D components of the ground deformation can then be estimated using the constraints provided by the line-of-sight vectors. In general, more overlapping images with different line-of-sight geometries means better estimates of the 3D ground deformation.

Chapter 5

First Iteration: The Genetic Algorithm

As their name implies, genetic algorithms borrow their method of solving problems from genetics. A population of solutions to the problem is randomly generated, and these solutions are allowed to crossover and mutate until an ideal solution is found. A crossover operator is the genetic algorithm equivalent of parents giving birth to offspring that inherit their genes. In a traditional genetic algorithm, a solution is represented as an array of bits, and the crossover operator might be defined to swap certain bits between two "parent" solutions. The mutation operator randomly changes the value of one or more bits in a solution array, similar to what occurs during a long period of a species' evolution. A genetic algorithm also requires some form of "survival of the fittest," which allows better solutions to be chosen to move forward during the execution of the algorithm. This is included in the algorithm as a fitness function—more "fit" solutions to the problem are those who maximize the fitness function or some other desired measure of fitness [44].

In this chapter, we utilize what is known as a real-coded genetic algorithm, in which the solutions are instead represented by a list of real-valued parameters. This change in the form of the solutions necessitates a change in the genetic operators, which will be explained in Section 5.1. Our goal is to use this algorithm to determine the best-fit parameters of our point source model from InSAR data.

5.1 Genetic Algorithms

We begin by describing our genetic algorithm in more detail. As stated in the previous section, the solutions in a real-coded genetic algorithm are represented as lists of real-valued parameters. For the genetic algorithm used in this chapter, the solutions are a list of parameters that describe the locations and orientations of a number of seismic point sources. In particular, every point source has a parameter for each of the following: x coordinate, y coordinate, z coordinate, strike angle, dip angle, and seismic moment. The x, y, and z coordinate parameters define the location of the point source in three-dimensional space—where z = 0 defines the ground's surface in the case of zero deformation. The strike angle and dip angle determine the orientation of the slipping fault represented by the point source. Strike angle determines the direction of the line created by the intersection of the fault plane and the ground's surface. The dip angle is the angle between the fault plane and the ground's surface. A diagram of the geometric parameters can be seen in Figure 2.6. In Okada's convention, the dip angle is restricted to lie within the range $-\frac{\pi}{2} < \delta < \frac{\pi}{2}$ [5]. The seismic moment of a point source represents a combination of the fault area and the amount that it slips. A solution will have 6n parameters total, where n is the number of point sources the solution is composed of. These point sources give rise to surface deformation as defined by Okada's expressions for deformation due to shear and tensile faults in a half-space [5]. Our analysis utilizes these equations, which are included in Chapter 3. The total deformation—the superposition of the deformation from all point sources—is compared to a desired surface deformation (the data), and the goal of the algorithm is to move and reorient the point sources until the model's surface deformation approximates that of the data. The specifics of the algorithm are discussed in the following paragraphs.

Given some ground deformation data in the form of ground coordinates and their corresponding deformations, the algorithm first determines the minimum and maximum x- and y-values to use as limits when generating possible source distributions to fit the data. This restricts the allowed locations of the point sources to an area below the ground deformation. Then the algorithm generates a population of a user-defined number of source

distributions (models) containing a user-defined number of sources with random locations and orientations within specified limits. It calculates each model's displacement field, which is the ground deformation resulting from a superposition of the ground deformation due to individual point sources in the model. Each model is compared to the input data, and the chi-squared value of each model is recorded. In this chapter, the chi-squared value for a given model is defined as:

$$\chi^2 = \sum_{i=1}^{n} (z_i - f(x_i, y_i))^2 \tag{5.1}$$

where z_i is the data value for the elevation of the ground at the point (x_i, y_i), $f(x_i, y_i)$ is the model value for the elevation of the ground at the point (x_i, y_i), and i runs over all data points.

After the chi-squared of each model has been determined, pairs of models are selected to use as parents in the creation of the next generation of models. The models with lower χ^2 are more likely to be selected as parents. Note that the same model cannot be both members of a pair, but can be present in more than one pair with another model. As each pair is selected, the member models are crossed to yield two more next-generation models.

This chapter uses what is called a simulated binary crossover operator to generate new solutions based on the parent solutions [45]. We choose simulated binary crossover because it provides improved performance compared to the typical random crossover of basic genetic algorithms. It is the real-coded equivalent of the single-point crossover operator of a binary genetic algorithm. The single-point crossover operator crosses the parent solutions by picking a random point in one solution's bit array, and swaps the bits after that point between the two solutions. Simulated binary crossover uses a probability density function to imitate single-point crossover for use in a real-coded genetic algorithm. Simulated binary crossover works as follows:

1. Choose two parents x_1 and x_2

2. Generate a random number $r \in [0, 1)$

3. Calculate the parameter β

$$\beta = \begin{cases} (2r)^{\frac{1}{\eta_c+1}} & \text{if } r \leq 0.5 \\ \left(\frac{1}{2(1-r)}\right)^{\frac{1}{\eta_c+1}} & \text{otherwise} \end{cases}$$

where η_c is the distribution index.

4. Compute the child solutions using

$$x_1^{new} = 0.5[(1+\beta)x_1 + (1-\beta)x_2]$$
$$x_2^{new} = 0.5[(1-\beta)x_1 + (1+\beta)x_2]$$

The distribution index determines the width of the distribution used for generating children. Large values of η_c tend to generate solutions closer to the parents, while smaller values generate solutions further away. The recommended value for η_c, and the one used in this chapter, is $\eta_c = 2$ [45]. Pairs are selected and crossed until the next generation becomes equal in size to the original population of models.

Once the next generation has been created, there is a user-defined chance for each model in the new generation to be mutated. The mutation operator—when applied to a model—gives each source in the model a user-defined chance to be shifted from its original position, orientation, and seismic moment. The amount of translation or rotation is determined by a Gaussian random number generator centered at the original value of the coordinate. For example, if the original strike angle of a source is $\pi/2$, the Gaussian distribution used to select the new value has a mean value of $\pi/2$. The amount of shift in the location and seismic moment is selected in a similar manner. The process of crossing to create new generations and mutation of the new generations is repeated until the user-defined number of generations is reached. In general, the "user-defined" parameters represent a trade-off between computation time and accuracy. There is no one correct value, and appropriate values can vary widely between applications.

5.2 Applying the Genetic Algorithm to Randomly Generated Data

To generate the synthetic data for testing the algorithm, an interferogram was generated by placing 10 point sources at random positions and orientations. The positions are restricted within a cuboid defined by the limits $0 < x < 30$ km, $0 < y < 10$ km and $-10 < z < -3$ km. The data points at which the generated data and models are compared lie within the same x and y bounds. 30 data samples were taken in the x-direction and 10 data samples in the y-direction, yielding a total of 300 data points—each a square with a side length of $1km$. The sources were placed with random strike and dip angles in the ranges $0 < \phi < 2\pi$ and $0 < \delta < \frac{\pi}{2}$, respectively, as well as random seismic moment in the range $10^8 < M_0 < 10^{12}$ Nm. The total ground deformation was calculated as a result of the superposition of the ground deformation of all placed sources—with each point source causing a ground deformation according to Okada's equation for the vertical displacement of a strike-slip seismic source. Horizontal deformation was not considered in this example.

The generated interferogram was fit using 10 point sources. The starting values of the parameters in the initial population of solutions were chosen from uniform distributions for each parameter. As stated before, the x and y coordinates of the initial population of sources lie within the range of the data points. The initial depth of the sources and their initial strike and dip angles were restricted to the same ranges used to generate the interferogram. The algorithm ran for 10000 generations with the spreads in Table 5.1 used to mutate each parameter. In Table 5.1, the half order of magnitude spread for seismic moment means that a Gaussian distribution was used to generate a power of 10 that was used as the new seismic moment. For example, if the original value of the seismic moment was 2.4×10^5, a Gaussian distribution centered at $log_{10}(2.4 \times 10^5)$ with a standard deviation of 0.5 was used to generate a random number r. The new value of the seismic moment is then 10^r. The chance for a model to be chosen to mutate in a given generation was 20%. If chosen to mutate, each source point in the model had a 10% chance to have its location, strike angle, dip angle, and seismic moment changed

Parameter	Amount of Spread
x	2 km
y	2 km
z	0.5 km
Strike angle	$\pi/6$
Dip angle	$\pi/24$
Seismic moment	Half order of magnitude

Table 5.1. The standard deviations of the Gaussian distributions used to mutate the parameters.

according to the above values of spread in each parameter. During the execution of the algorithm, the only restriction on the evolution of the sources is that their dip angles must remain in the range $0 < \delta < \frac{\pi}{2}$ as in Okada's convention—every other parameter is allowed to evolve freely according to the rules of the crossover and mutation operators. The model resulting from the fit is compared to the data in Figure 5.1.

5.3 Applying the Genetic Algorithm to ALOS-2 Data

The InSAR interferogram that is fit in this chapter was processed by [46] and was downloaded from the Nepal Earthquake ALOS-2 InSAR website [9]. The particular interferogram used is the sum of the ALOS2040533050-150222 and ALOS2050883050-150517 products, yielding an interferogram containing ground displacement between February 22nd, 2015 and May 17th, 2015. This interferogram was chosen because it exhibits deformation due to two seismic events—in this case, the magnitude 7.8 earthquake that occurred on April 25th, 2015, 36 km east of Khudi, Nepal, and its magnitude 7.3 aftershock that occurred on May 12th, 2015. The interferogram is a collection of points, each defined by their latitude, longitude, and line-of-sight ground displacement. The line-of-sight displacement is converted to vertical displacement using the reported look angle of the satellite for each data point. To fit this interferogram, the data are binned into a 30-by-30 two-dimensional histogram to reduce the amount of computation time. The value

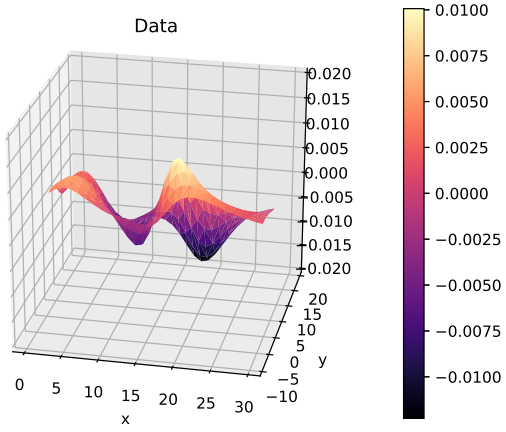

(a)

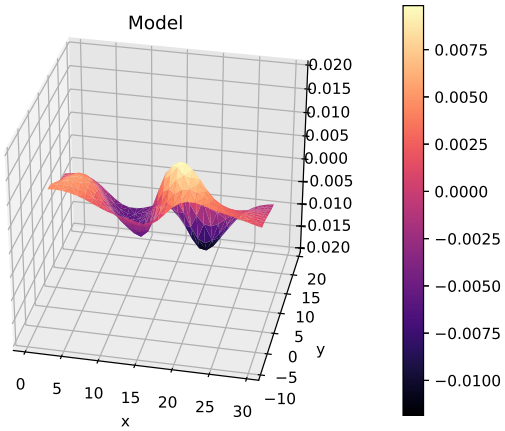

(b)

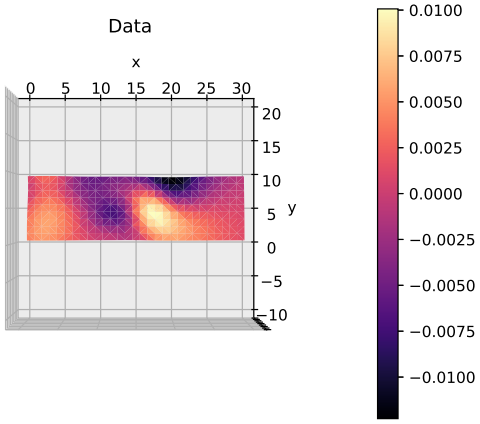

(c)

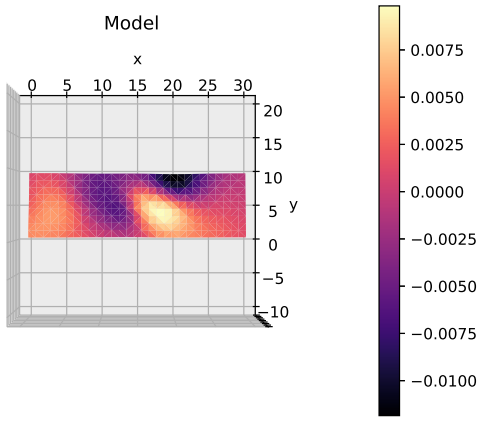

(d)

Figure 5.1. (a) Azimuthal view of the synthetic ground deformation data. (b) Azimuthal view of the model generated by the algorithm. (c) Top view of the synthetic ground deformation data. (d) Top view of the model generated by the algorithm.

of each bin is calculated as the average vertical displacement of each data point contained in that bin. After binning, the resulting pixels in latitude and longitude are mapped to the x-y plane, in units of km, to allow comparison to the results of the algorithm. To further reduce computation time, the area of the interferogram being fit is reduced to pixels in the range $40 < x < 240$ km and $70 < y < 200$ km, which contains the ground deformation of interest.

When fitting this interferogram, the algorithm is set to use a population size of 500, with each solution in the population containing 15 seismic point sources. The earthquake was a result of thrust faulting [47], and so Okada's equations for dip-slip faulting were used to calculate the ground deformation caused by the point sources. For this example, only the vertical displacement of the ground was calculated—the horizontal displacement was not considered. After running for 15000 generations, taking about 7400s to run, the algorithm returned the model visible in Figure 5.2. The distribution of the point sources can be seen in Figure 5.3. The residuals between the model and data can be seen in Figure 5.4. This run of the algorithm used the same parameters for spread and mutation probability as outlined in Table 5.1 and Section 5.2, respectively. The initial values of the point source parameters in the starting population are chosen from uniform distributions. The ranges of the x and y coordinates are limited to the dimensions of the interferogram area above and the depth ranged from $-30 < z < -20$ km. The strike and dip angles ranged from $0 < \phi < 2\pi$ and $0 < \delta < \frac{\pi}{2}$, respectively. The seismic moments are pulled from the range $10^9 < M < 10^{12}$ Nm. The parameters found by the algorithm for each point source can be seen in Table 5.2. These parameters are included for the sake of completeness; however, the goal of the current algorithm is to recreate the input ground deformation data, rather than to claim that it yields more accurate fault parameters than other inversion methods.

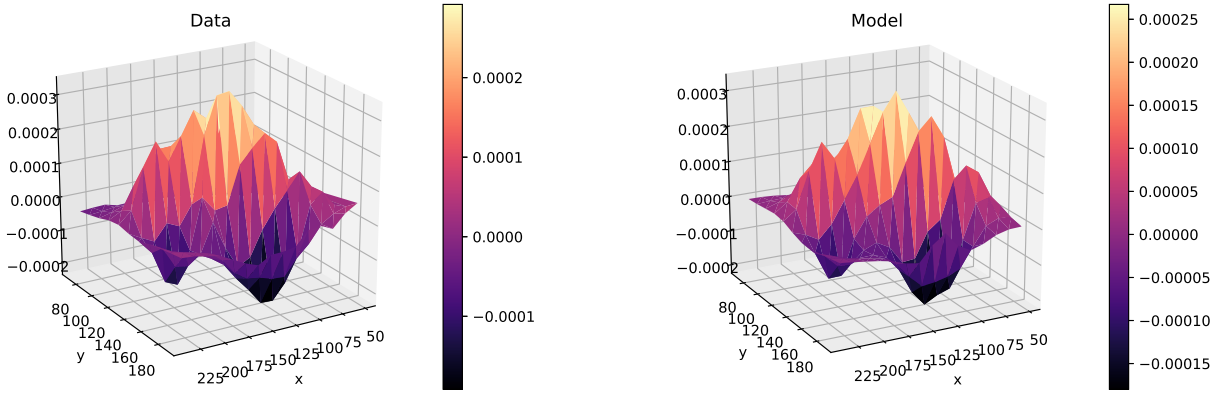

(a)

(b)

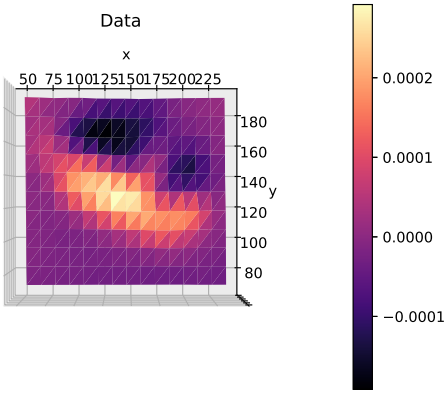

(c)

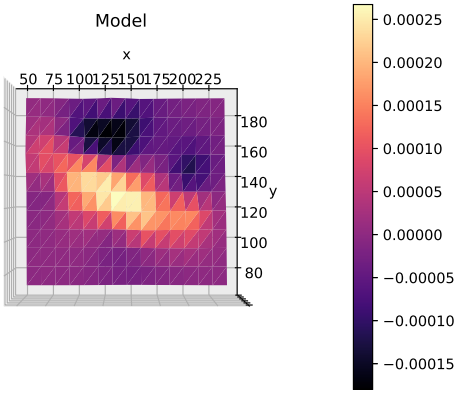

(d)

Figure 5.2. (a) Azimuthal view of the ALOS-2 ground deformation data. (b) Azimuthal view of the model generated by the algorithm. (c) Top view of the ALOS-2 ground deformation data. (d) Top view of the model generated by the algorithm.

	x	y	z	strike	dip	moment
1	69.8468	177.091	-29.9032	-0.45963	1.0839	0.13784
2	106.367	97.4588	-32.8588	6.61252	0.479722	168801
3	150.058	78.0384	-33.6847	19.0313	0.307234	1.23221e+09
4	140.425	191.588	-28.8003	5.79284	0.27404	1.90518e+10
5	202.588	127.159	-22.7864	0.111355	1.51411	2.05646e+10
6	72.8359	123.785	-17.2656	12.2768	1.4786	1894.74
7	131.227	132.126	-21.8409	6.72117	1.14697	1.06253e+10
8	143.966	118.57	-23.2668	3.75185	1.28514	1.53379e+10
9	73.7351	144.747	-21.1349	2.96139	1.4699	9.02219e+09
10	163.803	108.866	-29.3693	6.3945	0.352603	1.93104e+10
11	102.768	151.892	-22.8624	3.53234	0.0142592	2.29585e+10
12	181.87	89.2093	-36.7044	4.76648	0.0305045	4.18498e+09
13	126.37	151.843	-27.464	0.494327	1.51399	2.4217e+10
14	237.313	230.565	-26.7075	0.469047	1.12608	5.72458e+09
15	143.542	133.469	-26.0931	6.43808	1.21437	626.352

Table 5.2. The parameters found by the algorithm for each point source in the ALOS-2 data fit. The strike and dip angles are recorded in radians and seismic moment in Nm. Recall that these parameters use Okada's convention, where a strike angle of zero means the strike is parallel to the x axis.

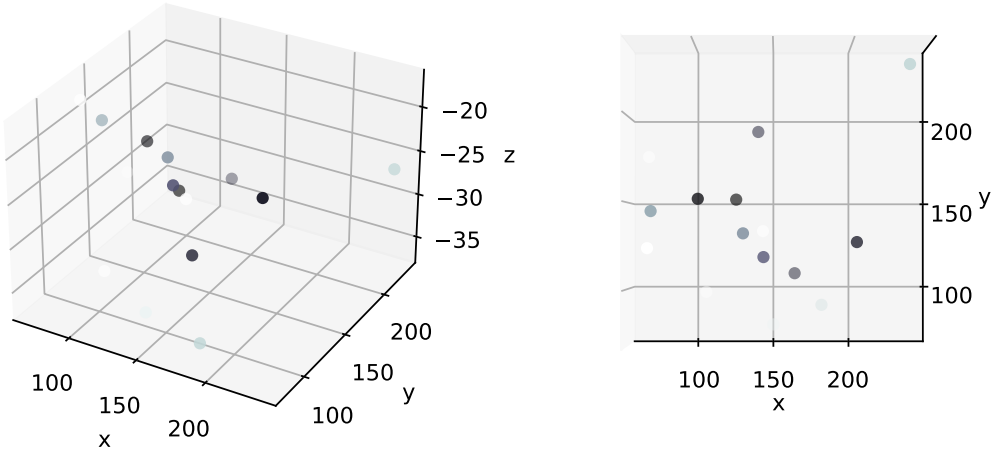

Figure 5.3. An azimuthal (left) and top-down (right) view of the 3D distribution of point sources resulting from the genetic algorithm fit. The parameters of the sources are outlined in Table 5.2. The points are colored according to their seismic moment—darker points have a higher seismic moment, while lighter points have lower seismic moment.

5.4 Performance of the Algorithm On a Single-Source Interferogram

To quantify the performance of the algorithm, a third interferogram was generated so that multiple fits could be performed and to investigate the effect of changing the parameters on the error of the model. The interferogram was generated from a single point source whose parameters were selected at random from reasonable uniform distributions in each parameter. The parameter values used to generate the interferogram, referred to as the true values in the following text, were 48.5774, 43.6555, -10.4041, 5.25892, 0.523487, and 8.29375e+09 for x, y, z, strike angle, dip angle, and seismic moment, respectively. After 50 fits of the aforementioned interferogram, the standard deviations of the parameters were 0.695, 0.6, 0.329, 0.099, 0.184, and 5.36e+09 for x, y, z, strike angle, dip angle, and

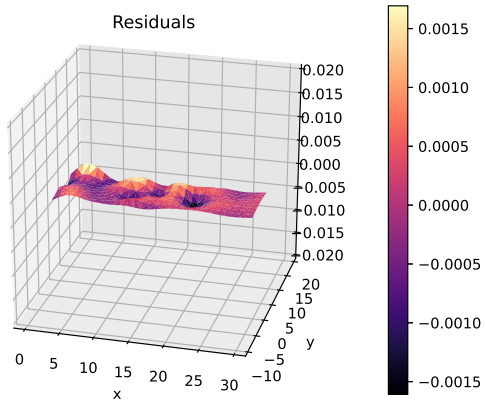

(a)

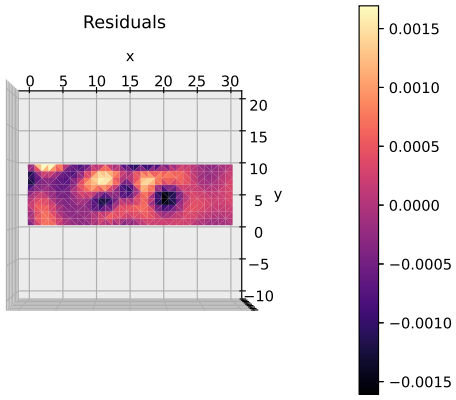

(b)

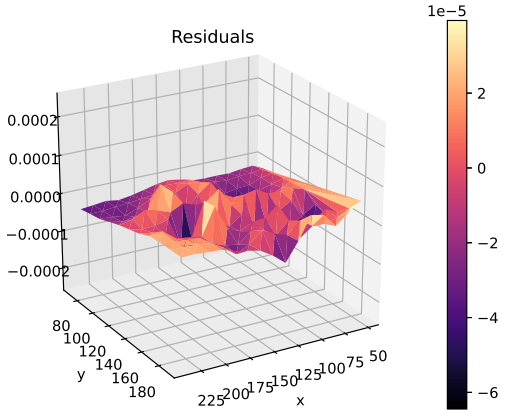

(c)

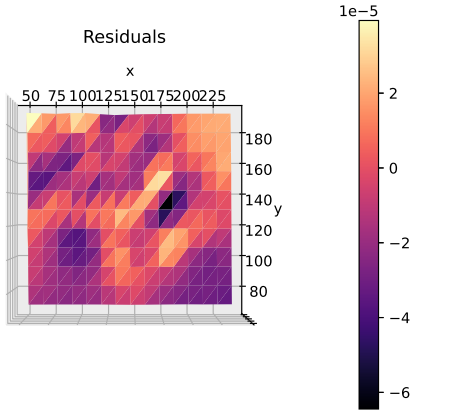

(d)

Figure 5.4. (a) Azimuthal view of the residuals between the synthetic ground deformation data and the corresponding model. (b) Top view of the residuals between the synthetic ground deformation data and the corresponding model. (c) Azimuthal view of the residuals between the ALOS-2 ground deformation data and the corresponding model. (d) Top view of the residuals between the ALOS-2 ground deformation data and the corresponding model.

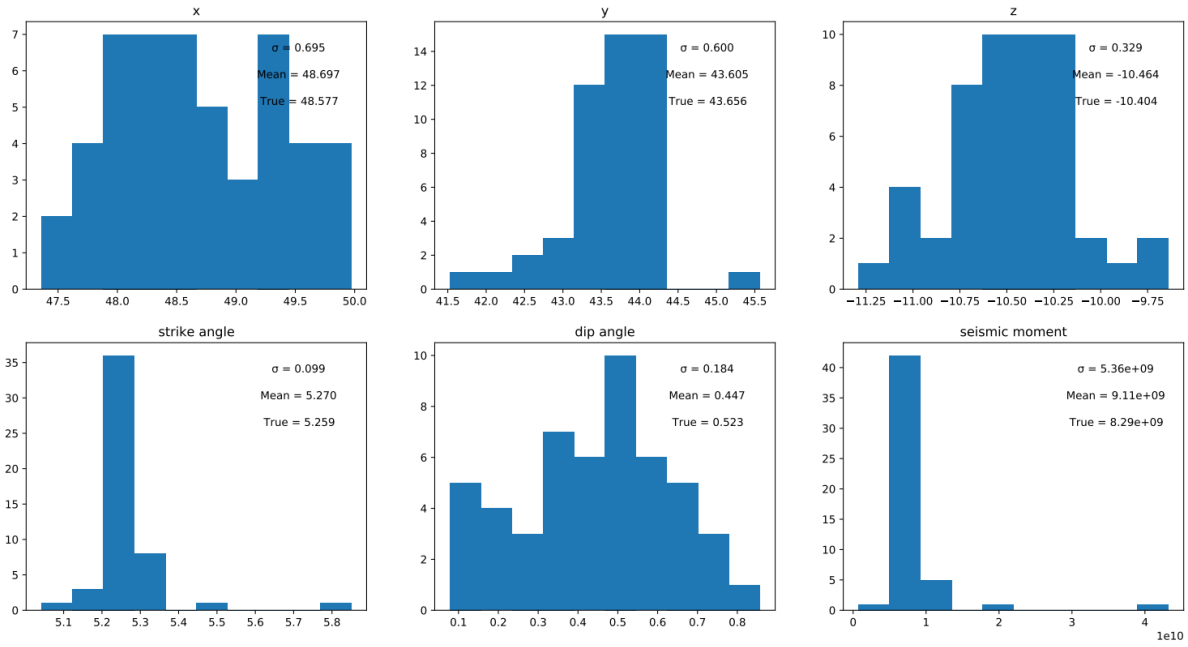

Figure 5.5. Histograms of the final parameter values found from 50 different fits of the same single-source interferogram.

seismic moment, respectively. Histograms of the values for each parameter resulting from the different fits can be seen in Figure 5.5. For all parameters, the mean of all fits lies within a single standard deviation of the true value.

The seismic moment standard deviation, however, is comparable in magnitude to the true value. This is likely due to the wide range of possible values allowed for the seismic moment in the algorithm, which spans over 3 orders of magnitude to allow a wide search space. Seismic moment also contains one of the most significant outliers due to its large range of possible values, so this could perhaps be improved by limiting the parameter space of the model.

In order to further characterize the relationships between the parameters of the model, we varied different pairs of parameters to see how the error in the displacement map was affected. We use a simple definition of error here: the sum of the squared residuals between the model and data. The "error maps" are displayed in Figure 5.6. As an example, the top left plot (in a landscape view) shows the error as a function of both x and y, with all other parameters fixed at the true values listed above. The purpose of these plots is to search for correlations that may exist between the parameters. One that can be clearly

seen is the inverse relationship between seismic moment and depth z. Another observation is that dip angle greatly affects the error of the fit regardless of which other parameter is being varied. In the dip angle v. strike angle plot, strike angle varies over a range of over 120° and the error slowly increases as it moves away from the true value. However, changes in the dip angle, which varies only around 40°, rapidly move toward higher error.

5.5 Changes to the Algorithm

One of the biggest problems with this algorithm is that there is a huge amount of freedom in the final model. Each point source has six possible parameters with very few restrictions placed upon them, so every fit yields different model parameters that all approximate the same ground deformation. There are two ways to easily impose restrictions that reduce the number of possible solutions. One is to increase the amount of data used in the fit, especially the inclusion of data with more components of the deformation. We are limited by the data itself and computation time so such an improvement is not viable for this case. We can only get accurate estimates of the z component of the deformation from the interferograms we have and if we increase the number of data points we increase the computational complexity of the problem. Instead, we can narrow our parameter space by utilizing previous fits of the same event and fixing the values of some of our parameters. This will both reduce the computational complexity of the problem and simultaneously reduce the parameter space.

To implement these changes into the algorithm, we fix every parameter of the point sources except for their seismic moment and place them into a grid that lies below the ground deformation. The idea behind these changes is that the distribution of seismic moment will show where the slip that caused the deformation occurred and therefore trace out the faults that slipped during the earthquake.

5.6 Applying the New Algorithm to ALOS-2 Data

The InSAR interferogram that we fit was processed by [46] and was downloaded from the Nepal Earthquake ALOS-2 InSAR website [9]. The particular one used is the combination of the ALOS2040533050-150222 and ALOS2050883050-150503 products, yielding

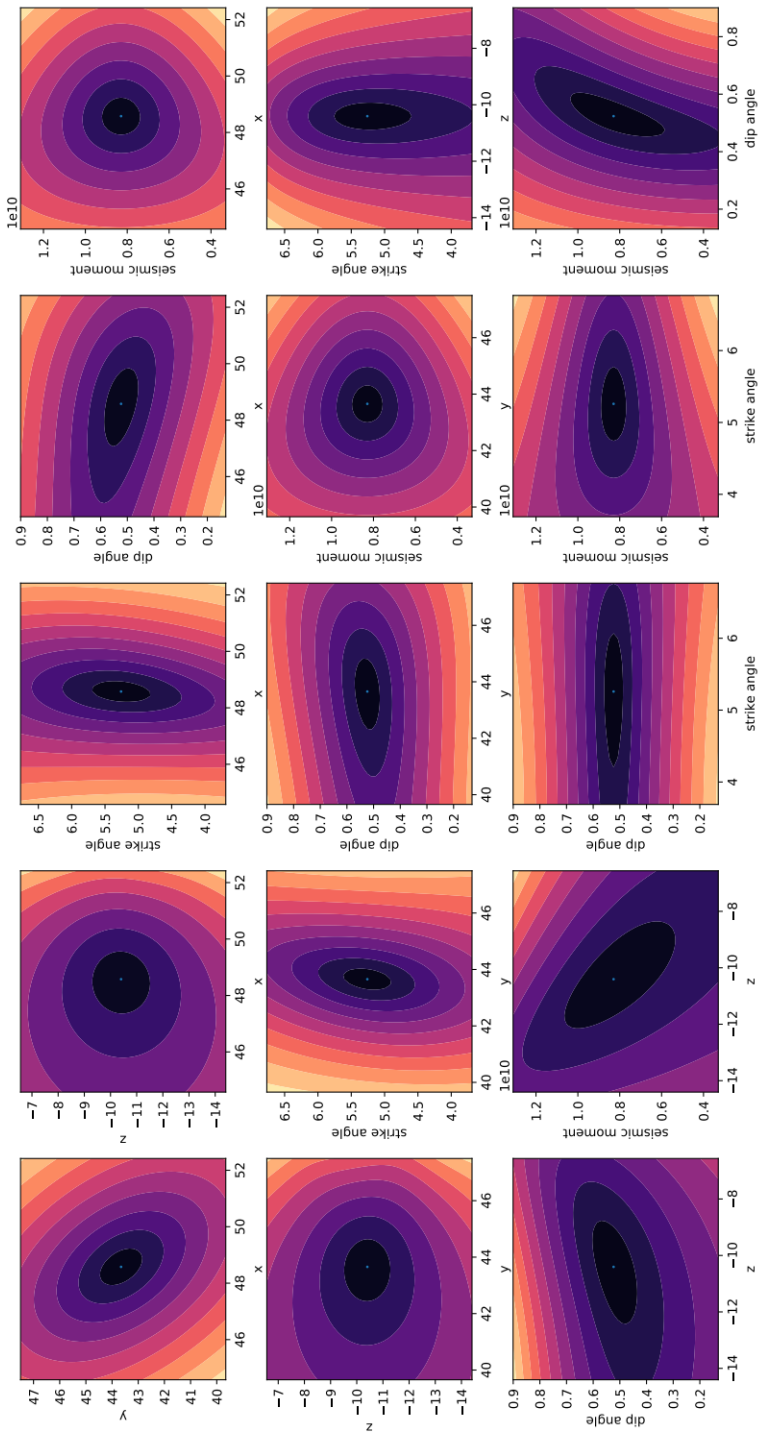

Figure 5.6. 2D heatmaps resulting from comparison of a single-source model to the single-source interferogram for every possible pairing of parameters. For each diagram, the listed parameters are varied from their true values (indicated by the blue dot at the center of each) and the error of the resulting model is calculated according to Equation 5.1. Black represents low error, while the progression toward white represents increasing error. The figure is rotated 90°counterclockwise to allow it to fit on the page.

an interferogram containing ground displacement between February 22nd, 2015 and May 3rd, 2015. This interferogram is different than the one we fit before—it includes only the deformation caused by the magnitude 7.8 earthquake that occurred on April 25th, 2015, 36 km east of Khudi, Nepal. We removed the additional aftershock from the deformation because it occurred on a different fault with a different orientation and we are now keeping the parameters fixed to those of the mainshock. With the parameters fixed to the mainshock, the model could not appropriately represent the aftershock. Otherwise, we follow the same data preparation steps outlined in Section 5.3: we bin the data, set limits on its extent, and convert it to vertical displacement.

When fitting this interferogram, we use the same genetic algorithm outlined in Section 5.1. The genetic algorithm was set to use a population size of 2000, with each solution in the population containing 513 seismic point sources arranged in a single-layer 27 x 19 grid. The grid size is chosen such that point sources are placed in a square grid with ∼5km side length below the significant ground deformation in the interferogram. Since the earthquake was a result of thrust faulting [47], Okada's equations for dip-slip faulting were used to calculate the ground deformation caused by each point source. For this run of the algorithm only the seismic moment of each point source was allowed to vary to reduce the computational complexity—each point source kept its location and orientation fixed during fitting. The strike angle, dip angle, and depth of the point sources were chosen to be averages of the 5 sets of earthquake parameters reported in [48] for the 2015 earthquake, held fixed at the values of 288.2°, 6.06°, and 18.8km, respectively. The initial values of the point source seismic moments in the starting population are chosen from a uniform distribution in the range $10^6 < M < 10^8$ Nm. The chance for a model to be chosen to mutate in a given generation was 20%. If chosen to mutate, each point source in the model had a 10% chance to have its seismic moment shifted up or down. After running until 500 successive generations passed with no improvement to the error between the best model and the data, the algorithm returned the model visible in Figure 5.7. The model is fully defined by its 513 values for each point source's seismic moment in Figure 5.8. The residuals between the model and data can be seen in Figure 5.9.

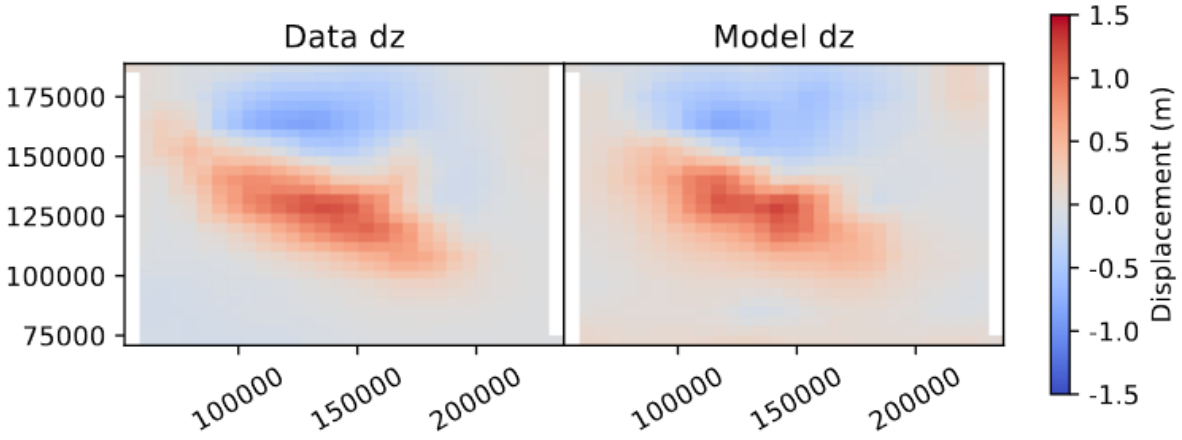

Figure 5.7. The z component of the ground deformation for the data (left) and model (right). The axes are in the Universal Transverse Mercator (UTM) coordinate system.

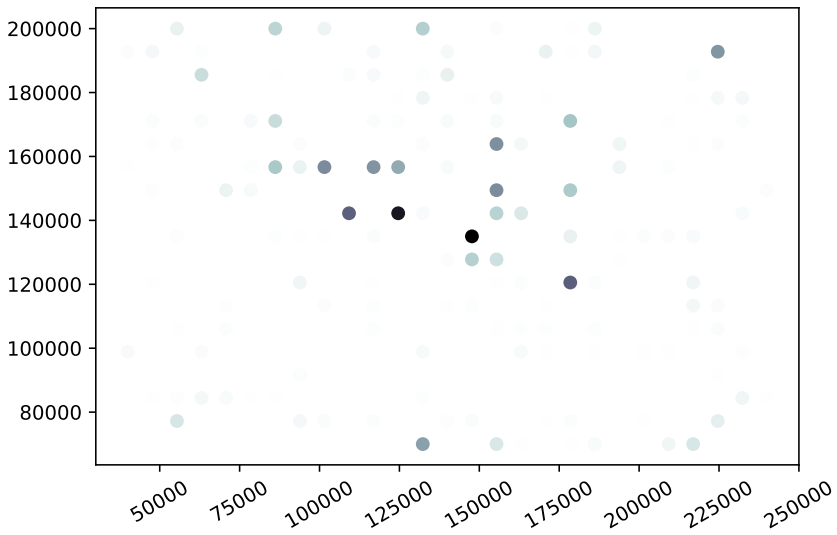

Figure 5.8. The point sources of the final genetic algorithm fit model shown in Figure 5.7. Each dot represents a point source and its color indicates the seismic moment of the source. Darker colors indicate higher seismic moment with the color moving toward white as seismic moment decreases. The axes are in the UTM coordinate system.

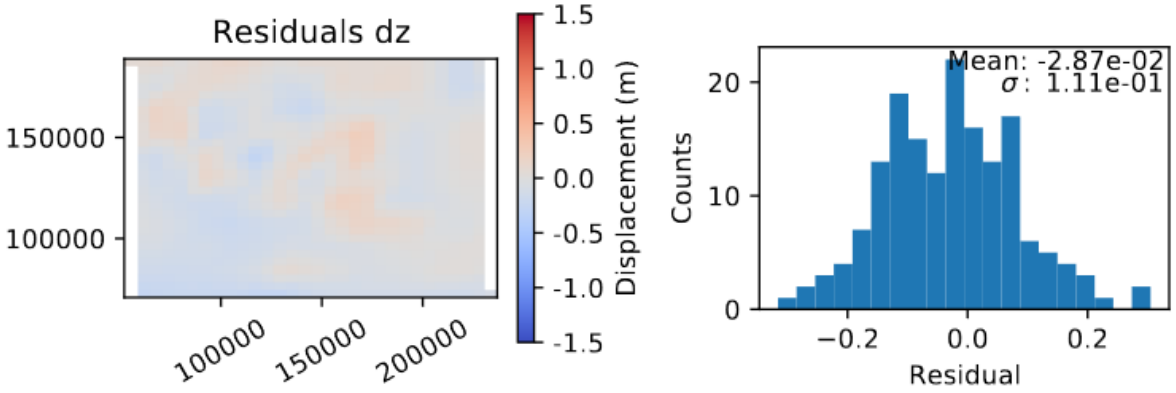

Figure 5.9. The residuals between the data and model shown in Figure 5.7 (left) and a histogram of the residuals (right).

5.7 Discussion and Conclusion

When comparing simulated or actual data to the resulting model, you can see that the basic shape of the data has been captured, but discrepancies exist if individual data points are compared. This is most likely a problem with the spread used when crossing and mutating the fit models. Since the spread of the parameters never changes, there comes a point where the error plateaus—further increases in fit accuracy require a decrease in the spread of the mutated parameters. A larger initial spread is useful to widely search the parameter space for the appropriate fit and to prevent falling into a local minimum. However, a large spread also prevents the fit from settling to a more exact solution. Simply reducing the spread leads to an increase in the computation time, as more time will be required for the solutions to search the parameter space in smaller steps. Increasing the population size can help widen the initial search area, but this also increases the computation time. A possible fix for this problem is an adaptive algorithm that modifies the spread during calculation to more efficiently search the parameter space and reduce the spread when close to the optimum solution. One such algorithm is outlined in [49].

The advantage of the method outlined in this chapter lies in its ability to invert the parameters of many seismic sources at a time. Inversions of fault geometry are typically calculated for a single rectangular fault plane, which limits their effectiveness in scenarios that are not well modeled by a single fault plane. One example is an interferogram that

contains deformation from more than one significant seismic event, such as the one fit in Section 5.3, which contains deformation from both a magnitude 7.8 mainshock and a magnitude 7.3 aftershock. Another capability of point sources is modeling of faults that cannot be accurately portrayed by planar surfaces. The point sources move independently, so in theory they can model any possible fault shape if an appropriate number of sources are used. The cost of this increased flexibility is an increase in the amount of computational complexity. The deformation caused by each source in a model must be calculated at every desired data point and their individual contributions must be summed to produce the total deformation field. This deformation field must be calculated for every model in the population for every generation that the algorithm runs. For example, if you desire for a population of 500 models containing 15 sources each to run for 10,000 generations, that is 75,000,000 function evaluations for each data point you are fitting. To reduce this computational complexity, it is possible to set a fixed value for any of the parameters or to use a more informative prior than a uniform distribution–both of which would reduce the size of the parameter space and therefore increase the speed of the fit. This was not done in this section to showcase the ability of the algorithm to fully explore the search space and arrive at a solution even with a vague starting point.

Future work with the genetic algorithm could include a first-pass fit to get general parameter values using a wide spread for a large search area, which could then be fed back into the algorithm with smaller spread values to fine-tune the parameters to provide the most accurate fit possible. Another possibility is to perform several fits using a different number of point sources in each model, to shed light on how it affects the overall fit. This would also help to combat overfitting by allowing adjustment of the total number of parameters compared to the total number of data points. The likely greatest improvement to the algorithm would be the inclusion of data from multiple sources; for example, the joint inversion of GPS and InSAR data or a combination of ascending and descending InSAR images that provide both horizontal and vertical displacements. This would reduce the overall freedom of the solution and provide more reliable results. Again, this chapter is meant more as a proof-of-concept for the method and the algorithm will

be expanded in the following iterations to include the above-mentioned improvements.

Chapter 6

Multiple Linear Regression Model

One of the main problems of the genetic algorithm is that it is slow to reach a solution. The main reason for this is because it relies on random-but-informed steps through the parameter space to move toward the final solution. However, we can instead utilize a multiple linear regression to estimate our parameters due to the simplifications outlined in Section 5.6—such as reducing the number of parameters and fitting only a single earthquake.

6.1 A Simpler But Faster Model

Since we are now only fitting for the seismic moment of each point source, the inversion problem becomes linear. This is because Equations 3.1-3.6 are linear in the seismic moment of the point source (after replacing $U_i \Delta\Sigma$ in each equation with $\frac{M_i}{\mu}$). Therefore, we can set up the equations to calculate the displacement of the model as a matrix equation as shown in Equation 6.1. Here y_i is the ground displacement of the model at point i, G_{ij} is the Green's function value for the displacement at point i due to source j, and M_j is the seismic moment of source j. Because we hold the position, strike, dip, and rake angles of the sources constant, the Green's matrix values G_{ij} are constant for a given model. The ground displacement y_i of point i is then given by $\sum_j G_{ij} M_j$. We are now left with a matrix inversion problem, which can be solved much more quickly than the nonlinear system of equations we dealt with before.

$$\begin{bmatrix} y_1 \\ y_2 \\ \vdots \\ y_i \end{bmatrix} = \begin{bmatrix} G_{11} & G_{12} & \dots & G_{1j} \\ G_{21} & G_{22} & \dots & G_{2j} \\ \vdots & \vdots & \ddots & \vdots \\ G_{i1} & G_{i2} & \dots & G_{ij} \end{bmatrix} \begin{bmatrix} M_1 \\ M_2 \\ \vdots \\ M_j \end{bmatrix} \tag{6.1}$$

6.2 Applying the Multiple Linear Regression Inversion Model to ALOS-2 Data

For this inversion we use the data as prepared in Section 5.6 with one change: the data are instead binned into a 75x75 histogram during processing. To summarize, it contains only the deformation of the M_w 7.8 mainshock, is downsampled and limited to a specified area around the earthquake. The model also remains the same: it is composed of a 27x19 grid of point sources, spans the area below the ground deformation data, and only the seismic moment of each source is allowed to vary. A comparison between the data and model obtained from the inversion is shown in Figure 6.1. The residuals between the data and model, as well as a histogram of the residuals, can be seen in Figure 6.2. Finally, the distribution of point sources in the model are plotted in Figure 6.3.

6.3 Discussion and Conclusions

On first glance, this inversion appears to have improved the overall fit compared to the previous genetic algorithm inversion in Figure 5.7, most notably at the "tails" that protrude from the area of positive displacement at the left and upper right sides. The tails are absent in the genetic algorithm fit, though they are less defined even in the data due to the coarser binning used for that inversion. However, upon closer inspection, the multiple linear regression model generally overestimates the amount of displacement. The overestimation can most easily be seen in Figure 6.2, in both the residual map and histogram of residuals. The mean of the residuals is -14.6cm, meaning that, on average, the model overestimates the amount of displacement by 14.6cm. Compared to the 2.8cm

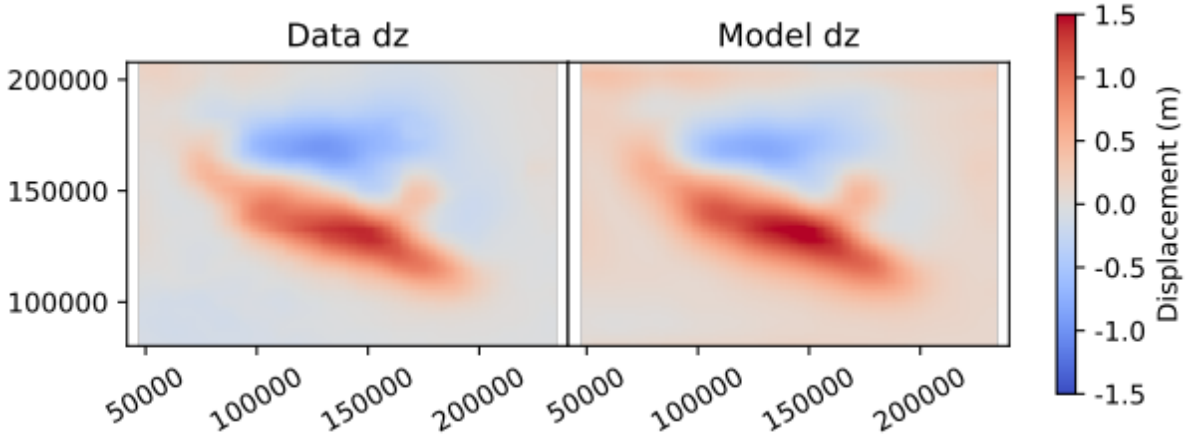

Figure 6.1. The z component of the ground deformation for the data (left) and model (right) for the multiple linear regression inversion model. The axes are in the UTM coordinate system.

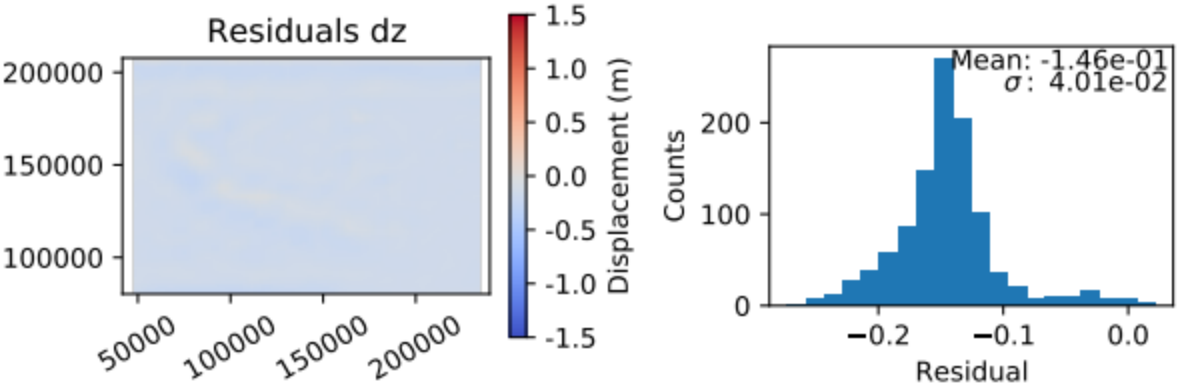

Figure 6.2. The residuals between the data and model shown in Figure 6.1 (left) and a histogram of the residuals (right).

average residual of the genetic algorithm inversion, the multiple linear regression inversion performs worse. The large shift in the mean indicates a bias in the inversion. The most likely source of the bias is due to one of the rules of multiple linear regression being violated—the independent variables shouldn't be correlated with one another. In this case, the sources are spatially correlated with their nearest neighbors since their deformation falls off over a distance of approximately 50 km and they are spaced approximately 5-7 km apart.

One improvement over the genetic algorithm inversion is in the standard deviation of the residuals. The distribution of residuals for the multiple linear regression inversion is

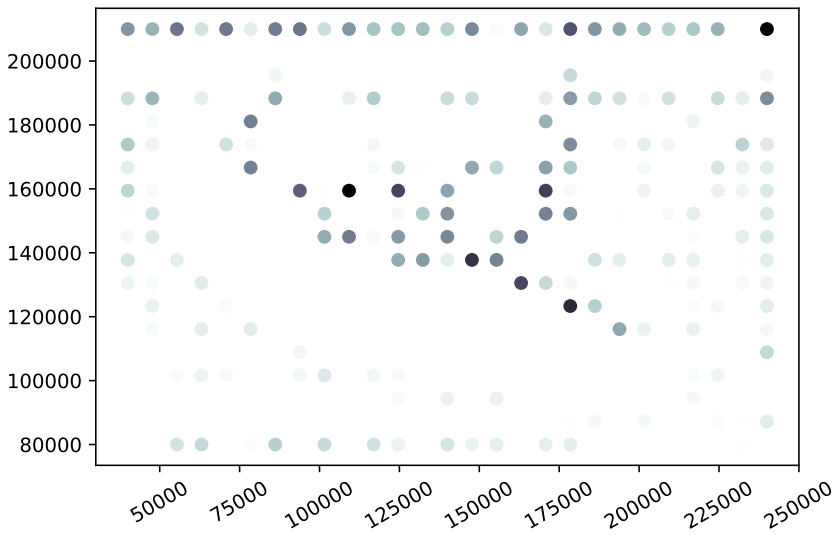

Figure 6.3. The point sources of the final multiple linear regression inversion model shown in Figure 6.1. Each dot represents a point source and its color indicates the seismic moment of the source. Darker colors indicate higher seismic moment with the color moving toward white as seismic moment decreases. The axes are in the UTM coordinate system.

much narrower with a standard deviation of 4 cm as opposed to the genetic algorithm inversion's standard deviation of 11 cm. So while the distribution is biased in one direction, it is much more compact, meaning that it is more consistent. The strongest positive aspect of this inversion is that it runs extremely fast compared to the genetic algorithm inversion. While the genetic algorithm inversion takes several hours on average, the multiple linear regression inversion runs in under a minute.

The ideal inversion would produce a mean residual near zero and minimize the standard deviation of the residuals, so neither of the inversions so far are ideal. The genetic algorithm is slow and has a significant spread in the residuals, while the multiple linear regression model is fast but produces a biased model. The next logical step forward is to use a non-linear solver that can account for the correlation between sources to see if it provides a model that is a happy medium between that of the genetic algorithm and multiple linear regression. We discuss this approach in the next chapter.

Chapter 7

LMFit

7.1 The LMFit Solver

While genetic algorithms are adept at searching wide parameter spaces, the time they take to solve a given problem can vary widely between runs. A compromise between population size, number of generations, and the parameter mutation spread must be found for a given problem because each one affects the amount of computation time necessary to reach an acceptable solution. Though the multiple linear regression inversion was an improvement in computation time, it suffered from a bias due to the correlation between neighboring point sources.

To alleviate these issues, we decided to use the Python package LMFit to solve for the model parameters instead. LMFit uses the Levenberg-Marquardt (LM) algorithm which is commonly used to solve non-linear least-squares problems so it is useful in a wide variety of problems. The LM algorithm utilizes gradient descent, so rather than relying on the stochastic nature of the genetic algorithm to slowly move toward the solution, the LM algorithm uses the gradients of the parameter space to move there more efficiently. We chose LMFit specifically because it is highly customizable and simple to use. A parameter object is defined for each target parameter, and LMFit allows us to set limits on each parameter if desired. One downside is that the LM algorithm requires an initial guess for each parameter to help it avoid falling into a local minimum. However, we have a solution to this problem: the focal mechanism is commonly calculated for any given earthquake,

which contains all of the necessary earthquake source parameters.

In order to utilize LMFit to solve an inversion problem, we must first define an objective function. The way in which we define your objective function can have a significant effect on the time required to solve the problem, so care must be taken when defining it. The return value of the objective function must be the residual between the target data and the model we define. To calculate the ground displacement of a given model (which is used to calculate the residual), we must first calculate the Green's matrix G_{ij} that defines how each point source in the model contributes to the total ground deformation. This requires us to calculate the value of Okada's equations for every combination of displacement point i and source j. However, as explained in Section 6.1, the Green's matrix G_{ij} is constant since we keep the position, strike, dip and rake angles of the sources fixed. Therefore, we can greatly speed up the residual calculations by using a pre-calculated Green's matrix. To get the ground displacement of a model, you simply multiply the Green's matrix by the vector of source seismic moments as shown in Equation 6.1.

7.2 Applying the LMFit Algorithm to ALOS-2 Data

For this inversion we use the same data as the multiple linear regression fit. To summarize, it contains only the deformation of the M_w 7.8 mainshock, it is downsampled, and it is limited to a specified area around the earthquake. The model also remains the same: it is composed of a 27x19 grid of point sources, spans the area below the ground deformation data, and only the seismic moment of each source is allowed to vary. A comparison between the data and model obtained from the inversion is shown in Figure 7.1. The residuals between the data and model, as well as a histogram of the residuals, can be seen in Figure 7.2. Finally, the distribution of point sources in the model are plotted in Figure 7.3.

7.3 Discussion and Conclusions

The LMFit inversion appears to successfully recreate the input deformation data. All of the main features are visible, including the tails that were missed by the genetic algorithm inversion. Looking at Figure 7.2, there is no evident bias of the inversion visible in either

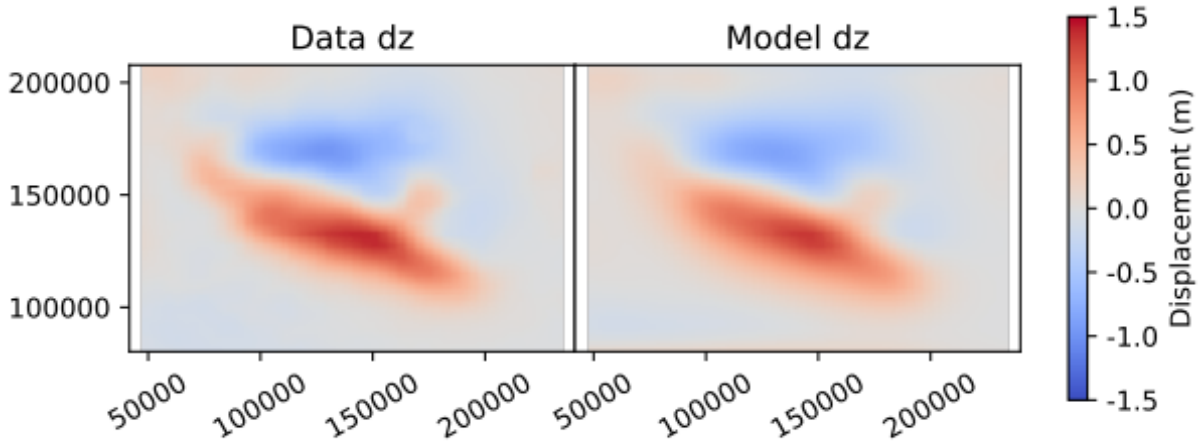

Figure 7.1. The z component of the ground deformation for the data (left) and model (right) for the LMFit model. The axes are in the UTM coordinate system.

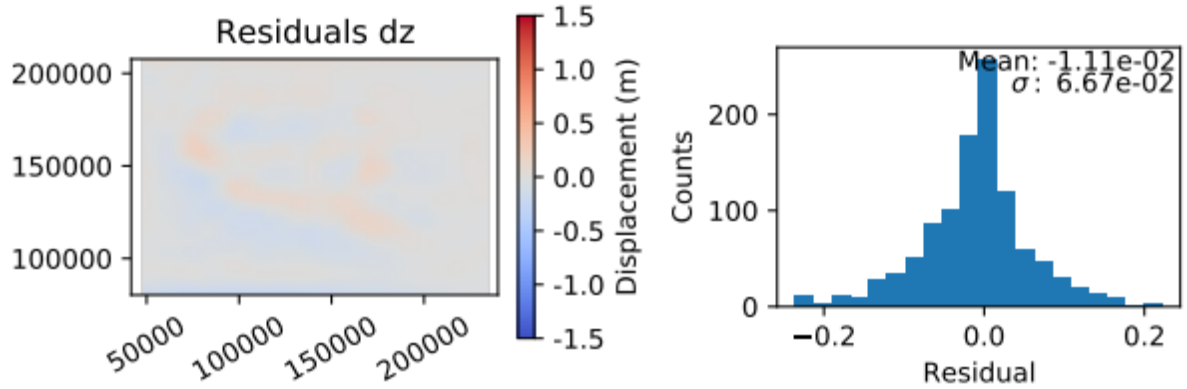

Figure 7.2. The residuals between the data and model shown in Figure 7.1 (left) and a histogram of the residuals (right).

plot. The histogram appears symmetric and its mean lies at 1.11 cm, meaning the average error for each data point is 1.11 cm. The standard deviation of the residuals is 6.67 cm.

If we look at the seismic moment distributions of each inversion in Figures 5.8, 6.3, and 7.3 we find that each one places the points of maximum seismic moment in similar areas. This area corresponds to the line of discontinuity between the positive and negative displacement lobes, which is expected based on Okada's deformation equations. If you look from Figure 5.8 to Figure 6.3 to Figure 7.3 in sequence, they appear to display the same general distribution with its features becoming more defined as you move through the sequence. Each distribution has sources of nonzero moment placed at the far edges

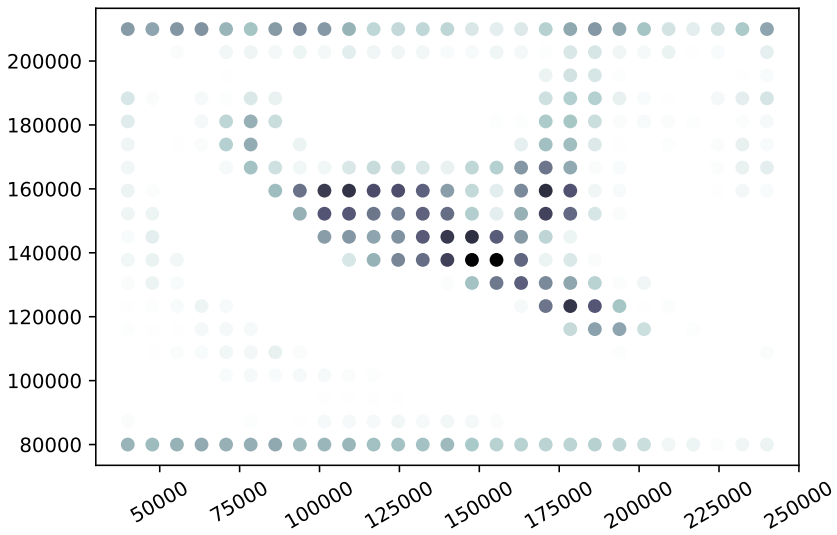

Figure 7.3. The point sources of the final LMFit inversion model shown in Figure 7.1. Each dot represents a point source and its color indicates the seismic moment of the source. Darker colors indicate higher seismic moment with the color moving toward white as seismic moment decreases. The axes are in the UTM coordinate system.

of the area (where displacement should be near zero) which we believe to be due to edge effects caused by the sources extended all the way to the edge of the data. Edge effects could be minimized by increasing the area around the deformation which we fit so the separation between edge effects and true signal is clear.

Since the fault involved in this event has a very small dip angle (about 9°), it is almost horizontal. Therefore, the seismic moment distribution can also be viewed as the slip distribution upon the fault. Slip distributions are commonly calculated as part of the investigation of a seismic event. Future work with our algorithm could include parameters aside from the seismic moment to see if it is possible to determine both the fault geometry and slip distribution simultaneously, rather than in two separate inversions as is typically done. If only the slip distribution is desired and the fault geometry is known, we could include the rake angle as an additional parameter to more accurately determine the slip distribution on the fault.

The means and standard deviations of the residuals for each inversion described in the

	Genetic Algorithm	Linear Regression	LMFit
Mean	-2.87cm	-14.6cm	-1.11cm
σ	11.1cm	4.01cm	6.67cm

Table 7.1. The means and standard deviations of the residuals for each inversion of the ALOS-2 data.

last few chapters are displayed in Table 7.1. The lowest mean was achieved by the LMFit inversion and the lowest standard deviation by the multiple linear regression fit. Despite its slightly higher standard deviation, the model obtained from the LMFit inversion has the best performance overall because it doesn't suffer from a visible bias while still keeping a lower standard deviation. However, this is not to say that the multiple linear regression inversion is useless—if the bias is always in a certain direction, it could be possible to account for it and minimize its effect while also benefiting from its high speed. The same cannot be said for the genetic algorithm inversion. Its main problem is that it produces a non-Gaussian distribution with a large standard deviation, meaning that it is the most inconsistent of the models. The most likely solutions to this problem are either to increase the number of data points to the same level as the other inversions or to reduce the spread of the mutation operator. Unfortunately, both of these changes will increase the time required to perform the inversion, which is already the slowest of the inversion methods. Because of this, the genetic algorithm inversion will be dropped in favor of the LMFit inversion, since it outperformed the genetic algorithm in both mean and standard deviation of residuals, as well as in time required to run. Since the multiple linear regression and LMFit inversions each have their upsides, we will apply both in the case study to follow in the next chapter.

Chapter 8

The Ridgecrest Earthquake Sequence: A Case Study

To test the performance of both the multiple linear regression and LMFit inversions, we apply them to a common event: the M_w 7.1 mainshock of the Ridgecrest earthquake sequence in 2019. We chose the Ridgecrest mainshock because it has been extensively studied since it is the largest earthquake to occur in California since the M_w 7.1 Hector Mine earthquake in 1999. The mainshock had a large mean slip of 1.2-1.7m [50], giving it a very clear InSAR signal for our inversions.

8.1 The Ridgecrest Earthquake Sequence

The Ridgecrest earthquake sequence began on July 4th, 2019 when a M_w 6.4 foreshock occurred southwest of Searles Valley, California. It was followed by the occurrence of the M_w 7.1 mainshock on July 5th, 2019. The mainshock has since been characterized as right-lateral slip on a series of northwest-southeast trending faults [51]. An image of the fault traces is shown in Figure 8.1. A timeline of the aftershocks that occurred as a part of the Ridgecrest earthquake sequence can be seen in Figure 8.2, while the locations of the aftershocks are mapped in Figure 8.3. Both figures cover a 21 day time period after the M_w 6.4 foreshock and contain aftershocks with a M_w greater than 2.5.

Figure 8.1. The fault traces produced by the M_w 7.1 Ridgecrest mainshock [7].

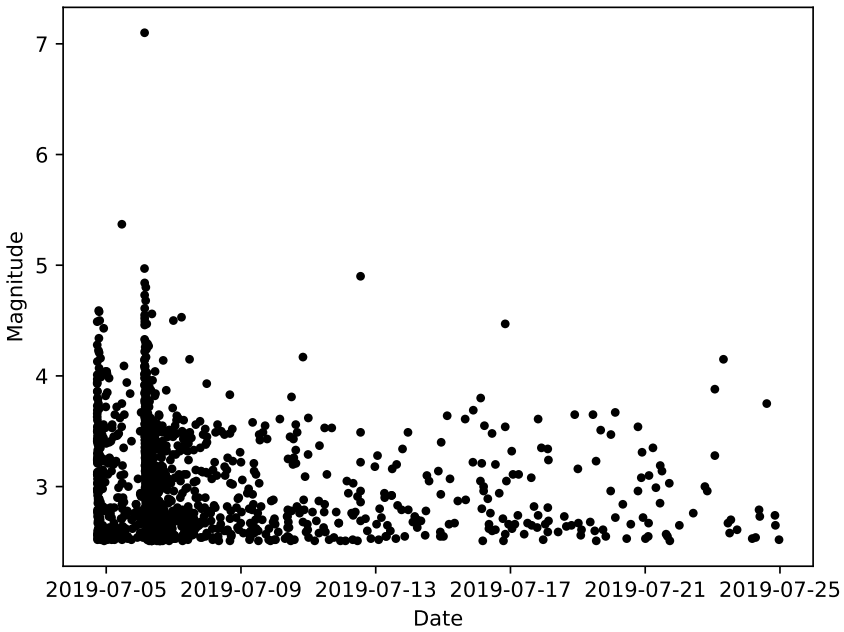

Figure 8.2. Aftershocks ($M_w < 2.5$) occurring within a 21 day period after the M_w 6.4 foreshock. The earthquakes are plotted according to their UTC time.

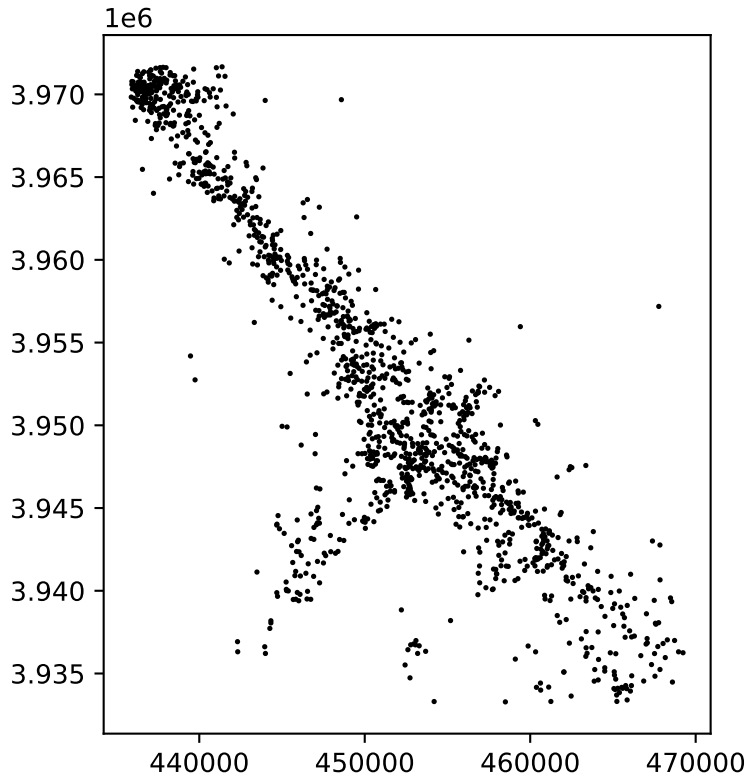

Figure 8.3. A map displaying the locations of the aftershocks ($M_w < 2.5$) occurring within a 21 day period after the M_w 6.4 foreshock. The axes are in the UTM coordinate system.

8.2 Data Preparation

Before we can begin our analysis we need to convert the data into a usable format. We start from the group of interferograms shown in Figure 8.4 which were obtained from [52]. Both sides of Figure 8.4 are the combination of 7 separate interferograms that each cover a portion of the deformation caused by the earthquake sequence—the left is the east-west displacement and the right is the north-south displacement. The interferograms show a clear trace of the faults (the discontinuity between positive and negative displacements) but also suffer from a significant amount of speckle. Speckle is a fluctuation in the signal due to inconsistent measurement of the scatterers in a given pixel which can be seen most clearly on the middle-right portion of each image. Unfortunately, the speckle values vary

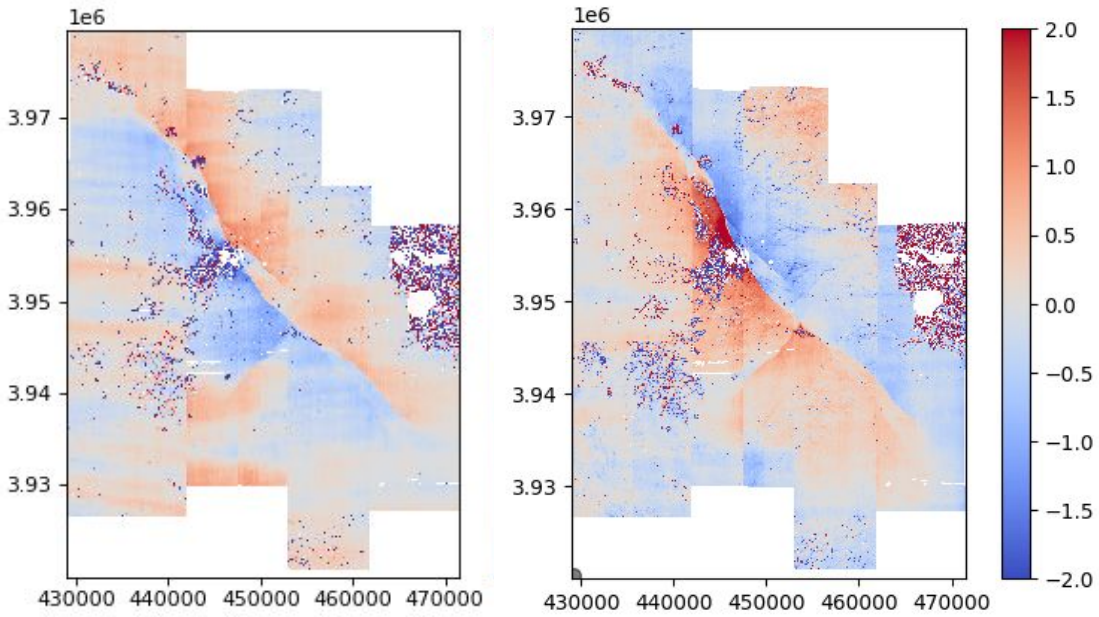

Figure 8.4. The east-west (left) and north-south (right) ground displacement caused by the Ridgecrest earthquake sequence. Positive deformation indicates movement to the east/north, while negative deformation indicates movement to the west/south. The axes are in UTM coordinates and the colorbar is in units of meters.

widely and are difficult to remove in an automated way.

To reduce the computational complexity of the inversions we make several simplifications. First, we focus on the deformation in a limited area around the northwest-southeast trending faults, which are attributed to the M_w 7.1 mainshock [7]. By limiting our analysis to the mainshock, the model only needs to represent right-lateral strike-slip faulting. Within this limited area the data is downsampled by kriging (interpolating) the value of the deformation from the interferograms at specified points. We also ignore points with a magnitude of displacement greater than 2 m (around the maximum measured displacement of the earthquake) to reduce the effect of the speckle in the interferograms (whose values go as high as 5 m). After downsampling, the data was reduced to 1192 data points in the specified area. The downsampled data in the east-west and north-south directions can be seen on the left side of Figures 8.5 and 8.8, respectively.

Our model for the inversions in this chapter is composed of a 20x20, uniformly-spaced grid of point sources (giving a total of 400) that spans the area below the ground defor-

Depth	8.0 km
Strike angle	322°
Dip angle	81°
Rake angle	-173°

Table 8.1. Parameters reported by USGS for the M_w 7.1 Ridgecrest mainshock [8].

mation data. The depth, strike, dip, and rake angles are held at fixed values obtained from the USGS event page for the M_w 7.1 Ridgecrest mainshock [8] and are outlined in Table 8.1. The initial value of the seismic moments are randomly chosen to be in the range 1.0e6 and 1.0e9 Nm.

8.3 Applying the Multiple Linear Regression Algorithm to Ridgecrest Data

The first inversion scheme we apply to the Ridgecrest interferograms is the multiple linear regression method that is outlined in Section 6.1. The general method is the same as outlined before, but it is instead applied to the Ridgecrest data using the model described in the previous section. In order, we apply the inversion to the east-west deformation (labeled dx in the figures), the north-south deformation (labeled dy in the figures), and then simultaneously to both components to see how the results are affected.

8.3.1 Using East-West Deformation Data

We first apply the multiple linear regression inversion to the east-west component of the Ridgecrest deformation data. The downsampled east-west deformation data and the resulting model are shown in Figure 8.5. The model clearly overestimates the east-west deformation across the entire dataset. If we look at Figure 8.6, it appears similar to the inversion in Section 6.2: the residuals are consistently negative and a bias is apparent due to the shifted mean. The mean residual is 50.6 cm—almost 1/3 of the average displacement—so this inversion is not reliable. The standard deviation of the residuals is 37.2 cm. Looking at the seismic moment distribution in Figure 8.7, no apparent structure is visible.

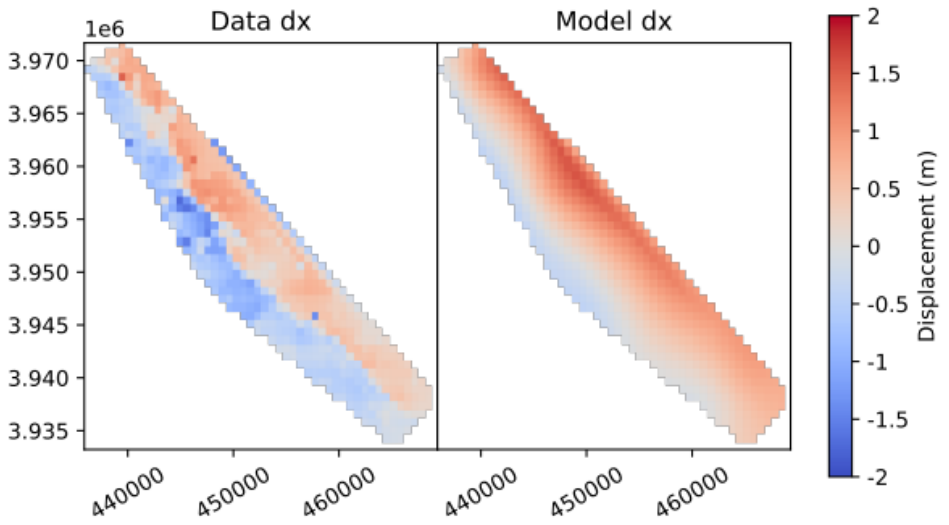

Figure 8.5. The x component of the ground deformation for the data (left) and model (right) for the multiple linear regression model. The axes are in the UTM coordinate system.

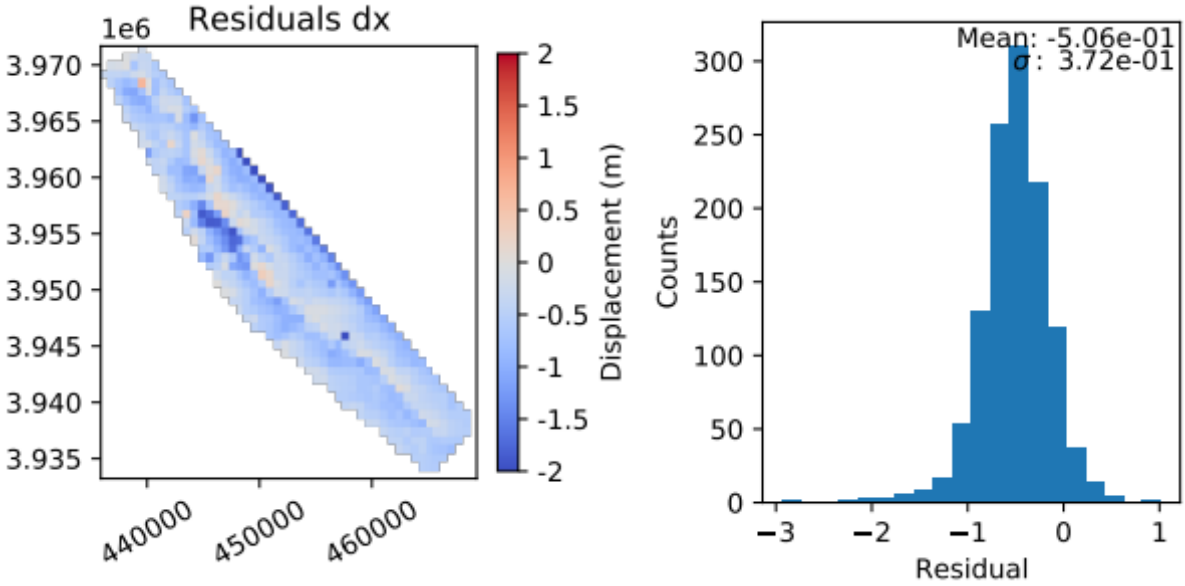

Figure 8.6. The residuals between the data and model shown in Figure 8.5 (left) and a histogram of the residuals (right).

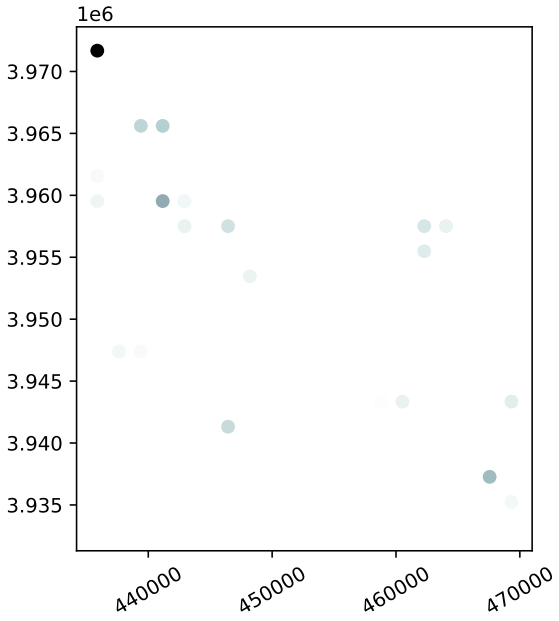

Figure 8.7. The point sources of the final multiple linear regression inversion model shown in Figure 8.5. Each dot represents a point source and its color indicates the seismic moment of the source. Darker colors indicate higher seismic moment with the color moving toward white as seismic moment decreases. The axes are in the UTM coordinate system.

8.3.2 Using North-South Deformation Data

Next we apply the multiple linear regression inversion to the north-south component of the Ridgecrest deformation data. The downsampled north-south deformation data and the resulting model are shown in Figure 8.8. This inversion appears more successful than the east-west inversion, since both the positive and negative lobes can be clearly seen and the separation between them follows a similar path. One major difference is that the transition from positive to negative displacement is very abrupt in the data, whereas in the model it is more gradual. Moving to the residuals in Figure 8.9, we see an area of significant error with both high positive and negative residuals. Referring back to the right side of Figure 8.4, in this area there is a very high positive displacement surrounded by a significant amount of speckle and some missing data. All of these contribute significantly to the discrepancy between the data and model. From the histogram of residuals we find a mean of 11.0 cm and standard deviation of 46.6 cm. While the mean is a significant improvement from the

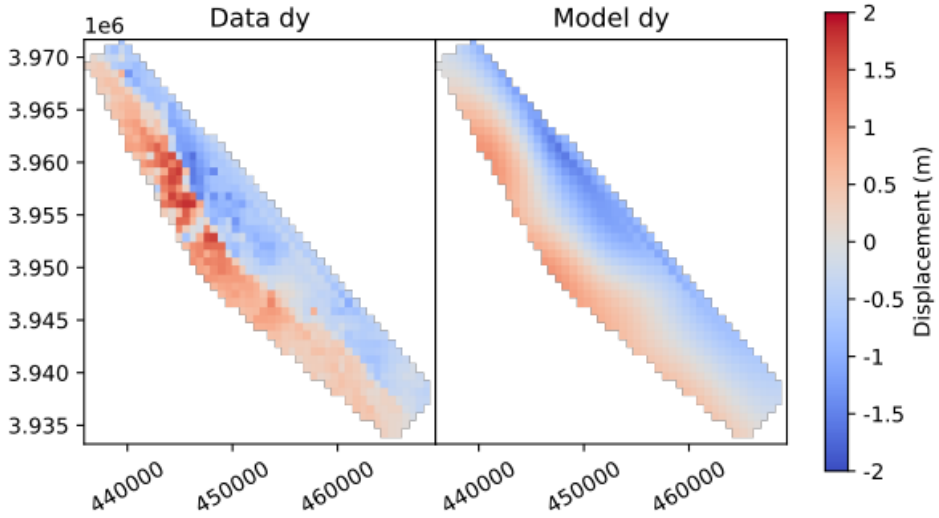

Figure 8.8. The y component of the ground deformation for the data (left) and model (right) for the multiple linear regression model. The axes are in the UTM coordinate system.

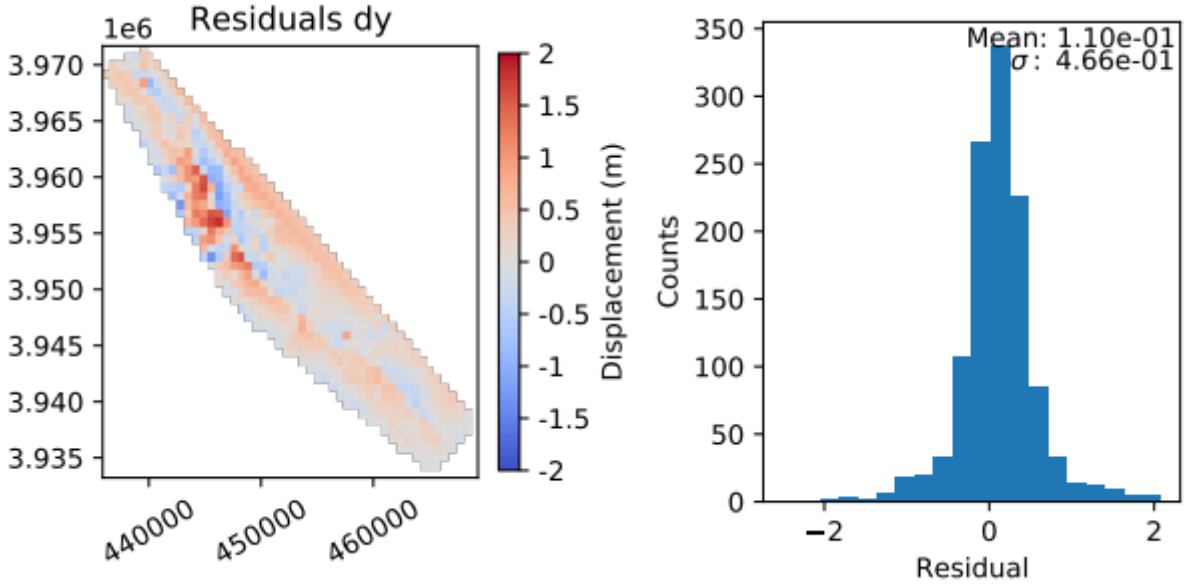

Figure 8.9. The residuals between the data and model shown in Figure 8.8 (left) and a histogram of the residuals (right).

east-west inversion, the standard deviation of the residuals has increased. If we compare the source distributions of each inversion, the north-south inversion appears to place more of the significant seismic moment along the trace of the fault and is less diffuse than the east-west inversion.

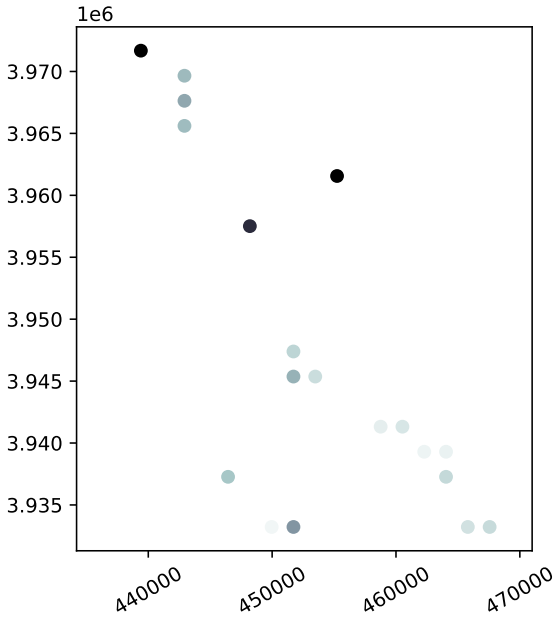

Figure 8.10. The point sources of the final multiple linear regression inversion model shown in Figure 8.8. Each dot represents a point source and its color indicates the seismic moment of the source. Darker colors indicate higher seismic moment with the color moving toward white as seismic moment decreases. The axes are in the UTM coordinate system.

8.3.3 Using Both East-West and North-South Data

Finally, we apply the multiple linear regression inversion to both the east-west and north-south deformation data simultaneously. In this inversion, we still develop a single model but it is compared to both datasets. This doubles the amount of data points used in the inversion, which correspondingly increases the amount of time the inversion takes. The goal of this is to improve the constraints on the model parameters to hopefully produce a more accurate model. The east-west deformation data and the corresponding model deformation are shown in Figure 8.11 and the north-south deformation and corresponding model deformation are shown in Figure 8.13. The residuals between the data and model for the east-west component and north-south component are shown in Figures 8.12 and 8.14, respectively. The east-west deformation of the model is greatly improved from that shown in Figure 8.5—it no longer suffers from a strong bias and captures the general shape of the deformation. The means and standard deviations of the residuals in each direction,

	Mean	σ
MLR - dx only	-50.6cm	37.2cm
MLR - dy only	11.0cm	46.6cm
MLR - both - dx	-7.16cm	41.0cm
MLR - both - dy	-4.81cm	49.5cm

Table 8.2. The means and standard deviations of the residuals for each multiple linear regression inversion of the Ridgecrest data.

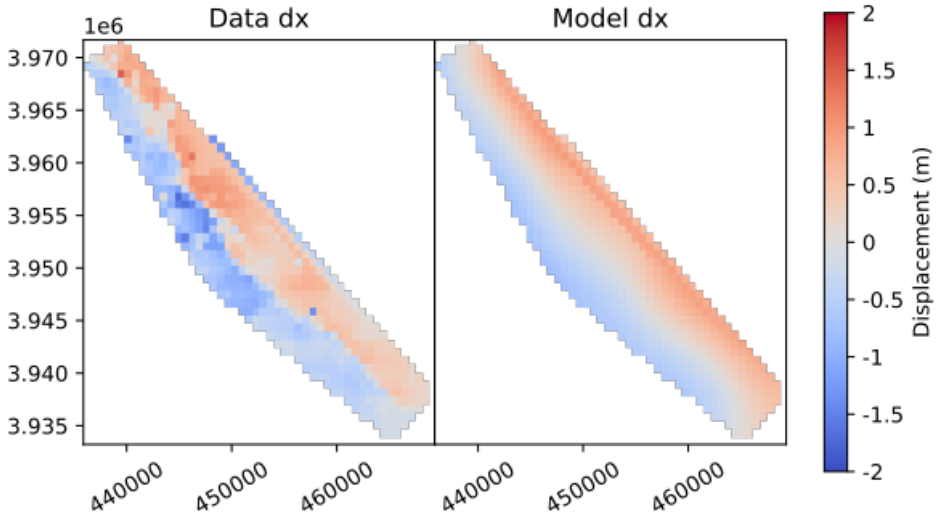

Figure 8.11. The x component of the ground deformation for the data (left) and model (right) for the multiple linear regression model utilizing both deformation components. The axes are in the UTM coordinate system.

as well as those of the previous inversions, are displayed in Table 8.2. The simultaneous inversion reduced the mean residuals in both directions—from -50.6 cm to -7.16 cm in the east-west direction and from 11.0 cm to -4.81 cm in the north-south direction. However, the standard deviation of the residuals in both directions increased slightly, to 41.0 cm in the east-west direction and to 49.5 cm in the north-south direction. One significant improvement over the single-dataset inversions can be seen in the source distribution in Figure 8.15. A much more defined trace of the fault line is visible, which is the expected location of most of the earthquake moment.

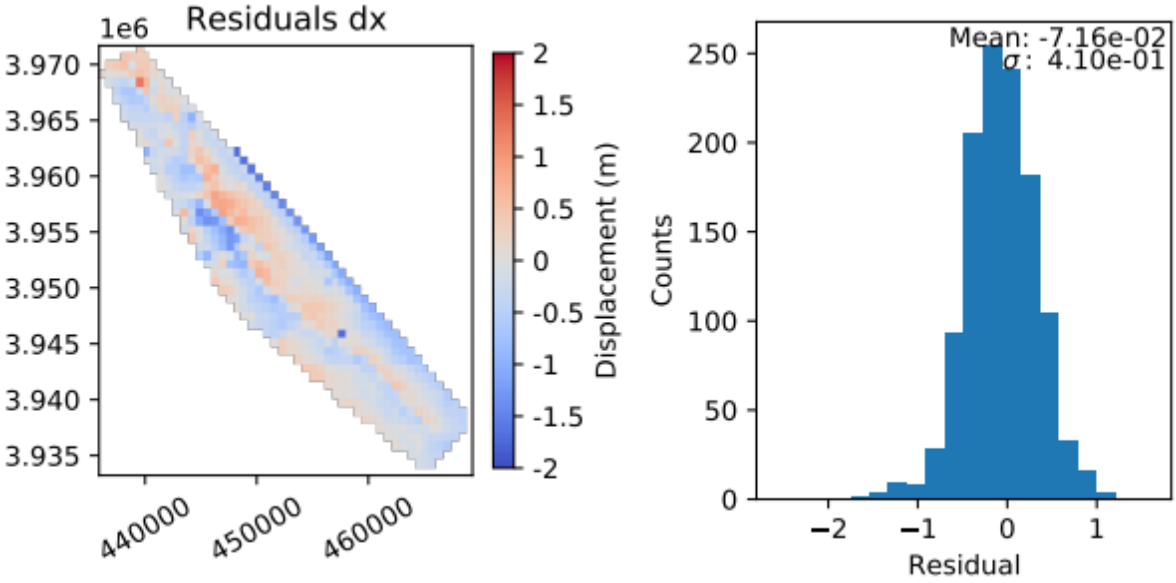

Figure 8.12. The residuals between the data and model utilizing both deformation components shown in Figure 8.11 (left) and a histogram of the residuals (right).

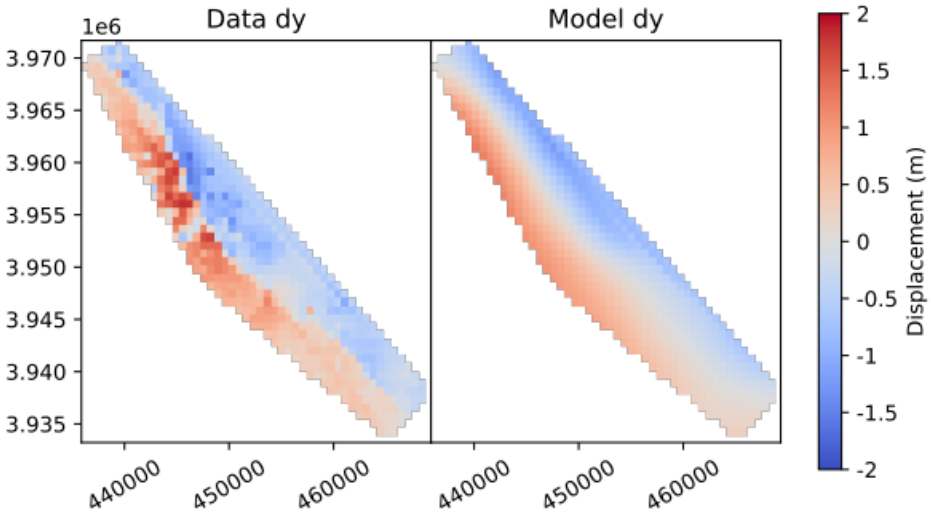

Figure 8.13. The y component of the ground deformation for the data (left) and model (right) for the multiple linear regression model utilizing both deformation components. The axes are in the UTM coordinate system.

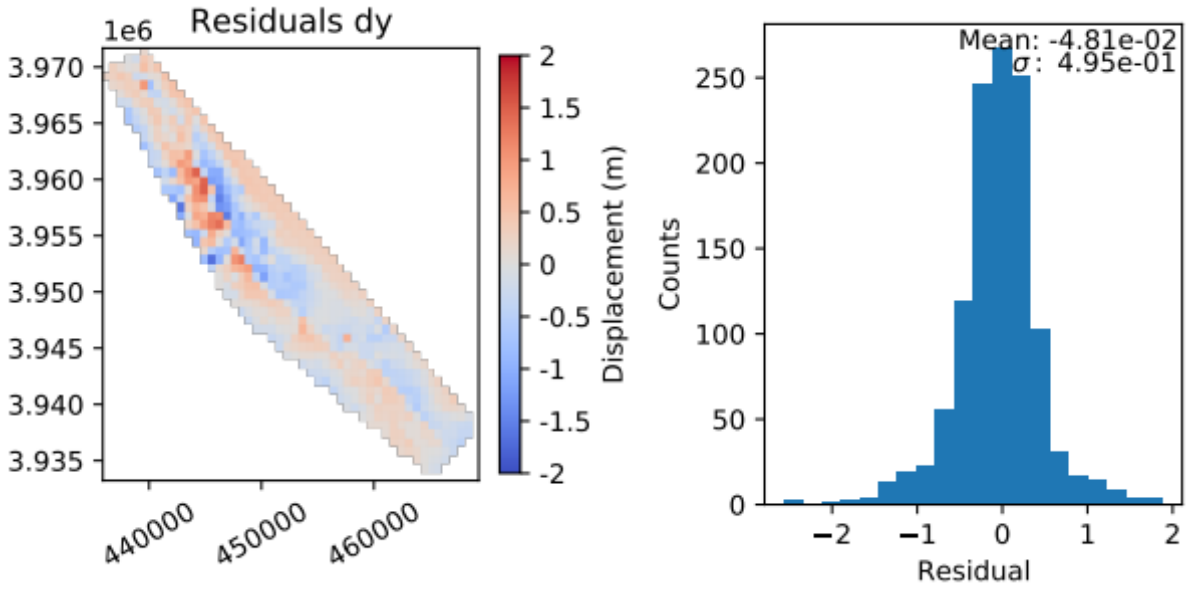

Figure 8.14. The residuals between the data and model utilizing both deformation components shown in Figure 8.13 (left) and a histogram of the residuals (right).

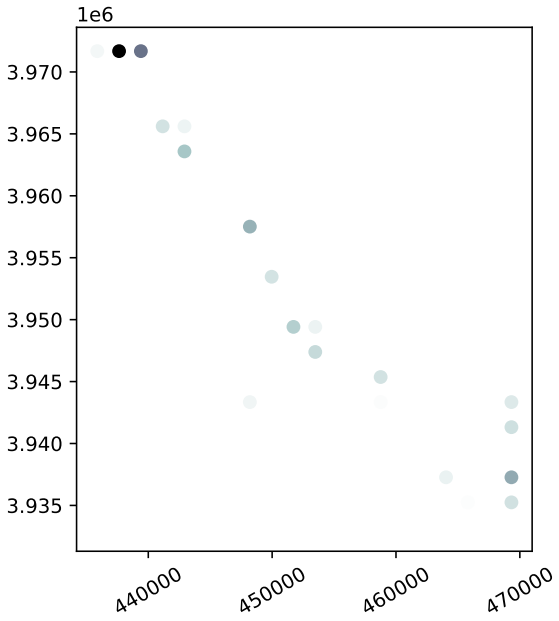

Figure 8.15. The point sources of the final multiple linear regression fit model utilizing both deformation components shown in Figures 8.11 and 8.13. Each dot represents a point source and its color indicates the seismic moment of the source. Darker colors indicate higher seismic moment with the color moving toward white as seismic moment decreases. The axes are in the UTM coordinate system.

8.4 Applying the LMFit Algorithm to Ridgecrest Data

The next inversion scheme we apply to the Ridgecrest interferograms is the LMFit inversion method that is outlined in Section 7.1. We follow the same method and use the model outlined at the beginning of this chapter. As before, we apply the inversion to the east-west deformation (labeled dx in the figures), the north-south deformation (labeled dy in the figures), and then simultaneously to both components to see how the results are affected.

8.4.1 Inverting for Seismic Moment

In the first set of inversions, we leave every parameter fixed except for seismic moment. Since LMFit is a nonlinear solver, we are not limited to linear inversions like we are with multiple linear regression. This makes the LMFit inversion much more flexible at the cost of increased computation time. If we find that the inversion could benefit from allowing more parameters to vary, we can redefine the objective function to do so.

8.4.1.1 Using East-West Deformation Data

We first apply the LMFit inversion to the east-west component of the Ridgecrest deformation data. The downsampled east-west deformation data and the resulting model are shown in Figure 8.16. The model captures the general shape of the deformation but the discontinuity between positive and negative displacement is blurred and follows a roughly straight line as opposed to the irregular shape of the true fault trace. No significant bias is apparent from the residuals in Figure 8.17 with a mean of -1.34 cm and standard deviation of 38.8 cm. The seismic moment distribution in Figure 8.18 overlaps the fault trace along its entire length but unexpectedly places the highest seismic moment at the top left corner. This could be caused by edge effects, which can be explored by running the same inversion with a dataset that covers a larger area. The distribution also has a few areas where the seismic moment extends away from the fault trace by as much as a few kilometers. An ideal distribution, for our purposes, would be compact and closely follow the path of the fault trace.

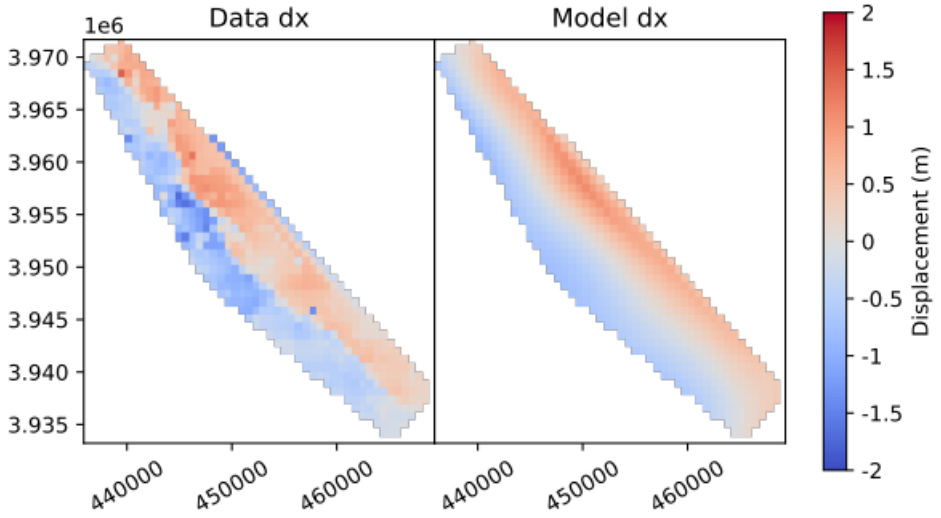

Figure 8.16. The x component of the ground deformation for the data (left) and model (right) for the LMFit inversion model. The axes are in the UTM coordinate system.

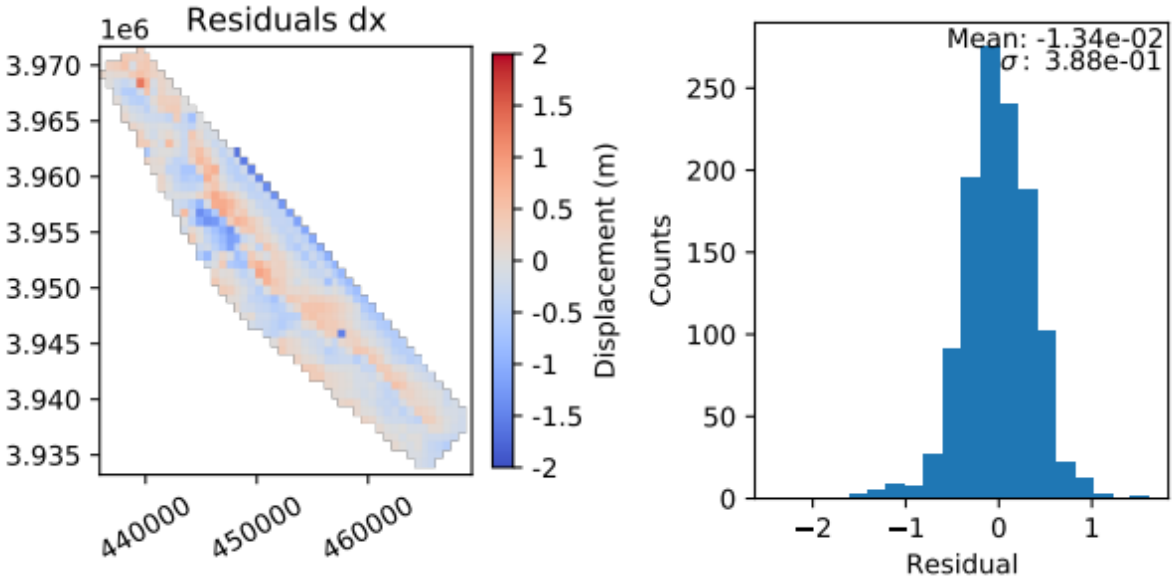

Figure 8.17. The residuals between the data and model shown in Figure 8.16 (left) and a histogram of the residuals (right).

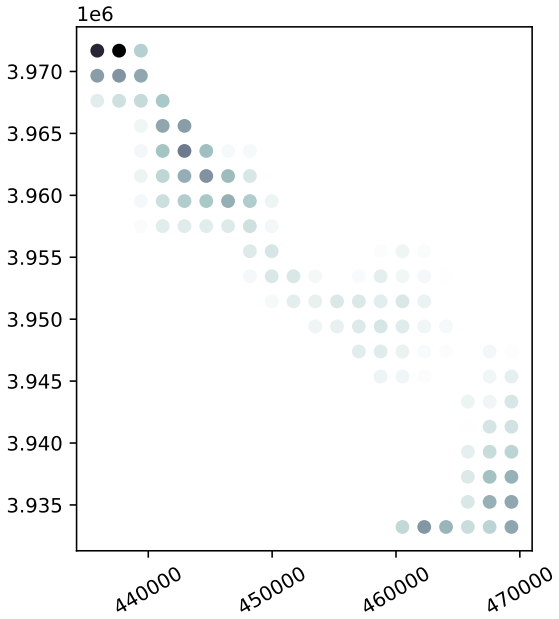

Figure 8.18. The point sources of the final LMFit inversion model shown in Figure 8.16. Each dot represents a point source and its color indicates the seismic moment of the source. Darker colors indicate higher seismic moment with the color moving toward white as seismic moment decreases. The axes are in the UTM coordinate system.

8.4.1.2 Using North-South Deformation Data

Next we apply the LMFit inversion to the north-south component of the Ridgecrest data. The data and corresponding model deformation are compared in Figure 8.19. This model better captures the shape of the fault trace though it still transitions from positive to negative displacement over a larger distance. The area of large positive displacement is also noticeably absent. Looking at the residuals we find a mean of 2.04 cm and standard deviation of 48.2 cm. Both values have increased compared to the east-west inversion. The source distribution also covers the fault trace but stretches farther away than that of the east-west inversion. Also of note is that the highest seismic moment is again placed at the top left of the distribution.

8.4.1.3 Using Both East-West and North-South Data

Finally, we apply the LMFit inversion to both the east-west and north-south deformation data simultaneously. The east-west deformation data and the corresponding model deformation are shown in Figure 8.22 and the north-south deformation and corresponding

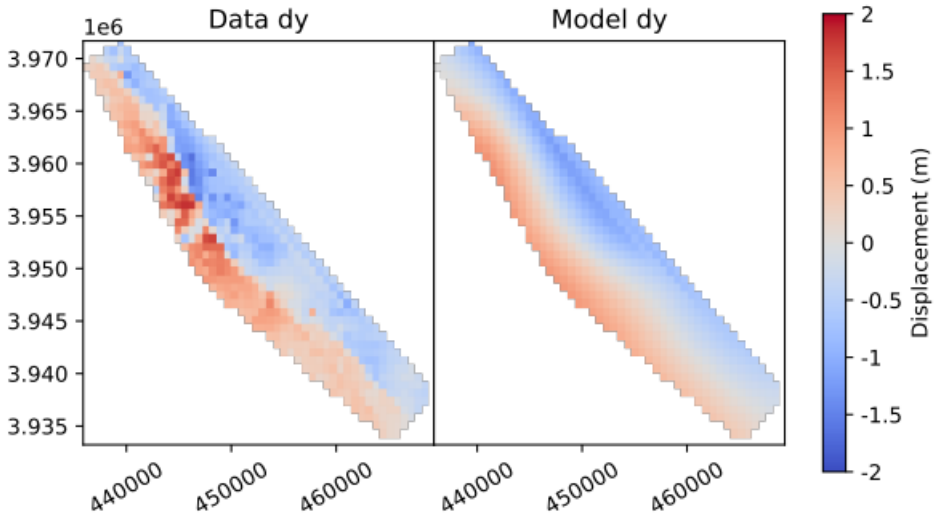

Figure 8.19. The y component of the ground deformation for the data (left) and model (right) for the LMFit inversion model. The axes are in the UTM coordinate system.

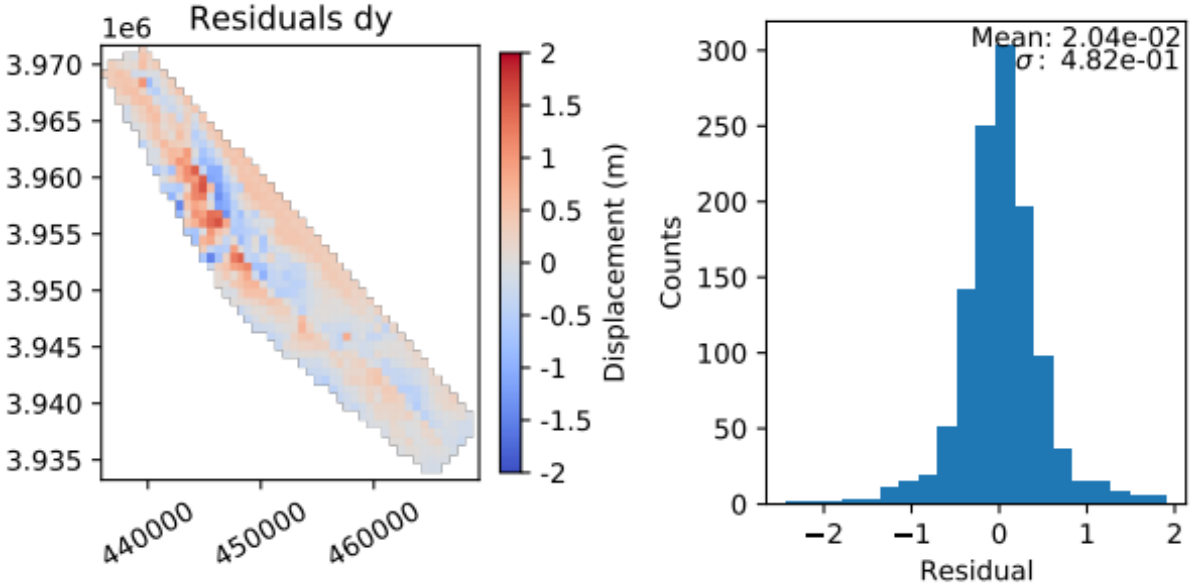

Figure 8.20. The residuals between the data and model shown in Figure 8.19 (left) and a histogram of the residuals (right).

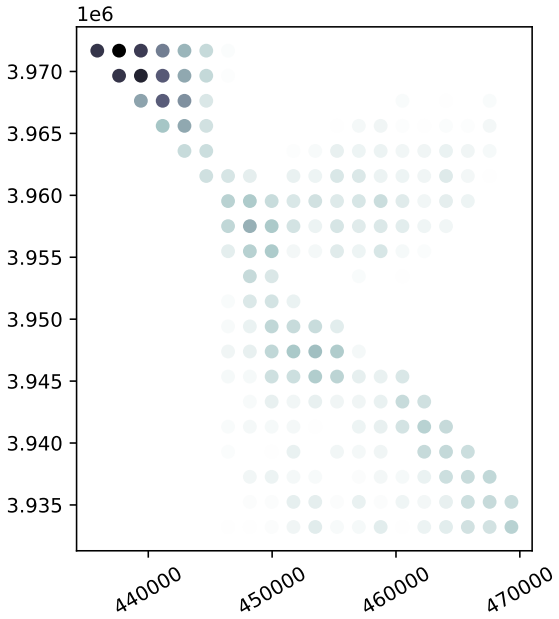

Figure 8.21. The point sources of the final LMFit inversion model shown in Figure 8.19. Each dot represents a point source and its color indicates the seismic moment of the source. Darker colors indicate higher seismic moment with the color moving toward white as seismic moment decreases. The axes are in the UTM coordinate system.

model deformation are shown in Figure 8.24. The residuals in the east-west and north-south directions can be seen in Figures 8.23 and 8.25, respectively. The mean and standard deviation for all of the LMFit inversions are listed in Table 8.3. In the east-west direction the mean residual increased from -1.34 cm to -3.85 cm, so it performs slightly worse while the mean residual in the north-south direction improved, decreasing from 2.04 cm to 0.057 cm. The standard deviation of the residuals increased slightly in both directions, similar to the multiple linear regression inversions. Looking at the source distribution in Figure 8.26 we see that it is much more compact than either of the single-direction inversions and still places the highest seismic moment at the top left corner.

8.4.2 Inverting for Seismic Moment and Strike Angle

One problem that arises frequently in our inversions for the seismic moment distribution of the Ridgecrest data is that it misses some of the details of the fault trace, most importantly, the meandering path. Some of the inversions ended on a fairly straight path for the fault, whereas the real fault trace is more complex. To more appropriately

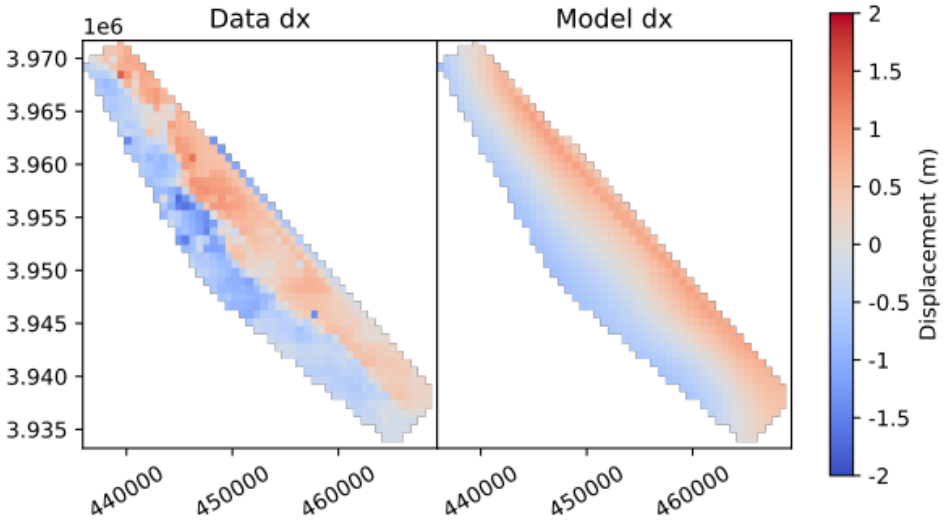

Figure 8.22. The x component of the ground deformation for the data (left) and model (right) for the LMFit inversion model utilizing both deformation components. The axes are in the UTM coordinate system.

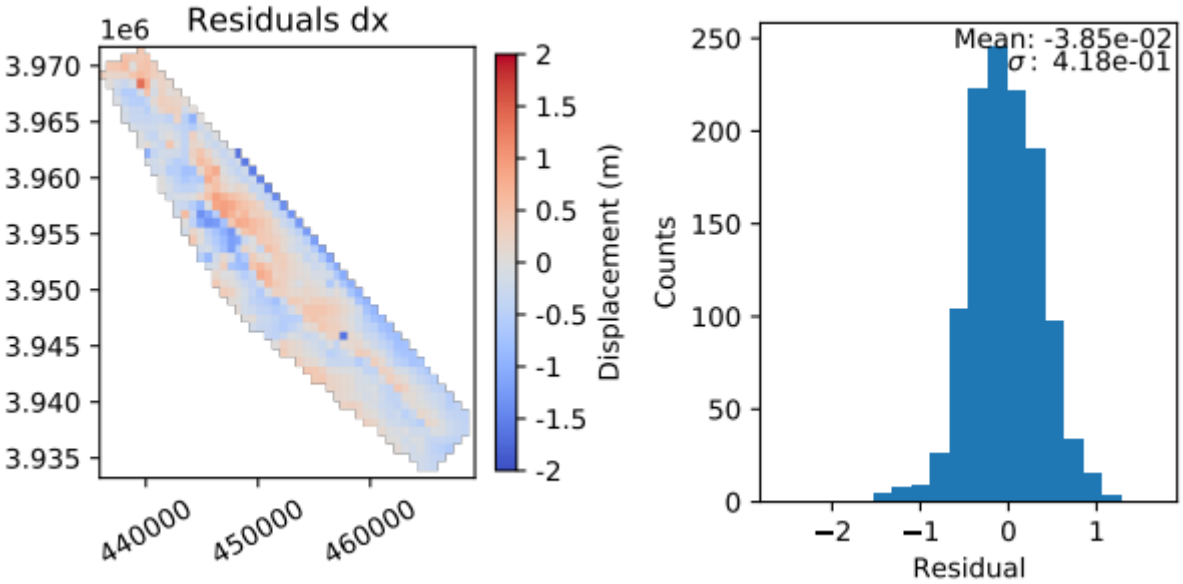

Figure 8.23. The residuals between the data and model utilizing both deformation components shown in Figure 8.22 (left) and a histogram of the residuals (right).

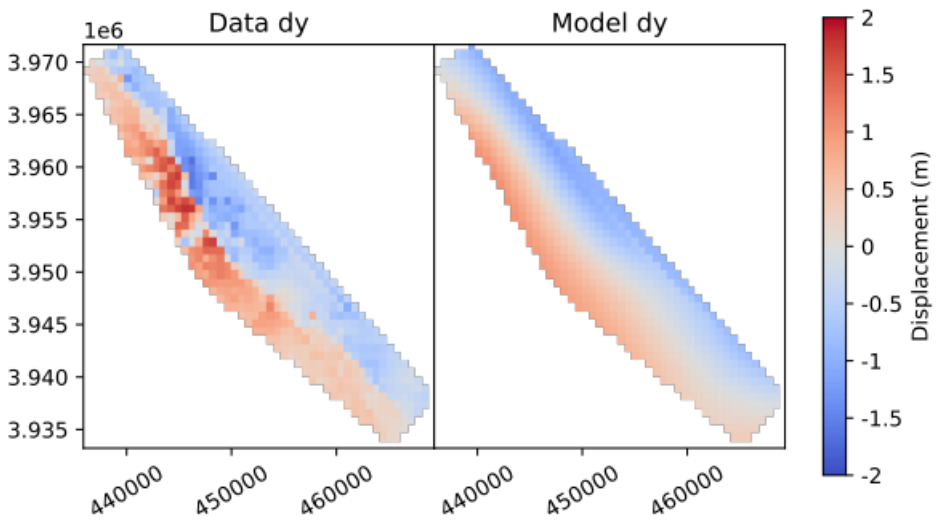

Figure 8.24. The y component of the ground deformation for the data (left) and model (right) for the LMFit inversion model utilizing both deformation components. The axes are in the UTM coordinate system.

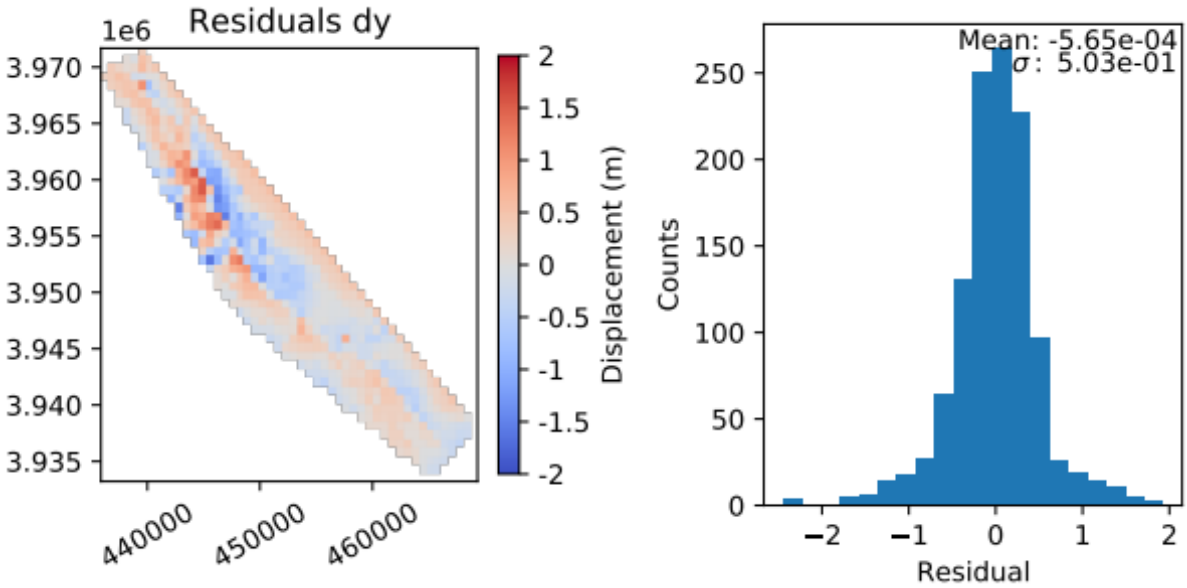

Figure 8.25. The residuals between the data and model utilizing both deformation components shown in Figure 8.24 (left) and a histogram of the residuals (right).

	Mean	σ
LM - dx only	-1.34cm	38.8cm
LM - dy only	2.04cm	48.2cm
LM - both - dx	-3.85cm	41.8cm
LM - both - dy	0.057cm	50.3cm

Table 8.3. The means and standard deviations of the residuals for each LMFit inversion of the Ridgecrest data.

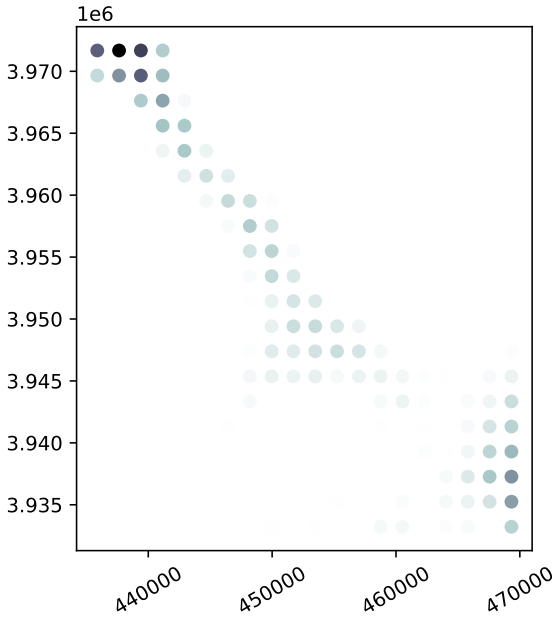

Figure 8.26. The point sources of the final LMFit inversion model utilizing both deformation components shown in Figures 8.22 and 8.24. Each dot represents a point source and its color indicates the seismic moment of the source. Darker colors indicate higher seismic moment with the color moving toward white as seismic moment decreases. The axes are in the UTM coordinate system.

capture these features, we expanded the inversion to include both seismic moment and strike angle. Adding strike angle as a parameter requires us to alter our definition of the objective function. We can no longer use the same Green's matrix for each source because the deformation equations non-linearly depend on strike angle. However, we can still simplify the deformation calculations. A single Green's matrix is calculated using a specified depth, dip angle, and rake angle. To get the deformation field for a source with a different strike angle or that is located at a different position, we perform a coordinate transformation and interpolate the new source deformation field from the precalculated field. After calculating the model deformation, the objective function finds the residual between the data and model for each pixel, and its goal is to minimize the residuals by adjusting the target parameters.

8.4.3 Inversion With No Limit On Strike Angle

Our first set of inversions for strike angle and seismic moment do not place any constraints on the parameters. We continue to use LMFit to perform the inversion with the same Ridgecrest datasets as before, using the objective function redefined to include strike angle as a parameter.

8.4.3.1 Using East-West Deformation Data

We first apply the LMFit strike inversion to the east-west component of the Ridgecrest deformation data. Figure 8.27 shows the downsampled east-west deformation data and the resulting model. The model is able to capture the turns in the fault trace and does so while reducing the width of the transition from positive to negative displacement. Figure 8.28 shows the residuals between the data and model. The mean of the residuals is -0.022 cm and the standard deviation is 32.0 cm, both the lowest values of any inversion performed so far. Both the seismic moments and strike angles of the model sources are shown in Figure 8.29. Seismic moments are plotted on the left and strike angle are plotted on the right. Each source on the left plot has a corresponding arrow that indicates its strike direction. The seismic moment distribution spans most of the area in question, so no clear fault trace is evident. There is also no apparent fault path that can be seen from the strike angles. The goal of including strike angle was that the inversion would reveal

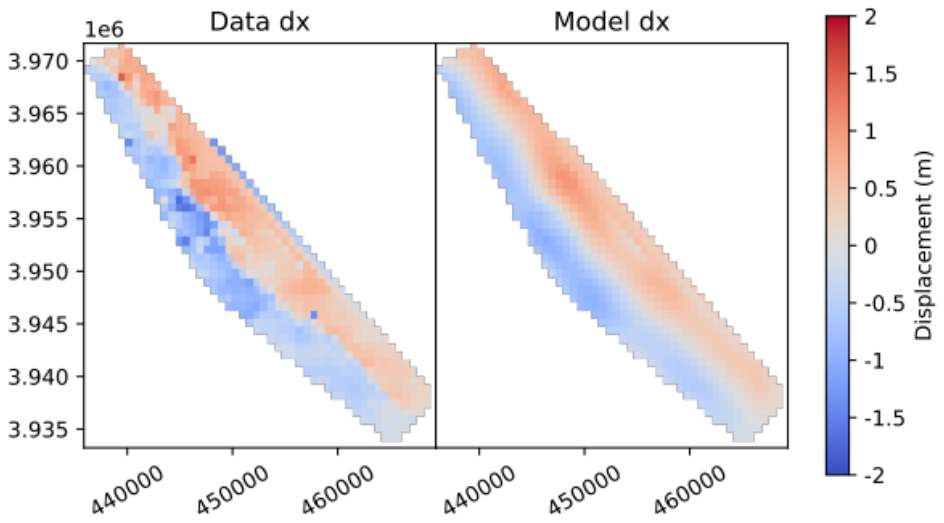

Figure 8.27. The x component of the ground deformation for the data (left) and model (right) for the LMFit inversion model. The axes are in the UTM coordinate system.

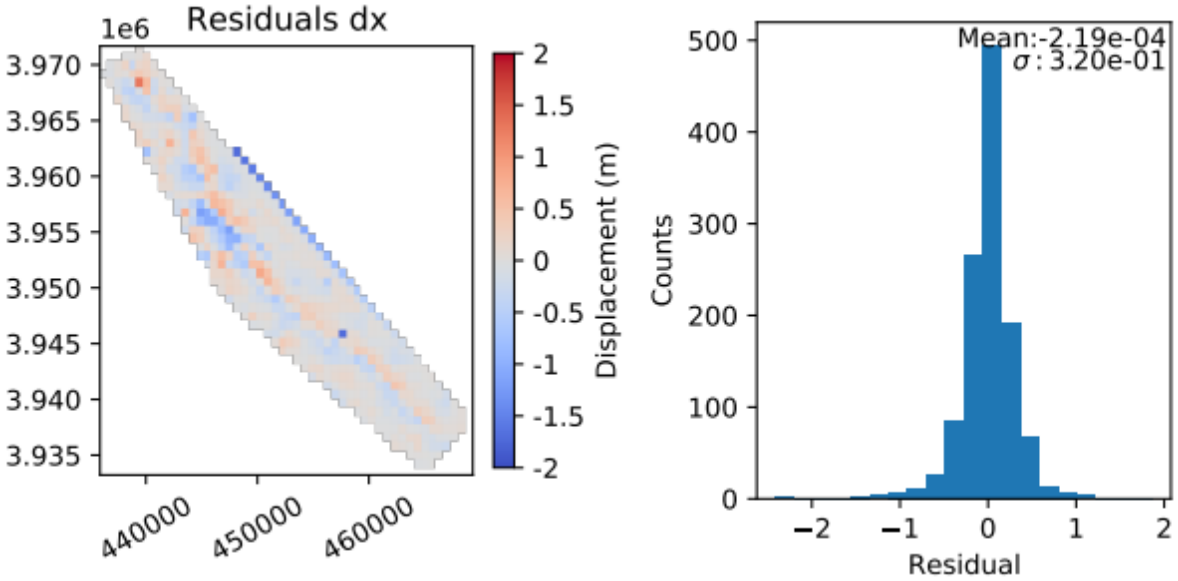

Figure 8.28. The residuals between the data and model shown in Figure 8.27 (left) and a histogram of the residuals (right).

a somewhat continuous path that represents the local strike of the fault as it turns.

8.4.3.2 Using North-South Deformation Data

Next we apply the LMFit strike inversion to the north-south component of the Ridgecrest data. The data and corresponding model deformation are compared in Figure 8.30. The residuals between the data and model are shown in Figure 8.31. This model also

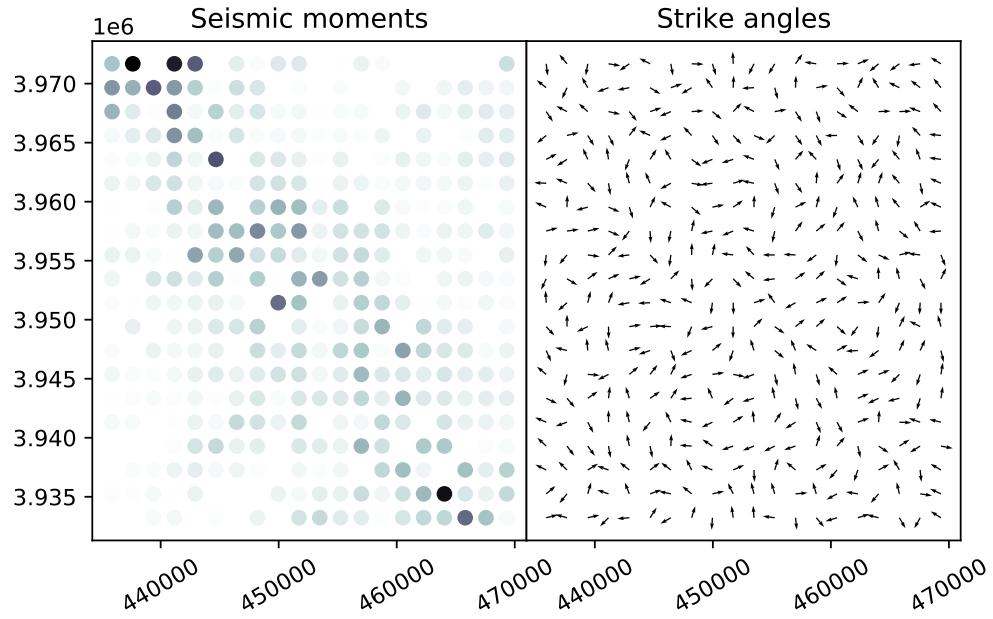

Figure 8.29. The point sources of the final LMFit inversion model shown in Figure 8.27. Each dot in the left half of the figure represents a point source and its color indicates the seismic moment of the source. Darker colors indicate higher seismic moment with the color moving toward white as seismic moment decreases. Each arrow in the right half of the figure indicates the strike direction of the corresponding point source on the left. The axes are in the UTM coordinate system.

captures the shape of the fault trace and narrows the separation between positive and negative displacement. The area of large positive displacement is also noticeably absent. Looking at the residuals we find a mean of 0.026 cm and standard deviation of 40.1 cm. Both values have increased compared to the east-west inversion. The source distribution covers the entire area of interest, though the highest seismic moment is no longer entirely concentrated in the far top left corner, but extended across the diagonal near the fault trace. The distribution of strike angles reveals no obvious fault trace.

8.4.3.3 Using Both East-West and North-South Data

Finally, we apply the LMFit strike inversion to both the east-west and north-south deformation data simultaneously. The east-west deformation data and the corresponding model deformation are shown in Figure 8.33 and the north-south deformation and cor-

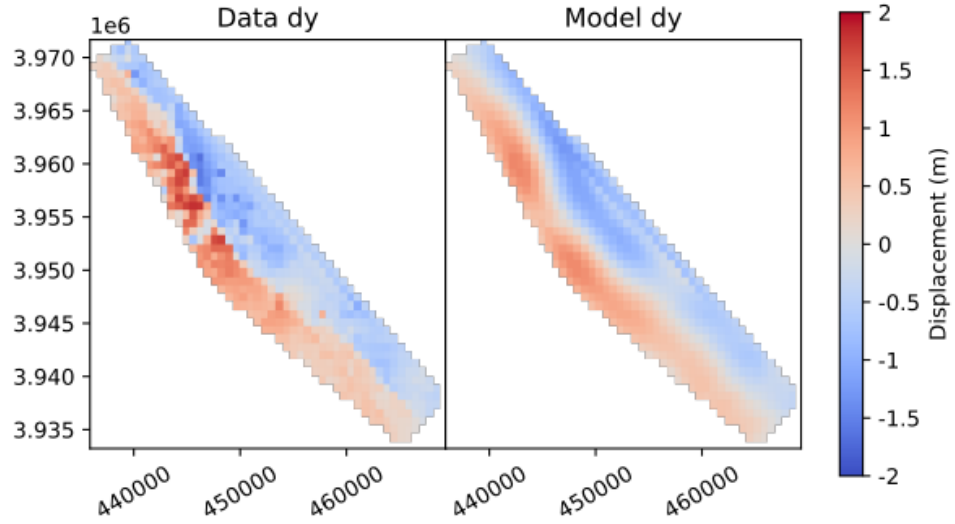

Figure 8.30. The y component of the ground deformation for the data (left) and model (right) for the LMFit inversion model. The axes are in the UTM coordinate system.

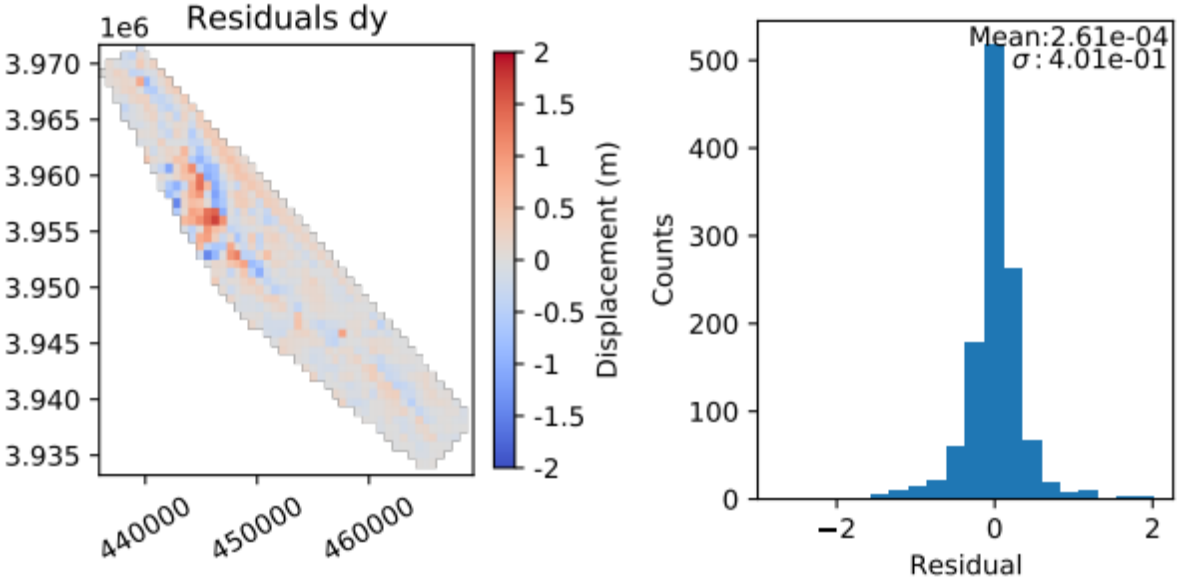

Figure 8.31. The residuals between the data and model shown in Figure 8.30 (left) and a histogram of the residuals (right).

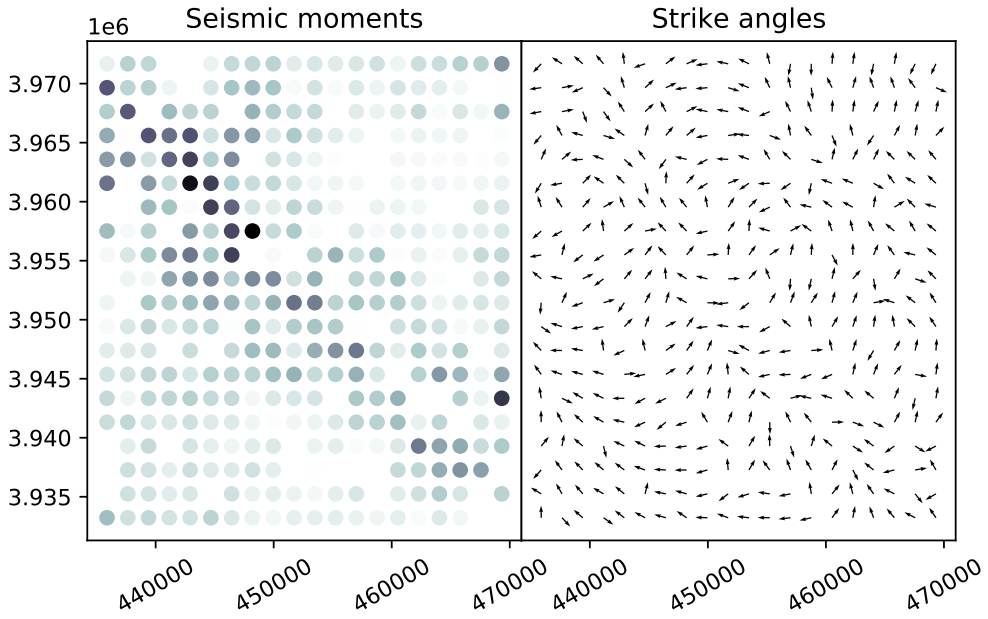

Figure 8.32. The point sources of the final LMFit inversion model shown in Figure 8.30. Each dot in the left half of the figure represents a point source and its color indicates the seismic moment of the source. Darker colors indicate higher seismic moment with the color moving toward white as seismic moment decreases. Each arrow in the right half of the figure indicates the strike direction of the corresponding point source on the left. The axes are in the UTM coordinate system.

responding model deformation are shown in Figure 8.35. The residuals in the east-west and north-south directions can be seen in Figures 8.34 and 8.36, respectively. The mean and standard deviation for all of the LMFit strike inversions are listed in Table 8.4. In both directions the mean residual remained roughly constant. The standard deviation of the residuals also changed very little. Looking at the source distribution in Figure 8.37, it places the highest seismic moment along the diagonal as we saw in Figures 8.29 and 8.32. However, there does appear to be a continuous path of sources whose strike points from the bottom right corner to the top left corner.

8.4.4 Inversion With a 40° Limit On Strike Angle

The final set of inversions we perform on the Ridgecrest data impose a limit of 40° on the strike angle. What this means is that we limit the value of the strike angle to a range

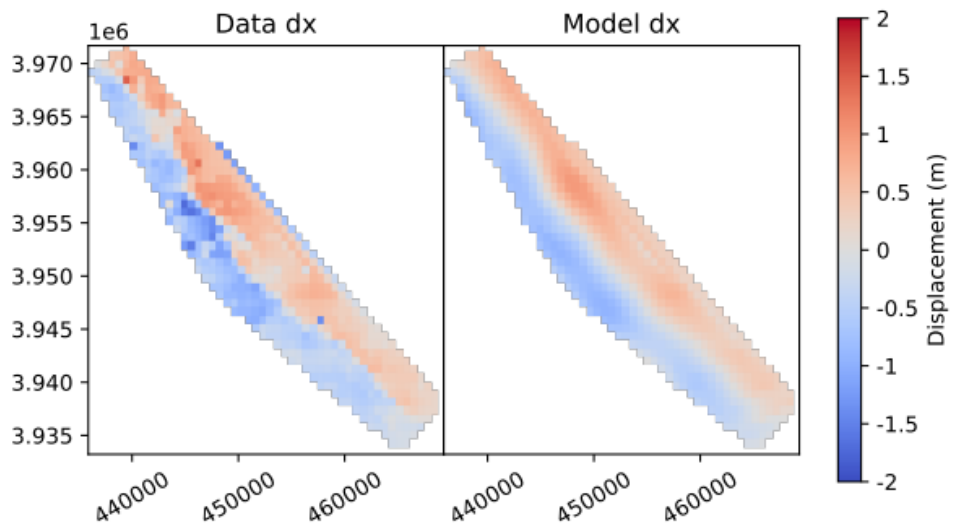

Figure 8.33. The x component of the ground deformation for the data (left) and model (right) for the LMFit inversion model. The axes are in the UTM coordinate system.

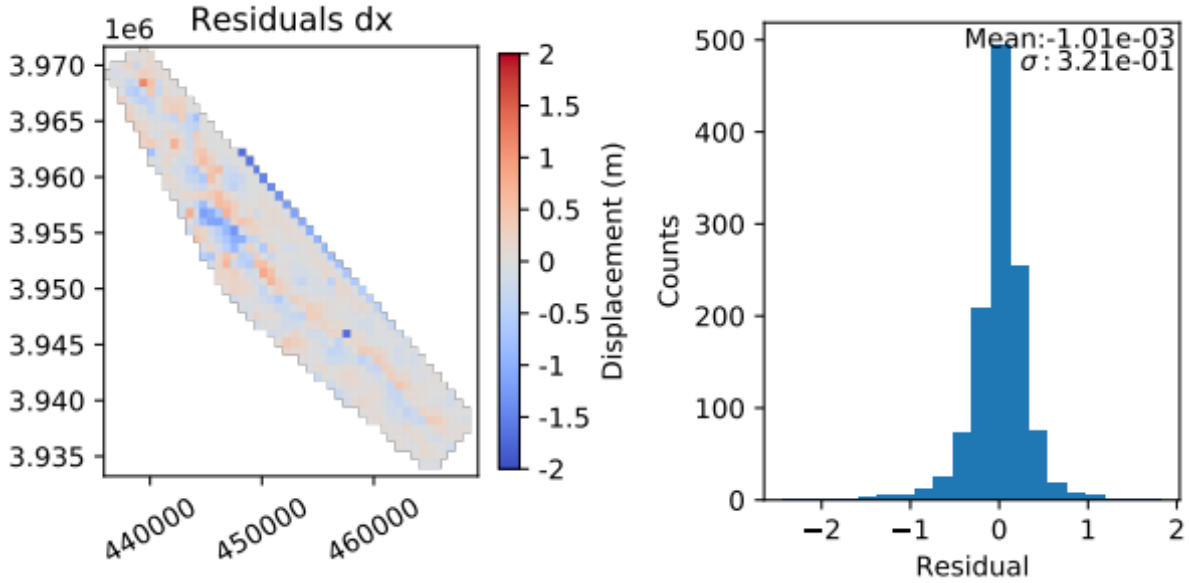

Figure 8.34. The residuals between the data and model shown in Figure 8.33 (left) and a histogram of the residuals (right).

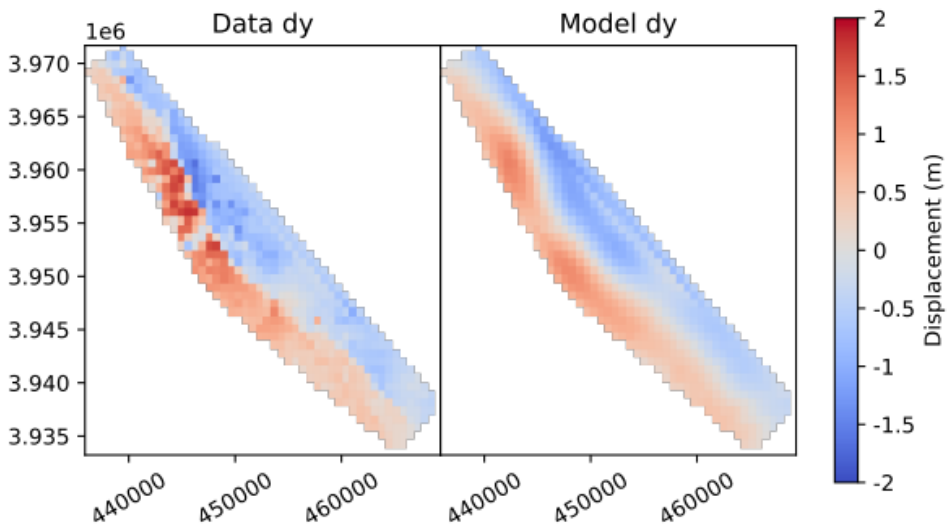

Figure 8.35. The y component of the ground deformation for the data (left) and model (right) for the LMFit inversion model. The axes are in the UTM coordinate system.

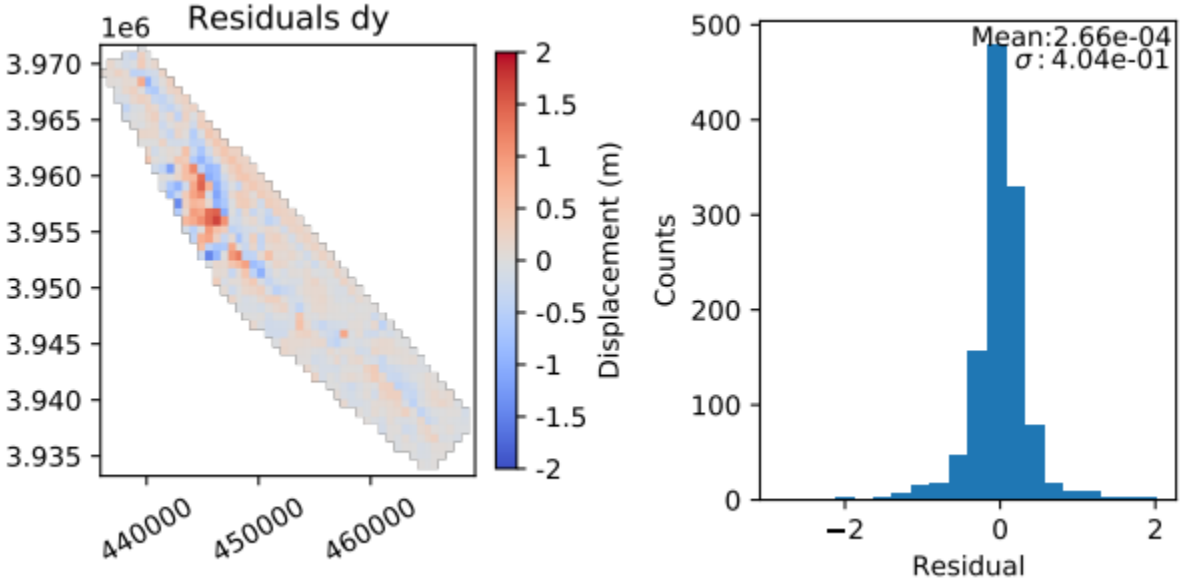

Figure 8.36. The residuals between the data and model shown in Figure 8.35 (left) and a histogram of the residuals (right).

	Mean	σ
LM - dx only	-0.022 cm	32.0 cm
LM - dy only	0.026 cm	40.1 cm
LM - both - dx	-0.101 cm	32.1 cm
LM - both - dy	0.027 cm	40.4 cm

Table 8.4. The means and standard deviations of the residuals for each LMFit strike inversion of the Ridgecrest data.

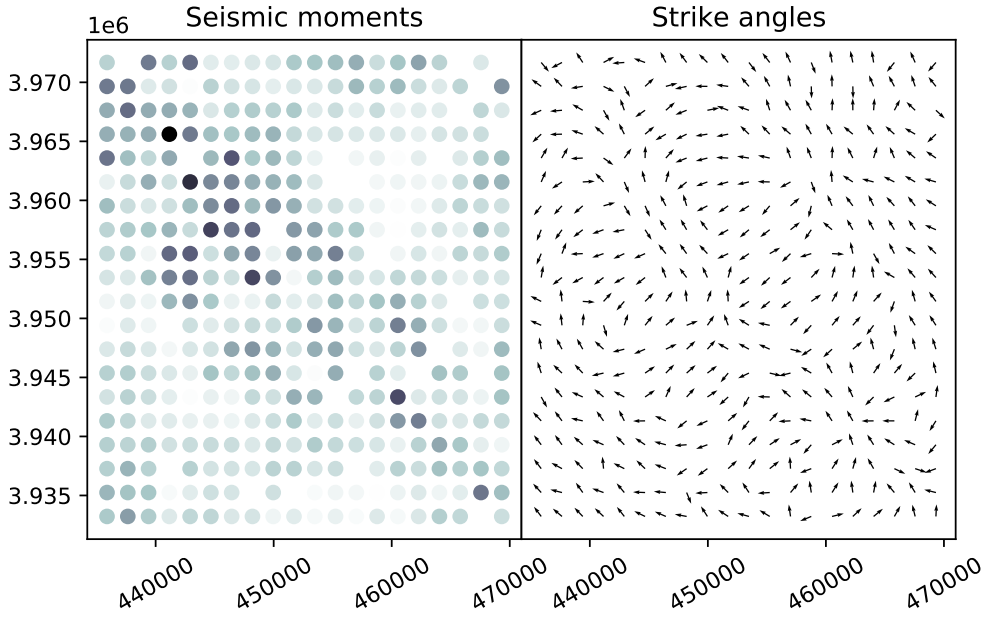

Figure 8.37. The point sources of the final LMFit inversion model shown in Figures 8.33 and 8.35. Each dot in the left half of the figure represents a point source and its color indicates the seismic moment of the source. Darker colors indicate higher seismic moment with the color moving toward white as seismic moment decreases. Each arrow in the right half of the figure indicates the strike direction of the corresponding point source on the left. The axes are in the UTM coordinate system.

of 80°, centered at the starting value of the strike angle. Our goal with this change is to force the solver to use the seismic moment of a source to control its strength rather than lowering the deformation in an area by flipping a source 180° relative to its neighbors (which is the same as multiplying the source's seismic moment by -1). Flipping a source's strike angle by 180° would essentially cause the source to destructively interfere with its neighbors. So ideally, in an area of no deformation, the seismic moments of the sources in that area are zero rather than sources with nonzero moments and opposing strike directions.

8.4.4.1 Using East-West Deformation Data

We first apply the LMFit strike inversion to the east-west component of the Ridgecrest deformation data. Figure 8.38 shows the downsampled east-west deformation data and the resulting model. The model somewhat captures the turns in the fault trace but the transition is wider than that of the inversions with no limit on the strike angle. Figure 8.39 shows the residuals between the data and model. The mean of the residuals is -0.235 cm and the standard deviation is 36.2 cm. Both the seismic moments and strike angles of the model sources are shown in Figure 8.40. The seismic moment distribution no longer spans the entire area—many of the sources away from the area of the fault trace have had their seismic moments reduced. No clear fault trace is apparent from the strike angles of the sources. Many of the sources appear to have the same strike angle—these sources had their strike angles stopped at either the upper or lower limit. Therefore, these values are not valid estimates of the strike angle if the seismic moment of the source was nonzero.

8.4.4.2 Using North-South Deformation Data

Next we apply the LMFit strike inversion to the north-south component of the Ridgecrest data. The data and corresponding model deformation are compared in Figure 8.41. This model also captures the shape of the fault trace with a slightly blurred transition between positive and negative displacement. Looking at the residuals we find a mean of 0.092 cm and standard deviation of 45.6 cm. The source distribution covers the entire area of interest, though the highest seismic moment is no longer all concentrated in the far top left corner, but extended across the diagonal near the fault trace. The seismic moment has

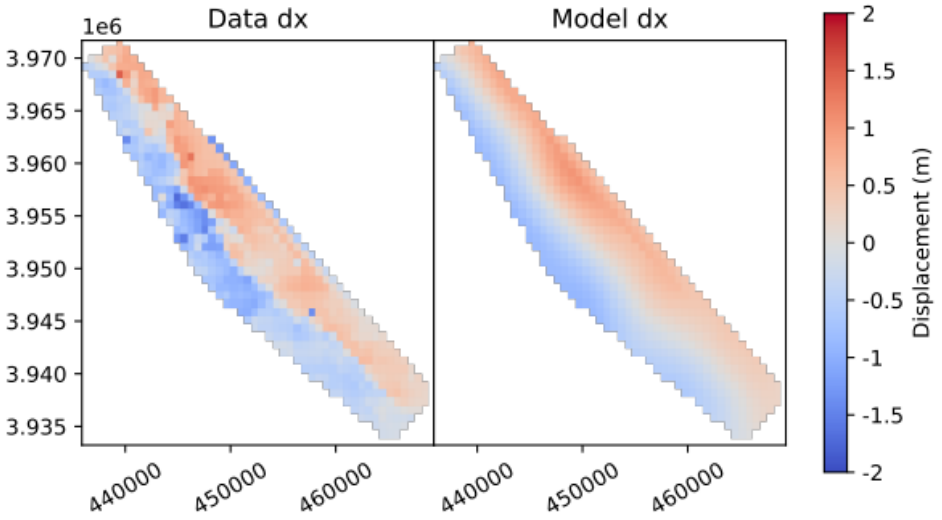

Figure 8.38. The x component of the ground deformation for the data (left) and model (right) for the LMFit inversion model. The axes are in the UTM coordinate system.

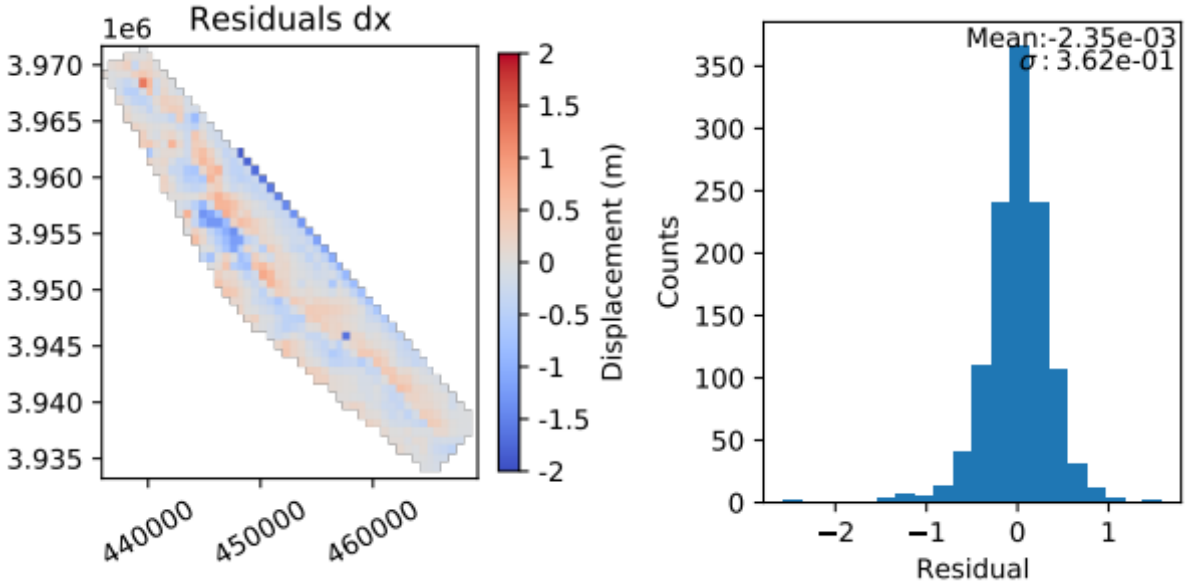

Figure 8.39. The residuals between the data and model shown in Figure 8.38 (left) and a histogram of the residuals (right).

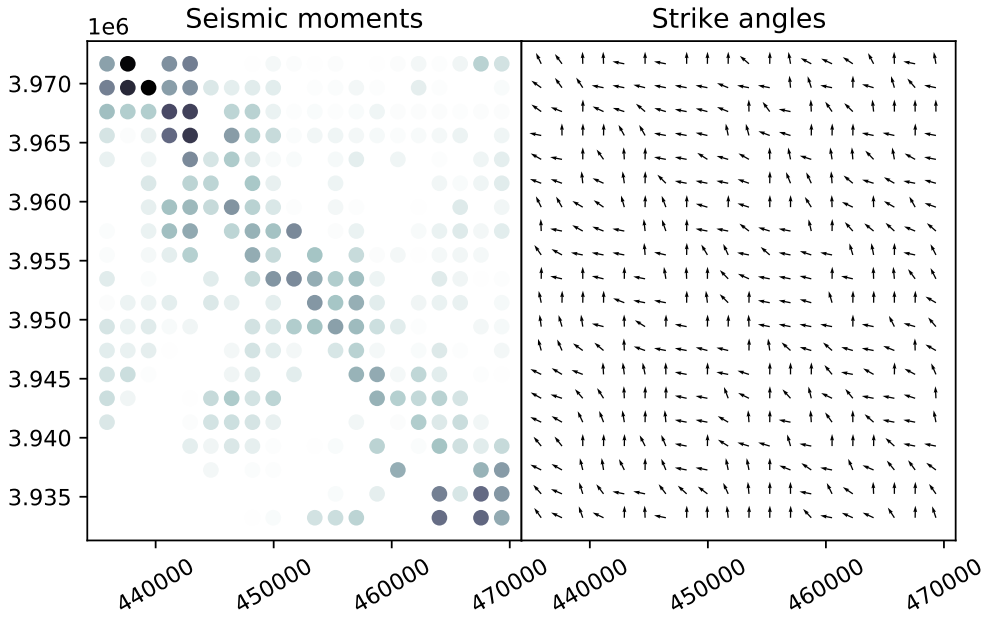

Figure 8.40. The point sources of the final LMFit inversion model shown in Figure 8.38. Each dot in the left half of the figure represents a point source and its color indicates the seismic moment of the source. Darker colors indicate higher seismic moment with the color moving toward white as seismic moment decreases. Each arrow in the right half of the figure indicates the strike direction of the corresponding point source on the left. The axes are in the UTM coordinate system.

been reduced in isolated patches but does not reveal a clear fault trace. The distribution of strike angles also reveals no obvious fault trace and suffers the same problem as the east-west inversion—many of the strike angles are stuck at the limits.

8.4.4.3 Using Both East-West and North-South Data

Finally, we apply the LMFit strike inversion to both the east-west and north-south deformation data simultaneously. The east-west deformation data and the corresponding model deformation are shown in Figure 8.44 and the north-south deformation and corresponding model deformation are shown in Figure 8.46. The residuals in the east-west and north-south directions can be seen in Figures 8.45 and 8.47, respectively. The mean and standard deviation for all of the LMFit limited strike inversions are listed in Table 8.5. In both directions the mean residual remains below 1.0 cm. The standard deviation of the

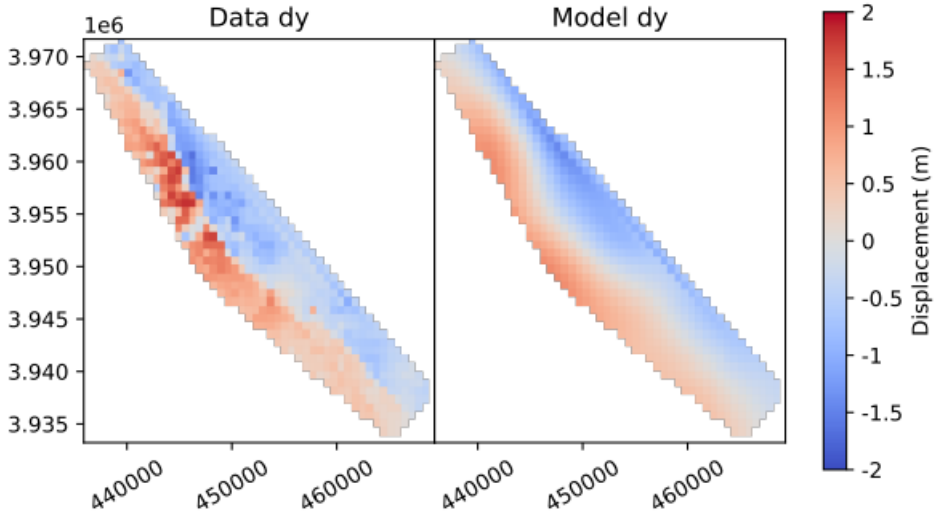

Figure 8.41. The y component of the ground deformation for the data (left) and model (right) for the LMFit inversion model. The axes are in the UTM coordinate system.

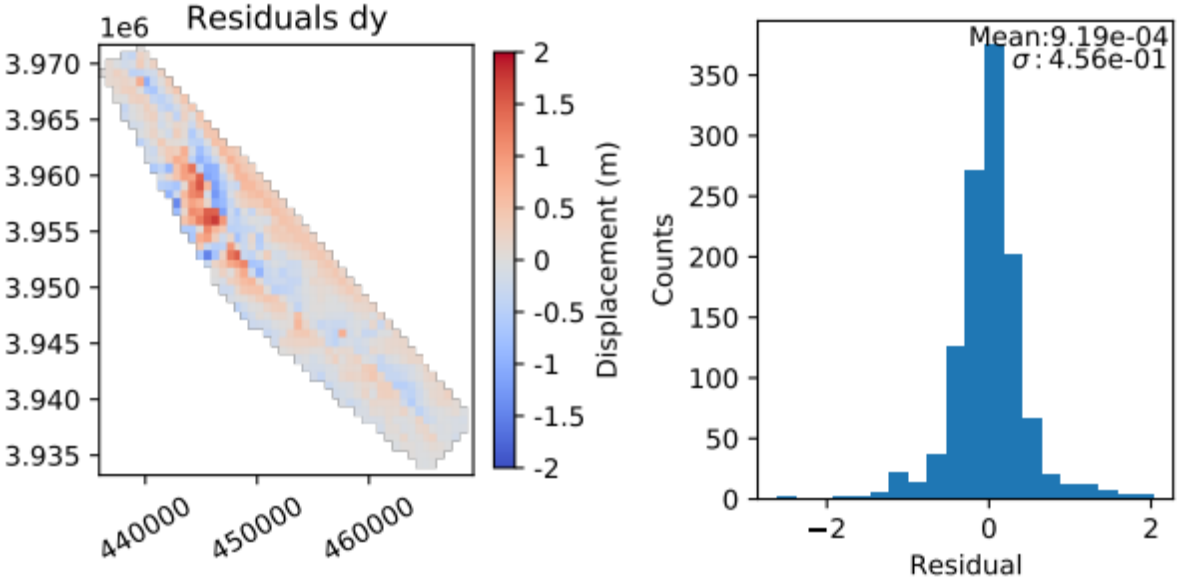

Figure 8.42. The residuals between the data and model shown in Figure 8.41 (left) and a histogram of the residuals (right).

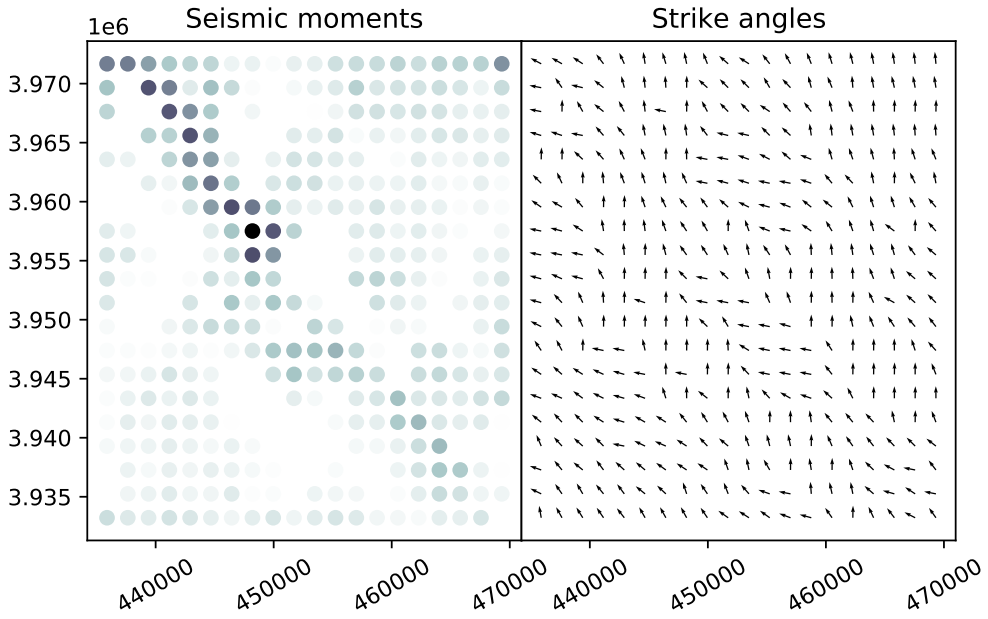

Figure 8.43. The point sources of the final LMFit inversion model shown in Figure 8.41. Each dot in the left half of the figure represents a point source and its color indicates the seismic moment of the source. Darker colors indicate higher seismic moment with the color moving toward white as seismic moment decreases. Each arrow in the right half of the figure indicates the strike direction of the corresponding point source on the left. The axes are in the UTM coordinate system.

residuals also changed very little. Compared to the previous limited strike inversions, the seismic moment distribution in Figure 8.48 is much more compact. However, it still has several branches extending from the fault trace line as well as some nonzero sources in the top right corner. There does appear to be a continuous path of sources whose strike points from the bottom right corner to the top left corner, though this could be biased by the limits placed on the strike angle.

8.5 Discussion and Conclusions

Since the fault involved in this event has a dip angle close to 90° (about 81°), it is almost vertical. Therefore, the seismic moment distribution should follow the strike of the fault. For an ideal inversion, the seismic moment distribution would follow the fault strike, with

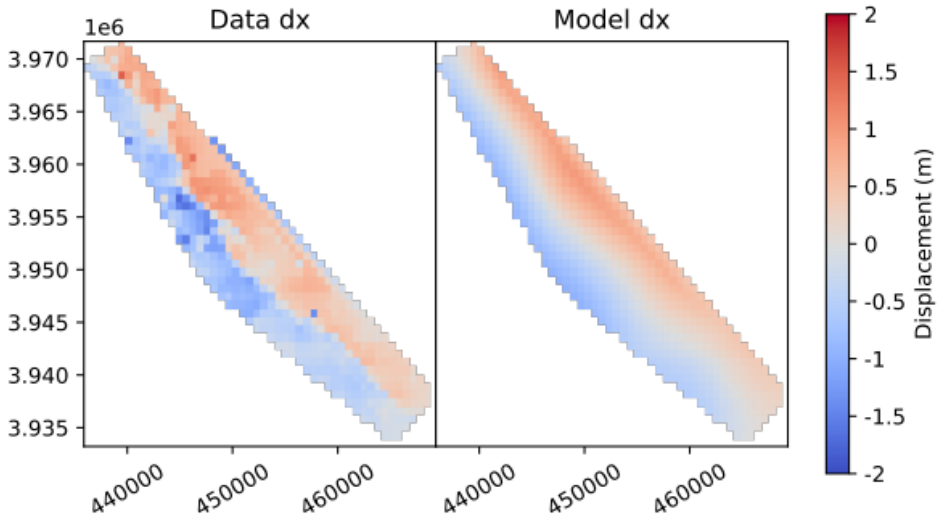

Figure 8.44. The x component of the ground deformation for the data (left) and model (right) for the LMFit inversion model. The axes are in the UTM coordinate system.

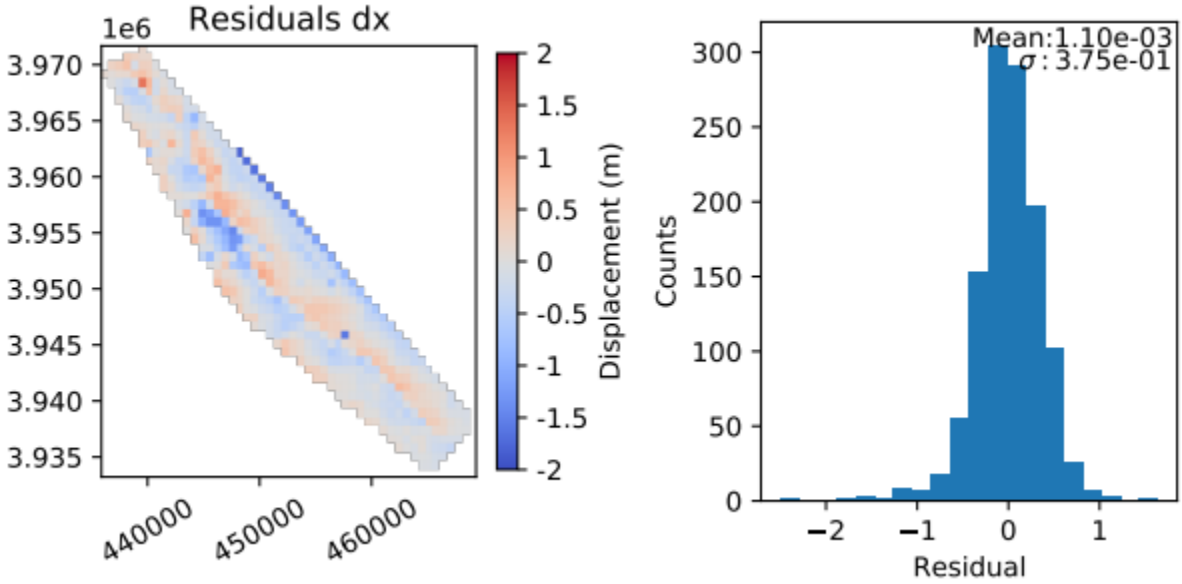

Figure 8.45. The residuals between the data and model shown in Figure 8.44 (left) and a histogram of the residuals (right).

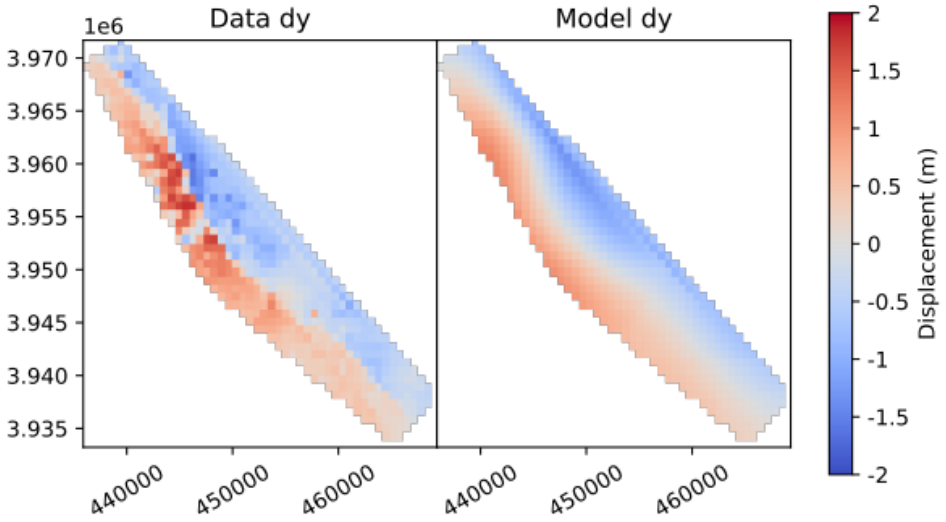

Figure 8.46. The y component of the ground deformation for the data (left) and model (right) for the LMFit inversion model. The axes are in the UTM coordinate system.

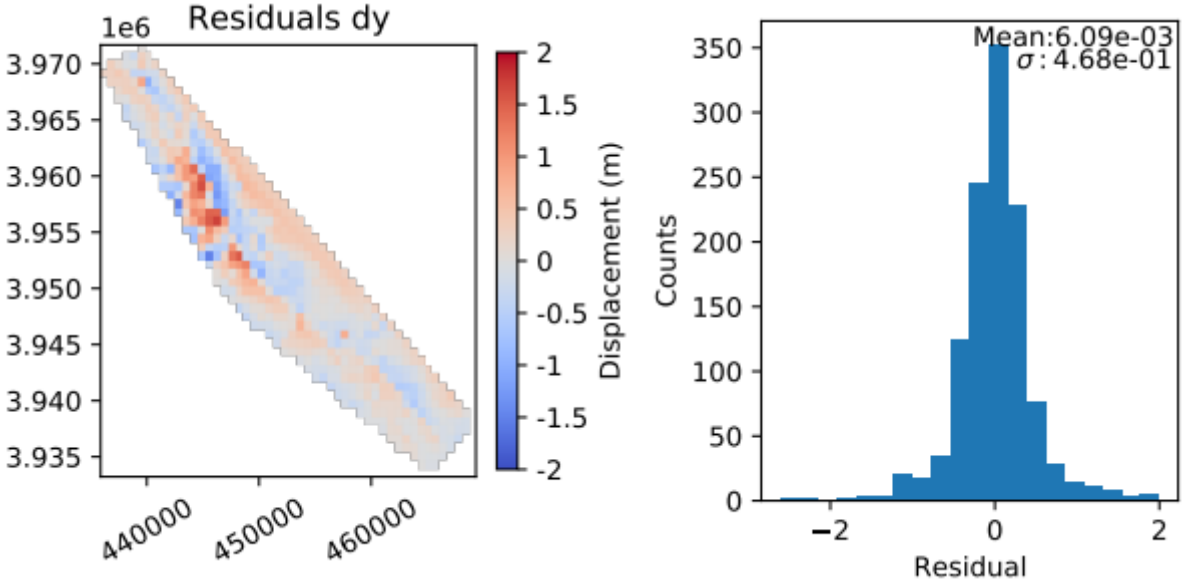

Figure 8.47. The residuals between the data and model shown in Figure 8.46 (left) and a histogram of the residuals (right).

	Mean	σ
LM Strike limit - dx only	-0.235 cm	36.2 cm
LM Strike limit - dy only	0.092 cm	45.6 cm
LM Strike limit - both - dx	0.110 cm	37.5 cm
LM Strike limit - both - dy	0.61 cm	46.8 cm

Table 8.5. The means and standard deviations of the residuals for each LMFit limited strike inversion of the Ridgecrest data.

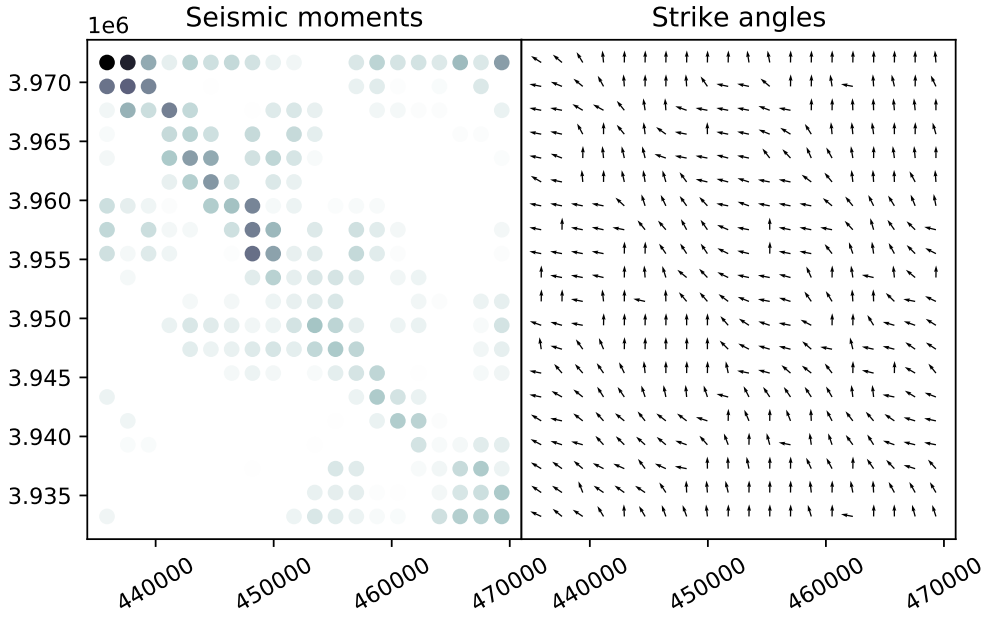

Figure 8.48. The point sources of the final LMFit inversion model shown in Figures 8.44 and 8.46. Each dot in the left half of the figure represents a point source and its color indicates the seismic moment of the source. Darker colors indicate higher seismic moment with the color moving toward white as seismic moment decreases. Each arrow in the right half of the figure indicates the strike direction of the corresponding point source on the left. The axes are in the UTM coordinate system.

	Mean	σ
MLR - dx only	-50.6 cm	37.2 cm
MLR - dy only	11.0 cm	46.6 cm
MLR - both - dx	-7.16 cm	41.0 cm
MLR - both - dy	-4.81 cm	49.5 cm
LM - dx only	-1.34 cm	38.8 cm
LM - dy only	2.04 cm	48.2 cm
LM - both - dx	-3.85 cm	41.8 cm
LM - both - dy	-0.057 cm	50.3 cm
LM Strike - dx only	-0.022 cm	32.0 cm
LM Strike - dy only	0.026 cm	40.1 cm
LM Strike - both - dx	-0.101 cm	32.1 cm
LM Strike - both - dy	0.027 cm	40.4 cm
LM Strike limit - dx only	-0.235 cm	36.2 cm
LM Strike limit - dy only	0.092 cm	45.6 cm
LM Strike limit - both - dx	0.110 cm	37.5 cm
LM Strike limit - both - dy	0.61 cm	46.8 cm

Table 8.6. The means and standard deviations of the residuals for each inversion of the Ridgecrest data. MLR refers to the multiple linear regression inversion. LM refers to the LMFit inversions for seismic moment. LM Strike refers to the LMFit inversions for seismic moment and strike angle. LM Strike limit refers to the LMFit inversions for seismic moment and strike angle, with a limit of 40° placed on the strike angle.

higher seismic moment sources being placed at points along the strike where the highest slip occurred.

The means and standard deviations of the residuals for every inversion performed in this chapter are collected in Table 8.6. Of all of the inversions, the lowest mean residuals were achieved by the LMFit inversion for the strike angle and seismic moment, with no limit placed on the strike angle. This is expected, as it is the inversion with the largest amount of freedom in its parameters and all of the inversions rely on the same set of equations. While the mean residuals frequently fell below 1.0 cm, the standard deviation

of the residuals only fell as low as 32.0 cm. We believe this to be due to the speckle present in the interferograms. The maximum value of some of the error pixels reaches as high as 6 m, whereas the maximum displacement of the earthquake is known to be around 2 m. While we placed a limit of 2 m when downsampling the data, this doesn't affect any of the pixels that lie below that limit. Therefore, the speckle's effect cannot be completely removed when it overlaps the data of interest. This happens near the peak displacement in the north-south deformation data, where the speckle overlaps the fault trace. Since the speckle rapidly changes from maximum to minimum displacement across a single pixel boundary, it contributes greatly to the standard deviation of the residuals since the models produce smooth, continuous deformation. Future inversions could validate the results presented in this thesis using either a different set of interferograms for the Ridgecrest mainshock or by applying a filter that is able to remove or minimize the effect of the speckle.

Despite the large standard deviation of each inversion, two stand out that were able to provide a trace of the major fault line associated with the Ridgecrest mainshock, the multiple linear regression inversion of both datasets in Figure 8.15 and the LMFit moment inversion of both datasets in Figure 8.26. Both place the highest seismic moment in the upper left corner and the distribution extends toward the bottom right along the path of the fault. Each distribution follows the true fault line which is visible in both interferograms in Figure 8.4. The source distribution in Figure 8.26 is more diffuse, which could possibly be improved by increasing the number of sources in the model. Currently, the sources are spaced several kilometers apart, heavily limiting the resolution of the model.

Thus far, our analysis has discussed the ability of our inversions to model ground deformation data. To extract further information about the trace of the fault we mentioned previously, we require a method that allows us to quantify the structure of the traces so that we don't rely solely on by-eye comparisons. This leads us to our next step: fractal analysis.

Chapter 9

Fractal Analysis

A fractal is an object that exhibits self-similarity at all scales. What this means is that the object appears the same no matter how far you zoom in to look at it (i.e. it looks the same at all scales). The most well-known example of a fractal—the length of a coastline—comes from Mandelbrot's original paper which also introduced the idea of a non-integer dimension (also called a fractal dimension) [53]. Since then, fractal dimensions have been used to quantify the characteristics of fractal objects in a wide variety of contexts from river networks [54] to human physiology [55] to the paintings of Jackson Pollock [56].

Fractal patterns occur frequently during fracture processes, having been found in the fracturing of: steel under plane strain [57], concrete by wedge-splitting [58] and natural rock [59], as well as many other materials. As a result, fractals are also common in earthquake processes. The fractal dimension of earthquake epicenters has been investigated by many groups including, but not limited to the authors of [60], [61] and [62]. The authors of [63] extended this type of analysis by also estimating the fractal dimension of active faults in Japan.

To extend our analysis of the point source distributions from our inversions of the M_w 7.1 Ridgecrest mainshock, we calculate their fractal dimensions. This allows us to quantify their structure in a systematic way so that we have a reliable method to compare the fractal dimensions of the inversion results, the aftershock distribution and the fault traces. The goal of this comparison is to determine whether the seismic moment distribution from the

inversions tells us more about the area of possible aftershocks or the specific faults upon which the earthquake occurred.

9.1 Box-Counting

We use a technique called the box-counting method to estimate the fractal dimensions we report in this chapter. The basic idea of the box-counting method is to overlay a series of square grids of decreasing box sizes over the system in question and count how many of the boxes are required to completely cover the system for each grid. The fractal dimension is then defined by the equation:

$$D = \lim_{\epsilon \to \infty} -\frac{logN(\epsilon)}{log(\epsilon)} \tag{9.1}$$

where $N(\epsilon)$ is the number of boxes required to cover the system for a grid composed of squares of side length ϵ. The fractal dimension is generally estimated by plotting $N(\epsilon)$ vs ϵ on a log-log plot and fitting a line to the resulting distribution. In practice it is not possible to reduce the grid sizes to arbitrarily small lengths, so the minimum ϵ is generally chosen to be low enough to capture the fractal nature of the system in question without introducing numerical errors.

To estimate the fractal dimension of our point source distributions, we first apply a filter which removes sources from the distribution if their seismic moment is below a specified threshold value. We then estimate the fractal dimension of the remaining sources using box counting. The fractal dimension is estimated at multiple threshold values and we produce a plot of the fractal dimension as a function of the applied threshold. The results of this analysis on the Ridgecrest inversions are shown in Figures 9.3 and 9.4 for the cases with no limit on the strike angle and with a limit on the strike angle, respectively.

Estimating the fractal dimension of the fault traces works slightly differently from that of the point source estimates. Since we have an image of the traces we perform a pixel-based fractal analysis. The points of the system we're trying to cover with the boxes are now represented by black pixels, while the empty space is represented by white pixels. Otherwise, the idea remains the same—we count how many boxes are required to cover the system for a series of grids with decreasing box sizes.

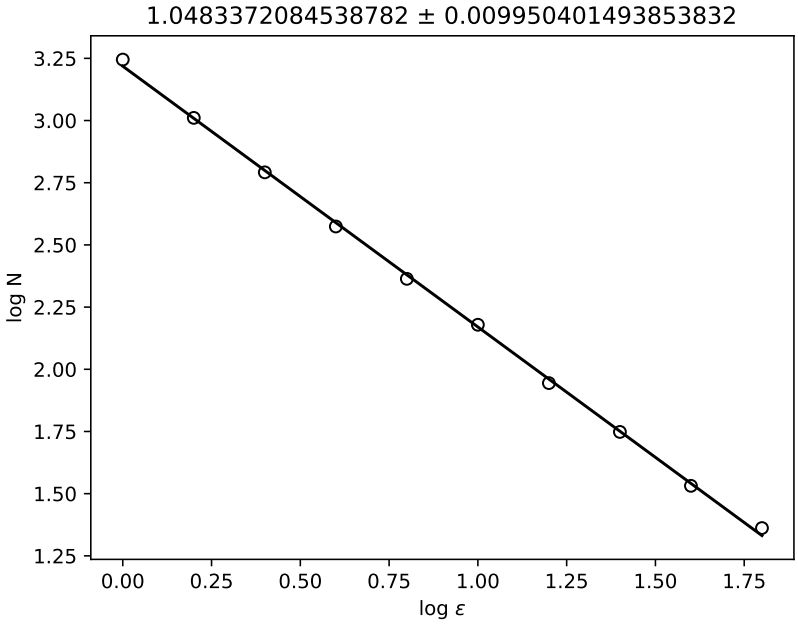

Figure 9.1. The linear fit used to estimate the fractal dimension of the fault trace image in Figure 8.1. The fractal dimension is listed in the title.

9.2 Results

The fractal dimension of the fault traces will be the basis of our analysis since the traces are well constrained by multiple sources. The linear fit used to estimate the value of their fractal dimension can be seen in Figure 9.1. This estimate is the result of pixel box counting on the image in Figure 8.1. The grid sizes used range from 1 pixel to 63 pixels and are applied on the image which is 515 x 389 pixels. With these parameters, the fractal dimension is estimated to be 1.048337 ± 0.009950.

The fractal dimension of the aftershock locations is estimated using point-based box counting. The linear fit used to estimate the fractal dimension is shown in Figure 9.2. The grid sizes used in this estimate range from 1km to 10km.

The inversion results are displayed in Figures 8.33-8.37 for the case where the strike angle has no limit. We focus specifically on the left side of Figure 8.37 for our fractal analysis. The fractal dimension of the point sources as a function of the applied threshold is shown in Figure 9.3.

The inversion results are displayed in Figures 8.44-8.48 for the case where the strike

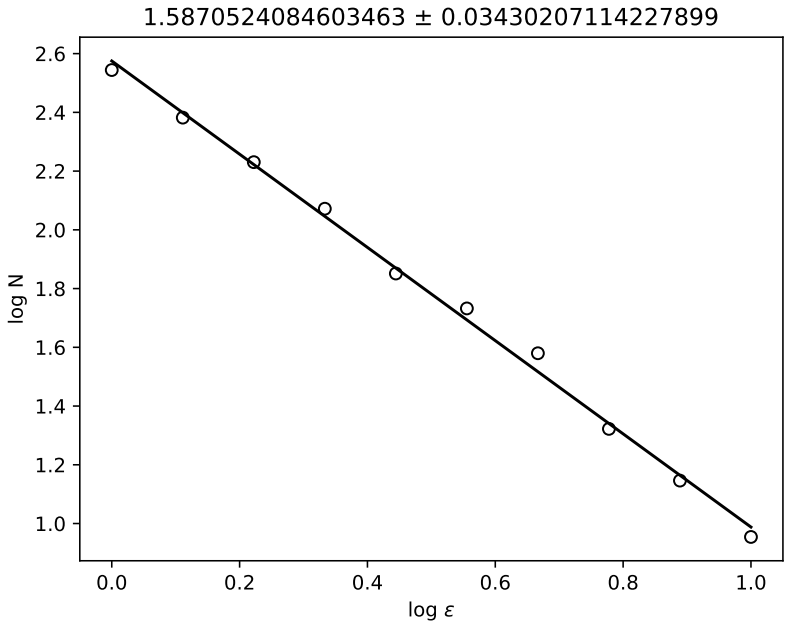

Figure 9.2. The linear fit used to estimate the fractal dimension of the aftershock locations in Figure 8.3. The fractal dimension is listed in the title.

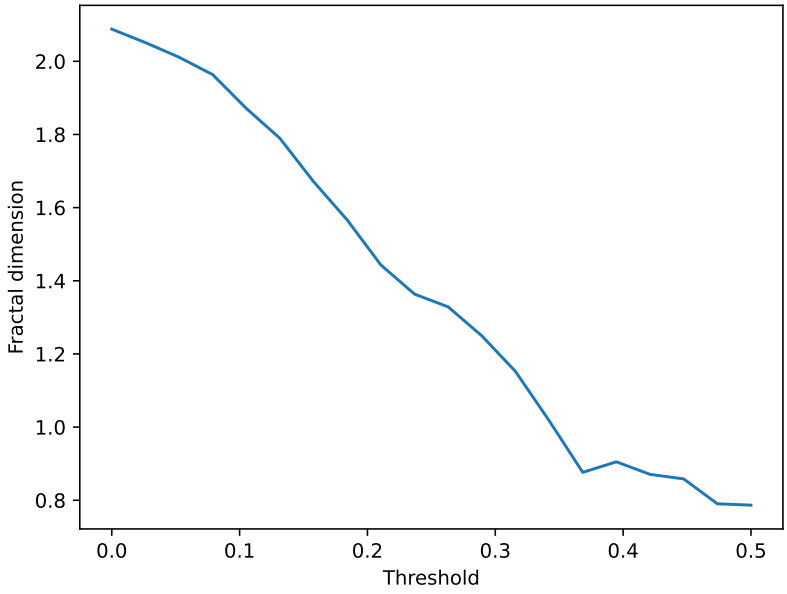

Figure 9.3. The estimated fractal dimension of the system of point sources (with no limit on strike angle) as a function of the seismic moment threshold. The threshold axis is in units of the maximum seismic moment of the distribution.

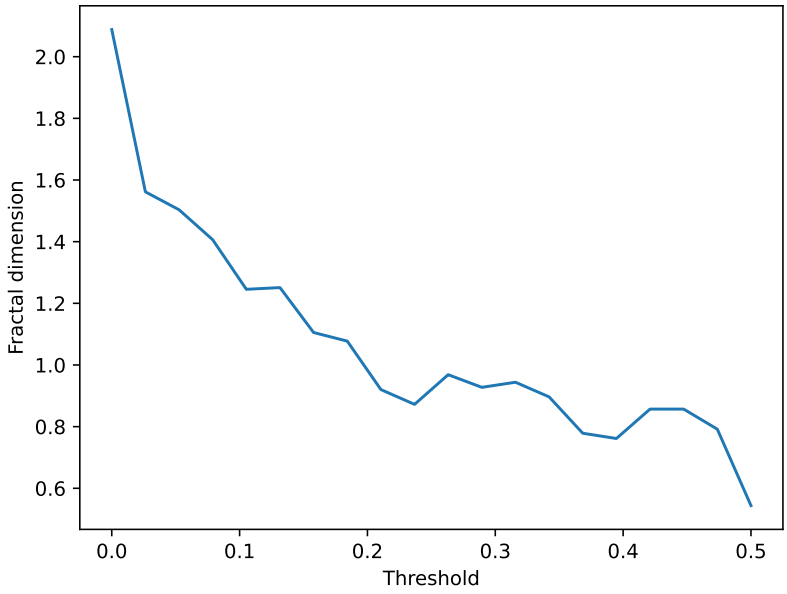

Figure 9.4. The estimated fractal dimension of the system of point sources (with a limit of 40° on the strike angle) as a function of the seismic moment threshold. The threshold axis is in units of the maximum seismic moment of the distribution.

angle is limited to be within 40° on either side of the starting value. The fractal dimension of the point sources as a function of the applied threshold is shown in Figure 9.4.

We also use point-based box counting to estimate the fractal dimension of the distribution of point sources resulting from the inversion. The distribution starts as a 20 x 20 grid of sources for a total of 400 points. A threshold is applied to the distribution which removes points from the distribution if their seismic moment is below the threshold. For example, a threshold of 0.2 indicates that the points with seismic moment below 20% of the maximum value of the distribution were removed and not considered in the box counting analysis. The estimated fractal dimension as a function of the threshold can be seen in Figures 9.3 and 9.4 for the cases without and with a limit on the strike angle, respectively.

9.3 Discussion and Conclusion

For both cases (with and without a limit on the strike angle) there exists a threshold at which the estimated fractal dimension of the model is approximately equal to the fractal

Distribution	Fractal dimension
Fault traces	1.048337 ± 0.009950
Point sources (no limit)	1.049246 ± 0.033324
Point sources (with limit)	1.028219 ± 0.081766

Table 9.1. Comparison of the fractal dimension of the fault traces to the fractal dimension of the point source distributions after applying a threshold on their seismic moment.

Distribution	Fractal dimension
Aftershocks	1.587052 ± 0.034302
Point sources (no limit)	1.583604 ± 0.037285
Point sources (with limit)	1.582805 ± 0.063705

Table 9.2. Comparison of the fractal dimension of the aftershock distribution to the fractal dimension of the point source distributions after applying a threshold on their seismic moment.

dimension of the fault traces and the aftershock distribution. The results of each case are compared to the fractal dimension of the fault traces in Table 9.1 and to the fractal dimension of the aftershock distribution in Table 9.2. Figures showing the point source distributions with the thresholds applied can be seen in Figures 9.5-9.8.

The total number of aftershocks is fairly low–only 1,430. Due to the low number of aftershocks the accuracy of the fractal dimension estimate is reduced. Ideally the range of grid sizes spans several orders of magnitude, while the analysis in Figure 9.2 spans only one. The accuracy is therefore limited by the minimum possible grid spacing, which must lie above the minimum separation distance of the points to avoid introducing numerical errors. Similar errors are present in the box counting of the point source distributions since they start with only 400 points and are reduced further by the applied thresholds. The most obvious solution is to increase the number of points in the model used in the inversion. However, this will greatly increase the computational complexity of the problem. Another possible solution is to upscale the current distribution to a larger number of points using interpolation; however, preliminary tests to this end showed a significant change to the fractal dimension estimates. Whether they are moving toward

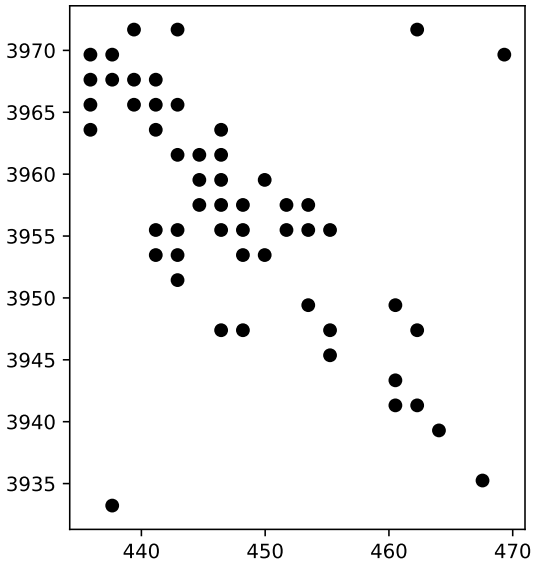

Figure 9.5. The distribution of point sources with no limit on strike angle after applying the threshold that yields a fractal dimension close to that of the fault traces.

the true value or the change occurs because the distribution is not truly scale invariant will be investigated in the future.

9.4 Concluding Remarks

Our point source inversion method has been shown to be effective in recreating the ground deformation caused by significant earthquakes. Armed with the information from a traditional rectangular fault inversion, our method can provide further information about either the slip distribution on the fault or the trace of the fault, depending on the fault geometry. Our method would be of particular usefulness in scenarios where the trace of the fault is not known beforehand, known as a "blind thrust" event. Current inversions for the slip distributions on complicated faults require the manual definition of multiple connected rectangular segments that follow along the fault. A point source inversion does not require a definition of the geometry before the inversion—we only require a focal mechanism, one of the first calculations performed upon detecting an earthquake.

Another benefit to our method is that it has not been fully explored. Our inversions

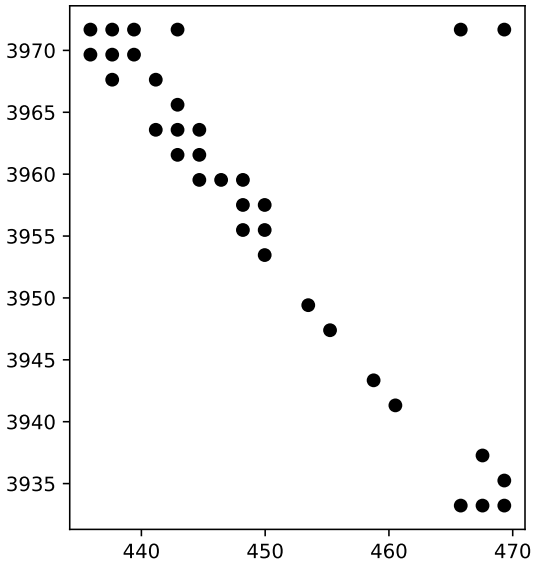

Figure 9.6. The distribution of point sources with a limit on strike angle after applying the threshold that yields a fractal dimension close to that of the fault traces.

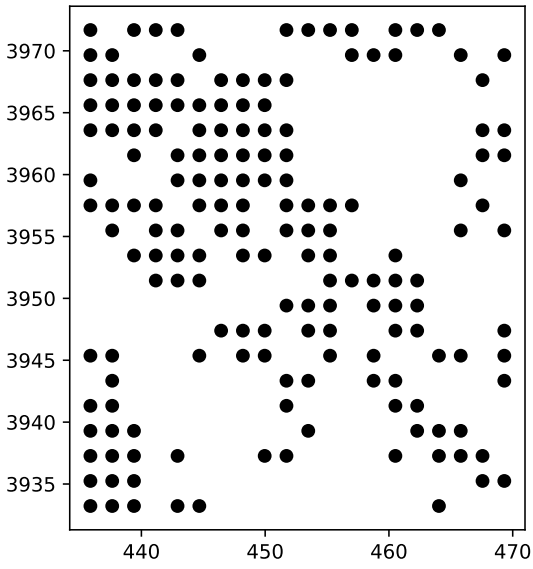

Figure 9.7. The distribution of point sources with no limit on strike angle after applying the threshold that yields a fractal dimension close to that of the aftershock distribution.

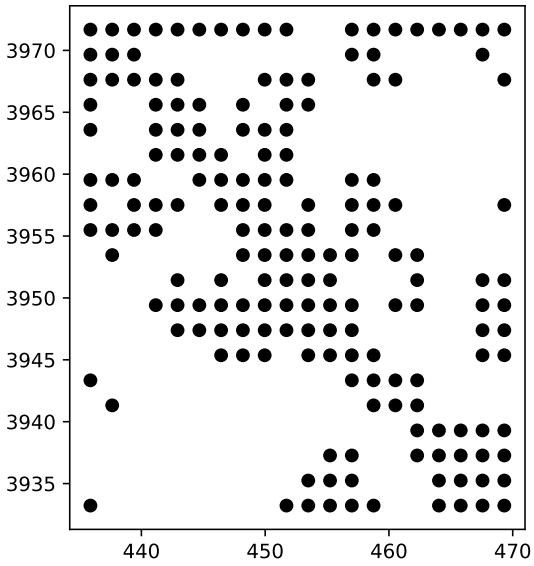

Figure 9.8. The distribution of point sources with a limit on strike angle after applying the threshold that yields a fractal dimension close to that of the aftershock distribution.

thus far have only included seismic moment and strike angle because they can be included with limited computational power. The other parameters could still be explored with a similar computational demand as the current version. The locations of the sources could be included as a parameter through a translation of a pre-calculated deformation field. The inclusion of rake angle would only expand the requirements to two pre-calculated Green's matrices, which would be combined using the appropriate components of the slip vector. Source depth or dip angle would require the complete recalculation of Okada's equations for each change in the source parameters and so would require much greater computational resources. The future of our inversion method remains open and waiting to be explored.

References

[1] A. Burtin, N. Hovius, and J. M. Turowski, "Seismic monitoring of torrential and fluvial processes," *Earth Surface Dynamics*, vol. 4, no. 2, pp. 285–307, 2016.

[2] R. M. Hohensinn, *Detection of Hazardous Ground Movements with Instantaneous Velocity Estimates by GNSS*. PhD thesis, ETH Zurich, 2019.

[3] USGS, "Earthquake glossary: seismograph." `https://earthquake.usgs.gov/learn/glossary/?term=seismograph` (accessed 2022-06-17).

[4] M. Norton, "Fitting nodal planes to data from a hypothetical earthquake," 2008. `https://commons.wikimedia.org/wiki/File:Focal_mechanism_02.jpg` (accessed: 2022-06-16).

[5] Y. Okada, "Surface deformation due to shear and tensile faults in a half-space," *Bull. of the Seismol. Soc. of Am.*, vol. 75, no. 4, pp. 1135–1154, 1985.

[6] NASA/JPL-Caltech, "Interferometry." `https://nisar.jpl.nasa.gov/mission/get-to-know-sar/interferometry/` (accessed: 2020-07-02).

[7] D. J. Ponti, J. L. Blair, C. M. Rosa, K. Thomas, A. J. Pickering, S. Akciz, S. Angster, J. Avouac, J. Bachhuber, S. Bacon, N. Barth, S. Bennett, K. Blake, S. Bork, B. Brooks, T. Bullard, P. Burgess, C. Chupik, T. Dawson, M. DeFrisco, J. Delano, S. DeLong, J. Dolan, A. Donnellan, C. DuRoss, T. Ericksen, E. Frost, G. Funning, R. Gold, N. Graehl, C. Gutierrez, E. Haddon, A. Hatem, J. Helms, J. Hernandez, C. Hitchcock, P. Holland, K. Hudnut, K. Kendrick, R. Koehler, O. Kozaci, T. Ladinsky, R. Leeper, C. Madugo, M. Mareschal, J. McDonald, D. McPhillips, C. Milliner, D. Mongovin, A. Morelan, S. Nale, J. Nevitt, M. O'Neal, B. Olson, M. Oskin, S. Padilla, J. Patton, B. Philibosian, I. Pierce, C. Pridmore, N. Roth, D. Sandwell, K. Scharer, G. Seitz, D. Singleton, B. Smith-Konter, E. Spangler, B. Swanson, J. T. Jobe, J. Treiman, F. Valencia, J. Vanderwal, A. Williams, X. Xu, J. Zachariasen, J. Zimmerman, and R. Zinke, "Documentation of Surface Fault Rupture and Ground-Deformation Features Produced by the 4 and 5 July 2019 Mw 6.4 and Mw 7.1 Ridgecrest Earthquake Sequence," *Seismological Research Letters*, vol. 91, pp. 2942–2959, 07 2020.

[8] United States Geological Survey, "M 7.1 - 2019 ridgecrest earthquake sequence." `https://earthquake.usgs.gov/earthquakes/eventpage/ci38457511/executive`, 2019. accessed: 2022-03-28.

[9] E. O. Lindsey, R. Natsuaki, X. Xu, M. Shimada, M. Hashimoto, D. Melgar, and D. T. Sandwell, "Nepal Earthquake ALOS-2 InSAR," 2015. `https://topex.ucsd.edu/nepal/` (accessed: 2020-06-09).

[10] X. Zhao, C. Wang, H. Zhang, Y. Tang, B. Zhang, and L. Li, "Inversion of seismic source parameters from satellite insar data based on deep learning," *Tectonophysics*, vol. 821, p. 229140, 2021.

[11] W. Le-Yang, G. Hua, and F. Guang-Cai, "Insar and gps earthquake source parameter inversion for the 2016 mw6.4 meinong, taiwan earthquake," *Chinese Journal of Geophysics*, vol. 60, no. 4, pp. 346–357, 2017.

[12] J. Salichon, B. Delouis, P. Lundgren, D. Giardini, M. Costantini, and P. Rosen, "Joint inversion of broadband teleseismic and interferometric synthetic aperture radar (insar) data for the slip history of the mw = 7.7, nazca ridge (peru) earthquake of 12 november 1996," *Journal of Geophysical Research: Solid Earth*, vol. 108, no. B2, 2003.

[13] R. Bürgmann, P. A. Rosen, and E. J. Fielding, "Synthetic aperture radar interferometry to measure earth's surface topography and its deformation," *Ann. Rev. of Earth and Planet. Sci.*, vol. 28, no. 1, pp. 169–209, 2000.

[14] Jet Propulsion Laboratory, California Institute of Technology, "What is UAVSAR?." `https://uavsar.jpl.nasa.gov/education/what-is-uavsar.html`, 2014. (accessed: 2020-06-16).

[15] H. Fattahi and F. Amelung, "InSAR uncertainty due to orbital errors ," *Geophysical Journal International*, vol. 199, no. 1, pp. 549–560, 2014.

[16] H. Fattahi and F. Amelung, "Insar bias and uncertainty due to the systematic and stochastic tropospheric delay," *Journal of Geophysical Research: Solid Earth*, vol. 120, no. 12, pp. 8758–8773, 2015.

[17] X.-l. Ding, Z.-w. Li, J.-j. Zhu, G.-c. Feng, and J.-p. Long, "Atmospheric effects on insar measurements and their mitigation," *Sensors (Basel)*, vol. 8, no. 9, pp. 5426–5448, 2008.

[18] A. Ferretti, G. Savio, R. Barzaghi, A. Borghi, S. Musazzi, F. Novali, C. Prati, and F. Rocca, "Submillimeter accuracy of insar time series: Experimental validation," *IEEE Transactions on Geoscience and Remote Sensing*, vol. 45, no. 5, pp. 1142–1153, 2007.

[19] M. Bagnardi and A. Hooper, "Inversion of surface deformation data for rapid estimates of source parameters and uncertainties: A bayesian approach," *Geochem., Geophys., Geosyst.*, vol. 19, no. 7, pp. 2194–2211, 2018.

[20] W. K. Hastings, "Monte Carlo sampling methods using Markov chains and their applications," *Biometrika*, vol. 57, no. 1, pp. 97–109, 1970.

[21] M.-J. Jo, H.-S. Jung, and S.-H. Yun, "Retrieving precise three-dimensional deformation on the 2014 m6.0 south napa earthquake by joint inversion of multi-sensor sar," *Sci. Rep.*, vol. 7, 2017.

[22] W. Feng, Z. Li, J. R. Elliott, Y. Fukushima, T. Hoey, A. Singleton, R. Cook, and Z. Xu, "The 2011 M_w 6.8 Burma earthquake: fault constraints provided by multiple SAR techniques," *Geophys. J. Int.*, vol. 195, no. 1, pp. 650–660, 2013.

[23] J. Kennedy and R. Eberhart, "Particle swarm optimization," in *Proc. of ICNN'95 - Int. Conf. on Neural Networks*, vol. 4, pp. 1942–1948, 1995.

[24] Y. Wen, C. Xu, Y. Liu, and G. Jiang, "Deformation and source parameters of the 2015 m_w 6.5 earthquake in pishan, western china, from sentinel-1a and alos-2 data," *Remote Sens.*, vol. 8, no. 2, 2016.

[25] Z. Li, Y. Wen, P. Zhang, Y. Liu, and Y. Zhang, "Joint inversion of gps, leveling, and insar data for the 2013 lushan (china) earthquake and its seismic hazard implications," *Remote Sens.*, vol. 12, no. 4, p. 715, 2020.

[26] X. Liu and W. Xu, "Logarithmic model joint inversion method for coseismic and postseismic slip: Application to the 2017 m_w 7.3 sarpol zahāb earthquake, iran," *J. of Geophys. Res.: Solid Earth*, vol. 124, no. 11, pp. 12034–12052, 2019.

[27] L. Zhang, J. C. Wu, L. L. Ge, X. L. Ding, and Y. L. Chen, "Determining fault slip distribution of the chi-chi taiwan earthquake with gps and insar data using triangular dislocation elements," *J. of Geodyn.*, vol. 45, no. 4-5, pp. 163–168, 2008.

[28] G. Jiang, C. Xu, Y. Wen, Y. Liu, Z. Yin, and J. Wang, "Inversion for coseismic slip distribution of the 2010 M_w 6.9 Yushu Earthquake from InSAR data using angular dislocations," *Geophys. J. Int.*, vol. 194, no. 2, pp. 1011–1022, 2013.

[29] Y. Fukahata and T. J. Wright, "A non-linear geodetic data inversion using abic for slip distribution on a fault with an unknown dip angle," *Geophys. J. Int.*, vol. 173, pp. 353–364, 2008.

[30] Y. Fukahata and M. Hashimoto, "Simultaneous estimation of the dip angles and slip distribution on the faults of the 2016 kumamoto earthquake through a weak nonlinear inversion of insar data," *Earth, Planets and Space*, vol. 68, 2016.

[31] M. Frietsch, A. M. G. Ferreira, G. J. Funning, and J. Weston, "Multiple fault modelling combining seismic and geodetic data: the importance of simultaneous sub-event inversions," *Geophys. J. Int.*, vol. 218, pp. 958–976, 2019.

[32] M. Peng, C. Zhao, Q. Zhang, J. Zhang, and Y. Liu, "Ground subsidence monitoring with mt-insar and mechanism inversion over xi'an, china," *ISPRS - Int. Archives of the Photogramm., Remote Sens. and Spatial Inf. Sci.*, vol. XLII-3, pp. 1375–1380, 2018.

[33] N. Langet, B. Goertz-Allmann, V. Oye, R. Bauer, S. Williams-Stroud, A. Dichiarante, and S. Greenberg, "Joint focal mechanism inversion using downhole and surface monitoring at the decatur, illinois, co2 injection site," *Bulletin of the Seismological Society of America*, vol. 110, 2020.

[34] E. Hicks, H. Bungum, and C. Lindholm, "Stress inversion of earthquake focal mechanism solutions from onshore and offshore norway," *Norsk Geologisk Tidsskrift*, vol. 80, pp. 235–250, 2000.

[35] R. J. Villegas A., J. Zahradník, S. Nacif, S. Spagnotto, D. Winocur, and M. F. Leiva, "Waveform inversion and focal mechanisms of two weak earthquakes in cordillera principal (argentina) between 35° and 35.5° s," *Journal of South American Earth Sciences*, vol. 71, pp. 359–369, 2016.

[36] E. N. Sokos and J. Zahradnik, "Isola a fortran code and a matlab gui to perform multiple-point source inversion of seismic data," *Computers & Geosciences*, vol. 34, no. 8, pp. 967–977, 2008.

[37] M. Sahimi, M. C. Robertson, and C. G. Sammis, "Fractal distribution of earthquake hypocenters and its relation to fault patterns and percolation," *Phys. Rev. Lett.*, vol. 70, pp. 2186–2189, Apr 1993.

[38] T. Candela, F. Renard, Y. Klinger, K. Mair, J. Schmittbuhl, and E. E. Brodsky, "Roughness of fault surfaces over nine decades of length scales," *Journal of Geophysical Research: Solid Earth*, vol. 117, no. B8, 2012.

[39] L. Bruhat, Y. Klinger, A. Vallage, and E. M. Dunham, "Influence of fault roughness on surface displacement: from numerical simulations to coseismic slip distributions," *Geophysical Journal International*, vol. 220, pp. 1857–1877, 12 2019.

[40] I. J. Hamling, S. Hreinsdóttir, K. Clark, J. Elliott, C. Liang, E. Fielding, N. Litchfield, P. Villamor, L. Wallace, T. J. Wright, E. D'Anastasio, S. Bannister, D. Burbidge, P. Denys, P. Gentle, J. Howarth, C. Mueller, N. Palmer, C. Pearson, W. Power, P. Barnes, D. J. A. Barrell, R. Van Dissen, R. Langridge, T. Little, A. Nicol, J. Pettinga, J. Rowland, and M. Stirling, "Complex multifault rupture during the 2016 mw 7.8 kaikoura earthquake, new zealand," *Science*, vol. 356, no. 6334, 2017.

[41] E. Hauksson, L. M. Jones, K. Hutton, and D. Eberhat-Phillips, "The 1992 landers earthquake sequence; seismological observations," *Journal of Geophysical Research B: Solid Earth*, vol. 98, no. B11, 1993.

[42] T. C. Hanks and H. Kanamori, "A moment magnitude scale," *Journal of Geophysical Research: Solid Earth*, vol. 84, no. B5, pp. 2348–2350, 1979.

[43] D. Dzurisin, *Volcano Deformation: New Geodetic Monitoring Techniques*. Heidelberg: Springer Berlin, 2007.

[44] M. Kumar, M. Husain, N. Upreti, and D. Gupta, "Genetic algorithm: Review and application," *J. of Inf. & Knowl. Management*, 2010.

[45] K. Deb and R. Agrawal, "Simulated binary crossover for continuous search space," *Complex Sys.*, vol. 9, no. 2, pp. 115–148, 1995.

[46] E. O. Lindsey, R. Natsuaki, X. Xu, M. Shimada, M. Hashimoto, D. Melgar, and D. T. Sandwell, "Line-of-sight displacement from alos-2 interferometry: m_w 7.8 gorkha earthquake and m_w 7.3 aftershock," *Geophys. Res. Lett.*, vol. 42, no. 16, pp. 6655–6661, 2015.

[47] United States Geological Survey, "M 7.8 - 26km E of Khudi, Nepal," 2015. `https://earthquake.usgs.gov/earthquakes/eventpage/us20002926/executive#general_summary` (accessed: 2020-06-10).

[48] T. Lay, L. Ye, K. Koper, and H. Kanamori, "Assessment of teleseismically-determined source parameters for the april 25, 2015 mw 7.9 gorkha, nepal earthquake and the may 12, 2015 mw 7.2 aftershock," *Tectonophysics*, vol. 714-715, 05 2016.

[49] K. Deb, K. Sindhya, and T. Okabe, "Self-adaptive simulated binary crossover for real-parameter optimization," in *Proc. of the 9th Ann. Conf. on Genetic and Evolutionary Computation*, p. 1187–1194, 2007.

[50] C. B. DuRoss, R. D. Gold, T. E. Dawson, K. M. Scharer, K. J. Kendrick, S. O. Akciz, S. J. Angster, J. Bachhuber, S. Bacon, S. E. K. Bennett, L. Blair, B. A. Brooks, T. Bullard, W. P. Burgess, C. Chupik, M. DeFrisco, J. Delano, J. F. Dolan, E. Frost, N. Graehl, E. K. Haddon, A. E. Hatem, J. L. Hernandez, C. Hitchcock, K. Hudnut, J. Thompson Jobe, R. Koehler, O. Kozaci, T. Ladinsky, C. Madugo, D. S. McPhillips, C. Milliner, A. Morelan, B. Olson, J. Patton, B. Philibosian, A. J. Pickering, I. Pierce, D. J. Ponti, G. Seitz, E. Spangler, B. Swanson, K. Thomas, J. Treiman, F. Valencia, A. Williams, and R. Zinke, "Surface Displacement Distributions for the July 2019 Ridgecrest, California, Earthquake Ruptures," *Bulletin of the Seismological Society of America*, vol. 110, no. 4, pp. 1400–1418, 2020.

[51] K. Wang, D. S. Dreger, E. Tinti, R. Bürgmann, and T. Taira, "Rupture Process of the 2019 Ridgecrest, California Mw 6.4 Foreshock and Mw 7.1 Earthquake Constrained by Seismic and Geodetic Data," *Bulletin of the Seismological Society of America*, vol. 110, pp. 1603–1626, 07 2020.

[52] W. D. Barnhart, R. D. Gold, and J. Hollingsworth, "Localized fault-zone dilatancy and surface inelasticity of the 2019 Ridgecrest earthquakes," *Nature Geoscience*, vol. 13, pp. 699–704, 2020.

[53] B. Mandelbrot, "How Long Is the Coast of Britain? Statistical Self-Similarity and Fractional Dimension," *Science*, vol. 156, pp. 636–638, 1967.

[54] D. G. Tarboton, R. L. Bras, and I. Rodriguez-Iturbe, "The fractal nature of river networks," *Water Resources Research*, vol. 24, no. 8, pp. 1317–1322, 1988.

[55] J. B. Bassingthwaighte, L. S. Liebovitch, and B. J. West, *Fractal Physiology*. New York: Springer New York, 1994.

[56] R. P. Taylor, A. P. Micolich, and D. Jonas, "Fractal analysis of Pollock's drip paintings," *Nature*, vol. 399, 1999.

[57] Z. Q. Mu and C. W. Lung, "Studies on the fractal dimension and fracture toughness of steel," *Journal of Physics D: Applied Physics*, vol. 21, no. 5, pp. 848–850, 1988.

[58] M. A. Issa, M. A. Issa, M. Islam, and A. Chudnovsky, "Fractal dimension—a measure of fracture roughness and toughness of concrete," *Engineering Fracture Mechanics*, vol. 70, no. 1, pp. 125–137, 2003.

[59] I. Pavičić, I. Dragičević, T. Vlahović, and T. Grgasović, "Fractal analysis of fracture systems in upper triassic dolomites in Žumberak mountain, croatia," *Rudarsko-geološko-naftni zbornik*, vol. 32, pp. 1–13, 07 2017.

[60] Y. Y. Kagan and L. Knopoff, "Spatial distribution of earthquakes: the two-point correlation function," *Geophysical Journal of the Royal Astronomical Society*, vol. 62, no. 2, pp. 303–320, 1980.

[61] A. Kumar, S. S. Rai, A. Joshi, H. Mittal, R. Sachdeva, R. Kumar, and V. Ghangas, "The b-value and fractal dimension of local seismicity around koyna dam (india)," *Earthquake Science*, vol. 26, pp. 99–105, 2013.

[62] Y. Y. Kagan, "Fractal dimension of brittle fracture," *Journal of Nonlinear Science*, vol. 1, pp. 1–16, 1991.

[63] X. Lei and K. Kusunose, "Fractal structure and characteristic scale in the distributions of earthquake epicentres, active faults and rivers in Japan," *Geophysical Journal International*, vol. 139, pp. 754–762, 12 1999.